Feasibility Analysis and Experimental Demonstration of Multisource Thermophotovoltaic Systems

Shahriar Homaei

A THESIS SUBMITTED TO THE FACULTY OF GRADUATE STUDIES IN PARTIAL FULFILLMENT OF THE REQUIREMENTS FOR THE DEGREE OF MASTER OF APPLIED SCIENCES

GRADUATE PROGRAM IN MECHANICAL ENGINEERING

YORK UNIVERSITY

TORONTO, ONTARIO

September 2025

© Shahriar Homaei, 2025

Abstract

With the growing need for efficient conversion of heat to electricity, thermophotovoltaic (TPV) systems offer a promising solution and gaining attention. Most TPV systems, however, are designed around a single heat source. In practice, situations like fluctuating solar irradiance or limited heat availability in space suggest that combining multiple heat sources could make these systems more effective. Yet, both the numerical and experimental impacts of adding auxiliary sources to TPV setups remain underexplored.

In this thesis, I take on the idea of a multi-source TPV system, combining both analytical modeling and experimental work. Using established physical equations and MATLAB simulations, I compared the electrical output and in-band emissive power of TPV cells powered by single versus dual heat sources across different input levels. On the experimental side, I built a custom absorber–emitter, using a tungsten coating on an aluminum nitride substrate reaching to 1060 K, and tested it inside a vacuum-based setup. This allowed me to study the system under controlled conditions using both Joule heating and radiative heat sources at the same time.

The results show that powering the emitter with more than one source significantly boosts electrical output from 1.08 to 1.72 mW/cm². Moreover, the combined effect is most pronounced at lower input power levels. Just as importantly, the experimental data matched closely with the theoretical predictions 1.44 and 2.05 mW/cm², supporting the validity of the multi-source approach. Together, these findings highlight how multi-source TPV systems can improve both reliability and efficiency under changing conditions. They also point toward future opportunities, from refining emitter designs and exploring additional heat sources to developing portable TPV devices that could make sustainable energy more practical and accessible.

Acknowledgment

I would like to sincerely thank all those who have supported me throughout this journey and accomplishing my research.

I would like to express my deepest gratitude to my supervisor, **Dr. Paul O'Brien**, whose invaluable guidance, continuous support, and encouragement have been a constant source of motivation throughout my research journey.

Special thanks to my lab mates, **Dr. Nima Talebzadeh** and **Keshav Ramparsad**, for their collaboration and insightful discussions that greatly enriched this work and made the lab environment a welcoming place.

I am grateful to **Columbiad Launch Services** for their essential support, which played a significant role in advancing this project.

To **Paria**, thank you for your unwavering support and encouragement every step of the way; your presence has meant more than words can express.

I also extend my heartfelt thanks to **my friends**, who kept me motivated and cheerful during the challenging moments over these past two years.

Most importantly, I am profoundly thankful to **my family**, who supported me from far across the seas, their spiritual support, prayers, and the sacrifices they made in my absence have been the bedrock of my perseverance and achievement.

Thank you all.

Table of Contents

Abstract II
Acknowledgment III
List of Figures VI
List of Tables IX
List of Symbols X
List of Abbreviations XII
1 Chapter 1: Introduction 1
1.1 Background and TPV Technology 1
1.2 Research Gap 4
1.3 Research Objectives 5
1.4 Thesis Outline 6
2 Chapter 2: Background and Literature Review 8
2.1 Heat Sources 9
2.2 Emitter 9
2.2.1 Selective Emitters 9
2.2.2 Tungsten-Based Emitters 14
2.2.3 Micro Heaters and Tungsten Integration 18
2.2.4 Deposition Processes 20
2.3 TPV Cell Overview 26
2.3.1 Historical Overview 26
2.3.2 Fundamentals of TPV Energy Conversion 27
2.4 Background Studies on TPV Systems 31
2.5 Multisource Systems 46
2.5.1 Hybrid TPV System Background 46
2.5.2 Fundamental Operating Principles of Multisource TPV Systems 49
3 Chapter 3: Methods 52
3.1 Analytical 52
3.1.1 Simulated Thermal Performance of the Absorber–Emitter 52
3.1.2 Numerical Analysis of the Thermophotovoltaic System 58
3.2 Experimental 63
3.2.1 External Instrumentation and Support Systems 63
3.2.2 Internal Chamber Assembly and Experimental Setup 66
3.2.3 Experimental Preparation and Data Acquisition 79
4 Chapter 4: Results & Discussion 84
4.1 Analytical 84

4.1.1 COMSOL Simulation Results for the Emitter 84
4.1.2 Analytical Performance Results of the Thermophotovoltaic Systems 87
4.2 Experimental 92
4.2.1 Absorber–Emitter Performance 92
4.2.2 TPV Cell Performance Results 95
4.3 Analytical–Experimental Correlation of Emitter and TPV System Performance 100
4.3.1 Absorber-Emitter Performance Comparison 100
4.3.2 TPV System Performance Comparison 104
5 Chapter 5: Conclusion & Future Work 106
5.1 Conclusion 106
5.2 Future Work 108
6 References 111

List of Figures

Figure 1-1 Key elements of a typical TPV system..... 1

Figure 1-2 (a) State of the art TPV efficiency, (b) TPV cell electrical output density [9], (c) Evolution of efficiency in thermal-to-electric energy conversion technologies [8]..... 2

Figure 1-3 (a) Main component and (b) an example of a multi-source TPV system..... 4

Figure 2-1 Comparison of broadband and narrow-band emitters: Broadband emitters provide higher total radiated power, while narrow-band emitters can enhance photovoltaic conversion efficiency. Emittance and radiated power are shown relative to a 1000 °C blackbody.[25]..... 10

Figure 2-2 (a,b) Si/SiO_2 1D PhC [35] [36] and (c) HfO2/W multilayer..... 12

Figure 2-3 2D PhC (a,b) tungsten-based [38], and (c) tantalum-based [40] emitters..... 13

Figure 2-4 3D PhC (a) HfO_2-coated tungsten [41], and (b) consisting of Si/SiO_2/Pt [42]..... 13

Figure 2-5 Diagram of a) a flat STPV system and b) a cylindrical STPV system, both with solar absorber and thermal emitter [49]..... 17

Figure 2-6 Bilayer emitter consisting of bulk substrate and a coating layer [50] 17

Figure 2-7 A general classification of surface engineering techniques [58]. 20

Figure 2-8 Illustration of two common PVD techniques: (a) sputtering and (b) evaporation using ionized argon (Ar^+) gas [64] 22

Figure 2-9 Diagram of a DC unbalanced magnetron sputtering setup [68]..... 24

Figure 2-10 The processing flow for a classic PVD sputtering process [64]..... 25

Figure 2-11 Absorber-emitter schematic..... 26

Figure 2-12 The periodic table showing the semiconductor groups [83] 28

Figure 2-13 Schematic of a solar cell showing the n-type and p-type semiconductor layers, the PN junction, and the flow of electrons generated by light energy that produces electric current [85] 29

Figure 2-14 IV characteristic [86]..... 30

Figure 2-15 (a) CAD model with labels of the experimental micro-TPV system, (b) the micro-TPV system during operation [35] 32

Figure 2-16 (a) Demonstration of prototype components, and (b) assembled prototype [88]..... 33

Figure 2-17 (a) TPV system sketch, (b,c) GaSb and InGaAs cell with water cooling on the back surface, (d) heating elements, and (e) tungsten emitter within a quartz crucible [89] 34

Figure 2-18 Overall demonstration of components of TPV system [87]..... 35

Figure 2-19 Experimental configuration for studying photon recycling effects on emitter temperature and output power [90]..... 37

Figure 2-20 (a) Sketch of major components of the TPV system, and (b) top view of the setup including refrigration system [22]..... 38

Figure 2-21 (a) Cross section of schematic, and (b) top view diagram of system setup [49]..... 39

Figure 2-22 (a) Sketch of the TPV system, and (b) realistic vacuumed setup [21] 40

Figure 2-23Exploded view of the components making up the STPV system prototype [91]..... 42

Figure 2-24 (a) Schematic, and (b) image of the concentrator setup [73] 43
Figure 2-25 (a) sunlight simulator sketch, (b) STPV-TE 3D structure, and (c) diagram of STPV-TE system [92] 45
Figure 2-26 Schematic of a hypothetical multi-source TPV system 49
Figure 2-27 Radiative heat exchange between two surfaces A and B 50
Figure 3-1 Tungsten electrical resistivity and conductivity based on temperature 55
Figure 3-2 Total emissivity of tungsten based on temperature 56
Figure 3-3 Specific heat capacity and thermal conductivity of AlN 56
Figure 3-4 Total hemispherical emissivity of AlN relative to temperature 57
Figure 3-5 (a) Meshed geometry of the absorber–emitter (b) maximum temperature variation with mesh elements 57
Figure 3-6 Numerical evaluation of VF using COMSOL simulation 62
Figure 3-7 External instrumentation comprises (a) chiller, (b) vacuum pump, (c) LabJack T7 data acquisition system, (d) vacuum chamber, (e) benchtop gauge controller and (f) power supply 63
Figure 3-8 Internal chamber assembly comprising (a) light source, (b) emitter segment, (c) TPV circuit assembly, and (d) cooling system 66
Figure 3-9 Tungsten sputtering target [112] 68
Figure 3-10 AMOD PVD platform 69
Figure 3-11 AlN substrates (a) before and (b) after depositing tungsten onto their surface 70
Figure 3-12 Tungsten target during sputtering 71
Figure 3-13 Spectral hemispherical emittance of the absorber-emitter 72
Figure 3-14 Expanded view of the assembled emitter segment, showing (a) the 304-grade stainless steel base, (b) Al_2O_3 insulation layer, (c) tungsten-coated emitter, (d) tungsten contact strips, (e) AlN ceramic blocks, and (f) Al_2O_3 ceramic blocks with pre-formed screw holes. 73
Figure 3-15 (a) GaSb TPV cell and its (b) external quantum efficiency 74
Figure 3-16 TPV cell (a-d) connectors and (e) assembled circuit 75
Figure 3-17 1600nm Spectral filter coating performance [116] 76
Figure 3-18 Tubed cold plate 77
Figure 3-19 Liquid feedthrough 78
Figure 3-20 (a) Reducer tube adaptor, (b) bulkhead reducing union 78
Figure 3-21 TPV system components on top of the cooling plate including (a) the black baffle with a rectangular opening, (b) metal zip ties, (c) thermocouple, and (d) the spectral filter 79
Figure 3-22 Emitter holder system viewed from (a) the top and (b) the bottom 80
Figure 3-23 Completed experimental assembly 81
Figure 3-24 IV Curve circuit measurement 83
Figure 4-1 Simulation temperature result from the sputtered substrate with 1 μm tungsten layer and an input voltage of 10 V 84

Figure 4-2 Emitter temperature relative to joule heating power for various sputtered tungsten thicknesses. 85

Figure 4-3 In-band emissive power of Si, GaSb, and InGaAs cells under single, separate, and simultaneous 5 W/cm² heat sources, showing enhanced output in multisource mode..... 88

Figure 4-4 (a) the sum of the output power from a TPV system when it is powered by two sources individually (case 2) (b) the output power from a TPV system when it is simultaneously powered by two sources (case 3)). (c) the power enhancement (case 3/case 2) is achieved by powering the TPV system with two power sources simultaneously as compared to the power generated when the power sources are used individually. 90

Figure 4-5 Absorber–emitter assembly during experimental testing 92

Figure 4-6 Absorber-emitter temperature relative to electrical input power..... 93

Figure 4-7 Emitter temperature relative to input power considering losses 94

Figure 4-8 Measured IV curves of the TPV cell at various emitter temperatures..... 95

Figure 4-9 Experimental FF..... 96

Figure 4-10 Measured TPV output power across different emitter temperatures 97

Figure 4-11 Comparison and demonstration of TPV system output power in multisource and separate modes across variations in emitter power density, with color pillars representing multisource operation and cross-line bars indicating separate source measurements..... 98

Figure 4-12 (a) the sum of the experimental output power from the TPV system when it is powered by halogen lamp and joule heater individually (case 2) (b) the output power from the TPV system when it is simultaneously powered by two heat sources (case 3). (c) the power enhancement (case 3/case 2) is achieved by powering the TPV system with two power sources simultaneously as compared to the power generated when the power sources are used individually. 99

Figure 4-13 (a) cross sectional, and (b) top view SEM images of tungsten deposited onto a AlN substrate 100

Figure 4-14 Comparison of experimental and simulated emitter temperatures with a 260 nm tungsten coating: (a) using supplied electrical power and (b) using radiative input power corrected..... 102

Figure 4-15 The output result from analytical modelling by utilizing experimental inputs 104

List of Tables

Table 2-1 Sputtering versus Evaporation parameters comparison [64] 23

Table 2 Thermal performance of tubed cold plate [118] 77

List of Symbols

Symbol	***Full Expression***	***Units***
A_{AlN}	Aluminum Nitride surface area	m^2
A_W	Tungsten surface area	m^2
c	Speed of light	m/s
C_p	Specific heat capacity	J/kg·K
E_b	Plank's law of blackbody radiation	$W/m^2 \cdot m$
E_g	Bandgap energy	eV
I_{mp}	Current at maximum power	A
I_{SC}	Short-circuit current	A
J	Current density	W/m^2
J_0	Recombination losses	A/m^2
J_{mp}	Current density at maximum power	A/m^2
J_{sc}	Short-circuit current density	A/m^2
k	Thermal conductivity	W/m.k
k_B	Boltzmann constant	J/K
P_{actual}	Actual power	W
P_{in}	Input power	W
P_{mp}	Maximum power point	W/m^2
P_{out}	Output power	W
q	Electron quantity of electron	C
Q_e	Volumetric rate of heat generation	W/m^3
q_i	Net spectral radiant heat flux	$W/m^2 \cdot m$
S	Siemens	1/ Ω
t	Thickness	mm
T	Temperature	K
$T_{ambient}$	Ambient temperature	K
T_{cell}	TPV cell temperature	K
T_{em}	Emitter temperature	K

Symbol	***Full Expression***	***Units***
V_{mp}	Voltage at maximum power	V
V_{OC}	Open-circuit voltage	V
w	Substrate edge width	mm
ε	Emissivity	-
ε_{AlN}	Aluminum Nitride emissivity	-
ε_{W}	Tungsten emissivity	-
λ	Wavelength	µm
λ_{bg}	Bandgap wavelength	µm
ρ	Resistivity	Ω·m
ρ_m	Density	kg/m³
σ	Electrical conductivity	S/m
σ_{SB}	Stefan–Boltzmann constant	$W/m^2 \cdot K^4$

List of Abbreviations

Abbreviation	*Full Expression*
AlGaInAs	Aluminum Gallium Indium Arsenide
AlN	Aluminum Nitride
ARC	Anti-Reflection Coating
Bi_2Te_3	Bismuth Telluride
CSP	Concentrated Solar Power
CVD	Chemical Vapor Deposition
DC	Direct Current
DNI	Direct Normal Irradiance
EQE	External Quantum Efficiency
Er	Erbium
FF	Fill Factor
FTIR	Fourier Transform Infrared Spectroscopy
GaInAsSb	Gallium Indium Arsenide Antimonide
GaSb	Gallium Antimonide
HfO_2	Hafnium Dioxide
Ho	Holmium
InGaAS	Indium Gallium Arsenide
IR	Infrared
LCOE	Levelized Cost of Electricity
MgO	magnesium Oxide
MWNT	Multiwalled Carbon Nanotube
NF-TPV	Near-field Thermophotovoltaic
PCB	Printed Circuit Board
PhC	Photonic Crystal
Pt	Platinum
PV	Photovoltaic
PVD	Physical Vapor Deposition
RF	Radiofrequency

Abbreviation	*Full Expression*
SCCM	Standard Cubic Centimeters per minute
SEM	Scanning Electron Microscope
SF_6	Sulfur Hexafluoride
Si	Silicon
Si_3N_4	Silicon Nitride
SiC	Silicon Carbide
SiO_2	Silicon Dioxide
SOFC	Solid Oxide Fuel Cells
STPV	Solar Thermophotovoltaic
Ta	Tantalum
TE	Thermoelectric
TEGS	Thermal Energy Grid Storage
TPV	Thermophotovoltaic
UV-Vis	Ultraviolet-visible
VF	View Factor
W	Tungsten
YAG	Yttrium Aluminum Aarnet
Yb	Ytterbium
YSZ	Yttria-Stabilized Zirconia
BN	Boron Nitride

1 Chapter 1: Introduction

1.1 Background and TPV Technology

The efficient conversion of thermal energy into electricity is increasingly important, driven by industrial waste heat and the growing use of thermal storage systems such as thermal batteries. One of the best solutions for this is using TPV systems [1].

TPV systems are similar to regular photovoltaic (PV) panels, but instead of using sunlight, they convert infrared thermal radiation into electricity [2]. They convert heat, which can come from a variety of sources, into usable electrical energy using PV cells. TPV devices have been studied since the 1960s and were first introduced as an alternative to thermoelectric and thermionic devices for direct energy conversion [3].

A typical TPV system, shown in Figure 1-1, includes three main components: a heat source such as solar energy, heat from combustion, waste heat, or nuclear heat to raise the temperature of the emitter; the emitter, normally combined with filters or reflectors to control the spectrum of the emitted radiation; and a PV cell that receives the radiated heat and converts it into electricity [4].

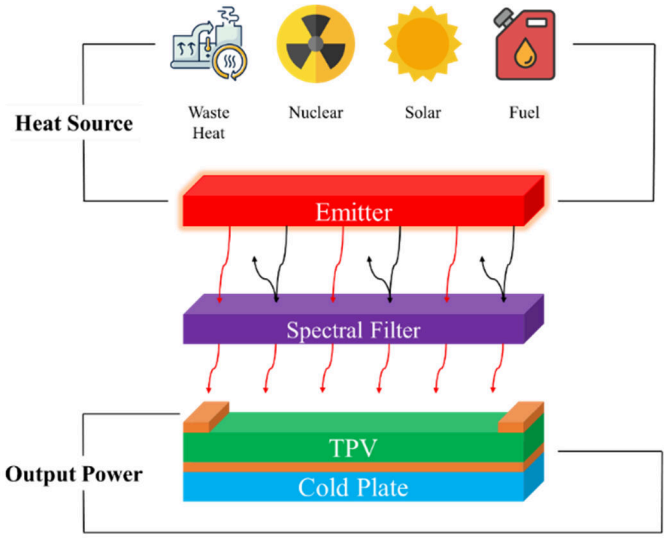


Figure 1-1 Key elements of a typical TPV system

The main role of the heat source is to raise the emitter temperature from about 1000 to 2000 K [5], enabling it to emit sufficient infrared radiation. Unlike conventional PV cells that respond primarily to ultraviolet and visible light, TPV cells are made from narrow bandgap semiconductor materials such as GaSb [6] and InGaAs [7], with bandgaps of approximately 0.72 eV and 0.59 eV, respectively. These materials are specifically designed to absorb in-band infrared photons, those with energies greater than the bandgap of the PV cell. In other words, these photons have enough energy to excite electrons across the bandgap, generating electron-hole pairs and thus producing electricity.

In recent years, TPV technology has made notable progress (Figure 1-2a), reaching efficiencies between 30–44% at emitter temperatures ranging from about 1000 °C to 2400 °C [8], [9]. TPV systems not only operate silently due to the absence of moving parts but with the rising efficiencies shown in Figure 1-2c, are now comparable to conventional turbogenerators [10].

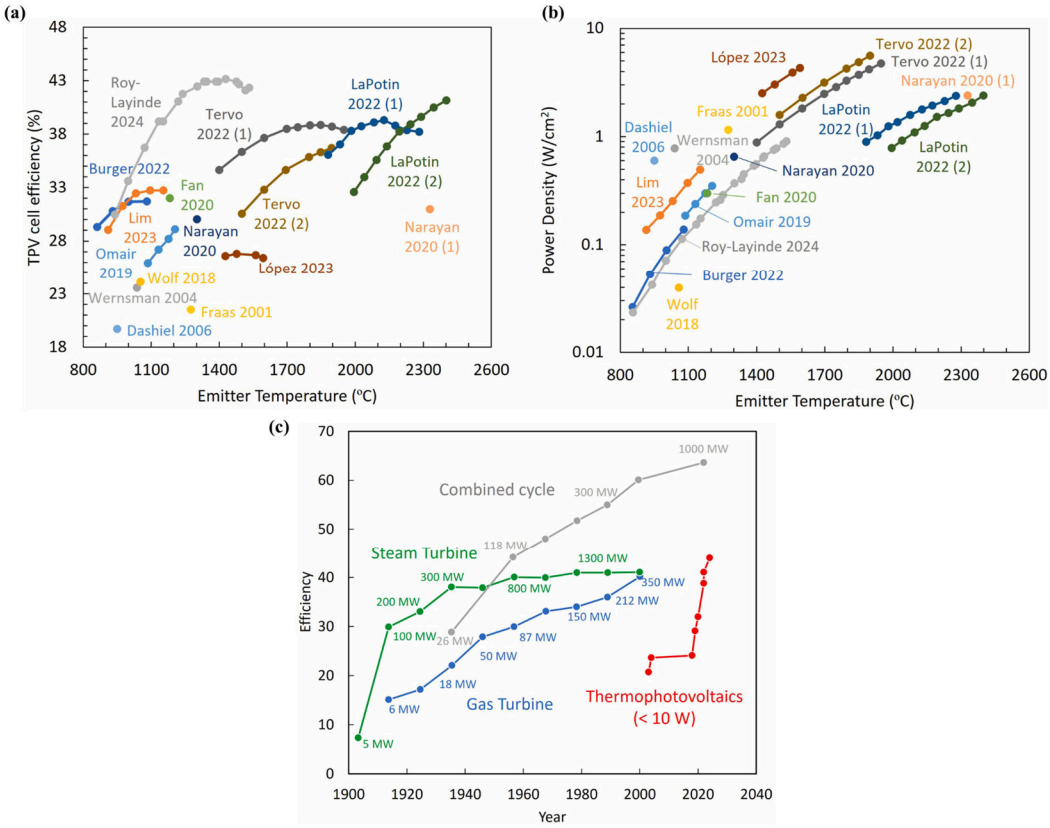


Figure 1-2 (a) State of the art TPV efficiency, (b) TPV cell electrical output density [9], (c) Evolution of efficiency in thermal-to-electric energy conversion technologies [8]

Their compact and lightweight design further enhances portability, positioning TPVs as a promising solution for space applications where high specific power and remote power generation are essential [11]. In addition, TPV technology is emerging as a strong candidate for high-temperature thermal battery systems, offering greater energy density and cost-effectiveness for grid-scale energy storage compared to traditional electrochemical batteries [12].

TPV generators operate efficiently at various scales and support decentralized electricity production from multiple thermal sources, this means that TPV systems are versatile in harnessing different heat sources, including solar radiation [13], nuclear energy, chemical fuel combustion [14], and waste heat recovery [15]. This adaptability significantly expands their potential for sustainable and off-grid energy solutions.

As shown in Figure 1-2a-b, increasing the emitter temperature and input power shifts the radiation spectrum toward shorter wavelengths and a greater fraction of in-band photons are emitted. This causes an increase in the PV system's efficiency and electrical output density. Furthermore, to enhance their utility and reliability, TPV systems can be powered using multiple heat sources. In multi-source TPV systems, unlike traditional TPV systems, multiple sources provide heat to the emitter simultaneously (Figure 1-3a). Subsequently, the emitter, with its elevated temperature, leads to an overall improvement in system efficiency. For instance, solar-powered TPV systems are a promising solution for remote or transportable power in sunny regions. However, solar irradiance is variable and intermittent. By incorporating a secondary heat source, such as fuel or waste heat, solar-powered TPV systems can operate without interruption and more efficiently (Figure 1-3b). In space applications, a secondary source is also vital to improve output power efficiency, especially considering weight limitations.

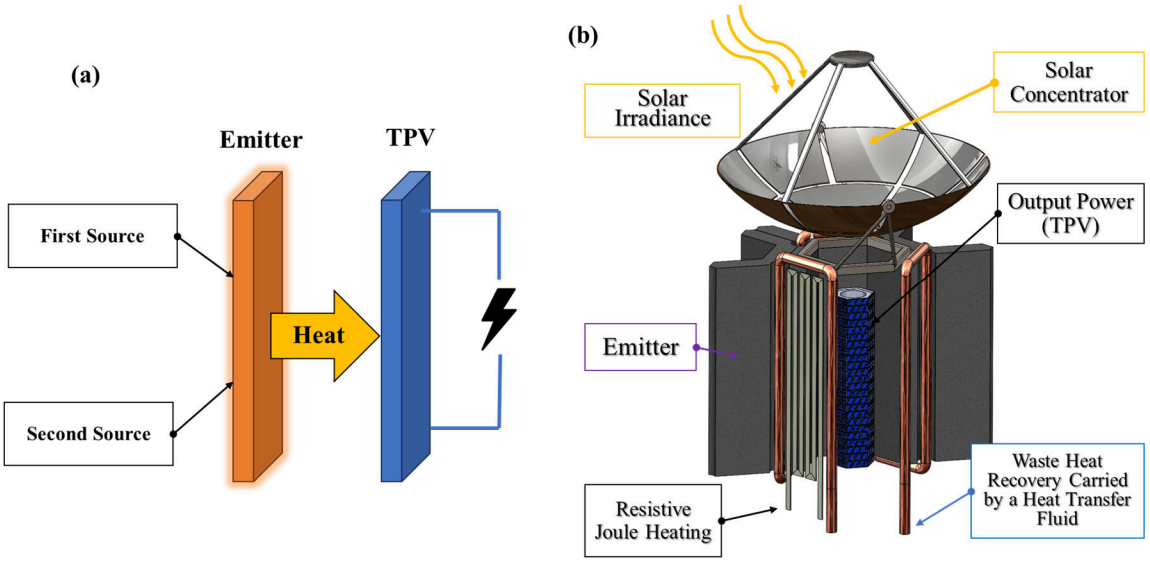


Figure 1-3 (a) Main component and (b) an example of a multi-source TPV system

The first advantage of a multi-source system is its increased versatility, offering the opportunity to integrate different sources within a single setup. Additionally, higher electrical output can be expected when operating in dual-source mode compared to single-source mode. This approach also allows low-grade heat sources to contribute more significantly to the overall power output.

1.2 Research Gap

The existing literature pertaining to multi-source powering of TPV systems only investigates the implementation of a secondary source in a general way. When evaluating new technologies, it's important to assess their performance, including what these technologies can provide under ideal conditions and their likely performance under practical limitations. However, a rigorous assessment of multi-source TPV systems has yet to be reported. That is, to date, research on multisource TPV systems has focused on introducing the concept, cost analysis, and construction of multisource TPV systems, and the presentation of rigorous numerical analysis and experimental results has been limited. This thesis focuses on the theoretical and numerical advantages of TPV systems powered by multiple sources, and ultimately on building a prototype and conducting experiments to measure the benefits of using two heat sources simultaneously to power a TPV system, with the results validated against theoretical predictions.

1.3 Research Objectives

Considering the limited numerical and experimental investigations conducted on multi-source TPV systems, this thesis aims to demonstrate the feasibility and potential of such systems through the following objectives:

- Objective 1: Prove the concept of a multi-source TPV system analytically by applying established performance equations, including formulas for spectral in-band emissive power and electrical power output.

The core approach involves using MATLAB to numerically model the system and compare the electrical output from TPV systems when heated using a single source or dual sources. A parametric analysis will be carried out by varying the input power levels to theoretically validate the multi-source configuration and assess its performance benefits.

- Objective 2: Fabricate an absorber-emitter capable of reaching high temperatures under vacuum conditions.

This component must serve two functions: first, to act as an absorber that collects energy from a remote radiative heat source; and second, to operate as a thermal emitter that, when sufficiently heated, radiates photons with energies above the bandgap of the TPV cell, thereby driving electricity generation. The design must ensure ease of fabrication and exhibit high thermal and structural stability during simultaneous absorption and emission.

- Objective 3: Utilize the absorber-emitter developed in Objective 2 to construct a vacuum-based multi-source TPV system and experimentally validate the theoretical findings.

The complete multi-source TPV system, including the custom emitter and a specially designed TPV circuit, will be assembled, and operated inside a vacuum chamber. A water-based cooling system will be integrated to reduce the operating temperature of the PV cell thereby improving heat-to-electric power conversion efficiency.

1.4 Thesis Outline

This thesis begins with a literature review, which provides background information useful for understanding the methodology and results obtained. The thesis outline is structured as follows:

- Chapter 2: Background and Literature Review:

A comprehensive review of previous experiments will be carried out focusing on the three main elements of a TPV system. First, different types of heat sources will be examined. Following this, thermal emitters will be reviewed in terms of their materials and properties, which also connects to Objective 2 which is fabricating an absorber–emitter. Next, a historical overview of TPV cells and the fundamentals of their operation will be presented. In addition, various experimental TPV systems and their characteristics will be analyzed, paying particular attention to how the main components have been implemented. This review will serve as a basis for designing a setup and selecting the most suitable option for the second heat source. Finally, background studies on existing hybrid TPV systems will be included, highlighting the current research gaps and identifying opportunities for improvement.

- Chapter 3: Methods:

In the first stage, the thermal profile of the absorber–emitter will be numerically analyzed using COMSOL Multiphysics, with details provided on the governing physics, material properties, and applied boundary conditions. Following this, and in line with Objective 1, a comparison between single-source and multi-source TPV systems will be conducted, evaluating both the in-band emissive power and the actual TPV output. The experimental stage, corresponding to Objective 3, will then focus on assembling the different components of the multi-source TPV setup. Each section of the system will be described in terms of its fabrication and integration process, leading to the complete preparation of the setup. Finally, the methods used for data acquisition and subsequent analysis will be outlined.

- Chapter 4: Results & Discussion:

In this chapter, the results obtained from the procedures described in Chapter 3 will be presented. These include the analytical section, which covers the simulated performance of the absorber–emitter and the numerical investigation of the TPV system, as well as the experimental section, which demonstrates the final TPV output under both single-source and multi-source conditions. A comparison between these two approaches will then be carried out to highlight their consistencies and differences. Finally, a discussion will be provided to interpret the findings and place them in context, offering deeper insight into the overall performance of the system.

- Chapter 5: Conclusion & Future Work:

The overall conclusions of this work will be provided in the last chapter and will bring together the key results from both the analytical and experimental parts. It will show how the objectives were addressed and what insights have been gained from the comparison between single-source and multi-source TPV systems. Chapter 5 will also suggest directions for future work, including improvements in emitter design, system assembly, and further testing under different conditions to strengthen the performance of multi-source TPV systems.

2 Chapter 2: Background and Literature Review

A TPV system consists of three primary components: a heat source that provides thermal energy, an emitter that transforms this heat into a tailored emission spectrum, and a photovoltaic (PV) cell that absorbs the emitted radiation and converts it into electrical power.

TPV systems have gained significant attention due to their high efficiency and versatility in renewable energy applications. These systems have demonstrated efficiencies ranging from 30% to 44% at emitter temperatures between 1000 and 2400 °C, making them comparable to conventional turbogenerators. Additionally, their compact and lightweight design enhances portability, making them particularly suitable for space applications. TPV generators operate silently and without moving parts, enabling decentralized electricity production from various heat sources while maintaining high conversion efficiency regardless of scale [16]. Moreover, TPV technology shows promise for high-temperature thermal battery systems, offering superior energy density and cost efficiency for grid-scale energy storage compared to electrochemical batteries [17].

Another key advantage of TPV systems is their ability to utilize diverse heat sources, including solar radiation, radioactive isotopes, chemical fuel combustion, and waste heat recovery, further broadening their potential for sustainable energy solutions [18].

Since TPV systems can generate electricity from different heat sources, it is of interest to investigate the benefits of using multiple heat sources simultaneously to power TPV systems. This concept is particularly useful for space applications, where reducing weight is crucial. Combining multiple heat sources, such as concentrated sunlight or laser power beaming, alongside fuel, could provide important advantages.

In this section, after discussing the three key components of a TPV system and examining various TPV system setups, the focus shifts to hybrid TPV systems by reviewing relevant studies and previous research in the field.

2.1 Heat Sources

Thermophotovoltaic systems can operate with a variety of heat sources, each suited to specific applications and operating environments. One common approach is fuel combustion, which has been extensively studied for use in portable power systems [19]. Industrial waste heat is another promising option to utilize inside TPV systems [20]. Solar energy has also been adapted, where concentrated sunlight is used to provide a heat source for TPV applications [21]. Moreover, in other literature, laser power beaming was utilized as a wireless high-power heat source that would be beneficial for providing power from a distance [22].

2.2 Emitter

The emitter is heated to a high temperature such that it radiates thermal energy toward a TPV cell. The efficiency of this process depends on how much of the emitted radiation has energy greater than the bandgap of the PV cell (referred to as in-band photons), as only these in-band photons can be converted into electricity. To maximize this usable portion of the spectrum, the concept of a selective emitter was introduced, which is designed to enhance in-band emission while suppressing out-of-band losses.

2.2.1 Selective Emitters

An ideal selective emitter has a unity in-band emittance for a TPV cell and zero emittance at other wavelengths. Emitted photons with less energy than that of the TPV cell bandgap are referred to as out-of-band photons. Out-of-band photons cannot generate electricity, and the heat caused by these unabsorbed photons can raise the temperature of the TPV cell, which decreases its efficiency and lifespan [23]. A selective emitter is made to emit a greater portion of in-band photons while emitting less out-of-band photons. As shown in Figure 2-1, these emitters can be tuned to work in either broadband or narrow-band modes [24].

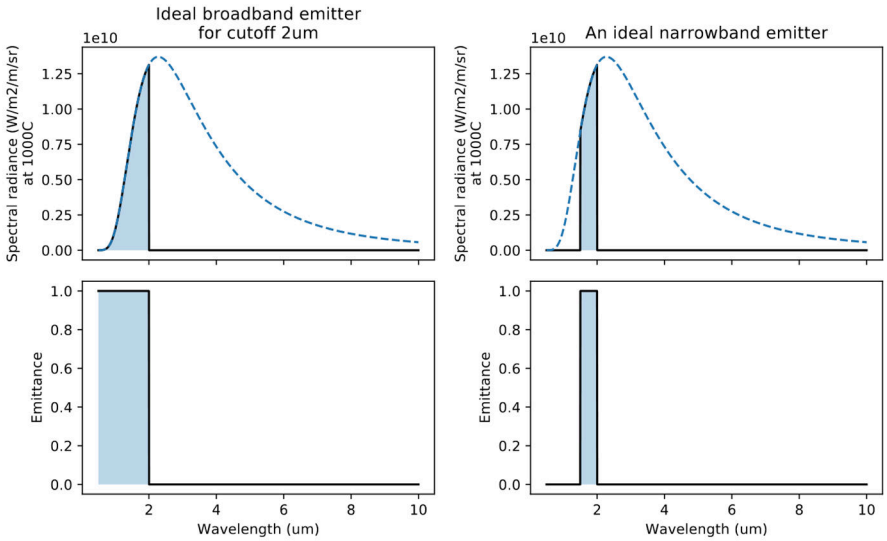


Figure 2-1 Comparison of broadband and narrow-band emitters: Broadband emitters provide higher total radiated power, while narrow-band emitters can enhance photovoltaic conversion efficiency. Emittance and radiated power are shown relative to a 1000 °C blackbody.[25].

To design a selective emitter, two approaches can be implemented. The first is to rely on the inherent optical properties of a material and search for a suitable one with an emissivity spectrum that best matches the bandgap of the TPV cell. The other method is to take a broadband material and manipulate its surface emittance by altering its texture. These two methods can also be combined. There are three different categories into which emitters can be classified: (1) bulk emitters, (2) rare-earth composite or doped emitters, and (3) photonic crystal (PhC) emitters. In this work, the focus was on the emitters that have been used in experimental and prototype systems [23].

2.2.1.1 Bulk Emitters

These materials have broadband emittance and are available as refractory materials. Materials such as Tungsten (W) [26], Silicon (Si) [26], Silicon Carbide (SiC) [27], Tantalum (Ta), and Platinum (Pt) [28] have commonly been used in experiments. These materials by themselves do not have high emissivity. Utilizing an anti-reflection coating (ARC) contributes to enhancing in-band thermal radiation. For example, Shimizu et al. [29] made an absorber–emitter based on a tungsten emitter coated on both sides with yttria-stabilized zirconia (YSZ) as an ARC, enhancing the top for absorbing solar irradiance and the bottom for

matching the GaSb bandgap. Fraas et al. [30] also used a SiC substrate coated with tungsten and added ARC to the tungsten to reach 75% spectral efficiency for generating electricity using a GaSb cell.

2.2.1.2 Rare Earth Composite

Rare earth materials, unlike bulk emitters, are inherently selective and possess high emissions in narrow IR regions. Also, rare earth materials can be easily fabricated by doping them into ceramic hosts. Since they are monolithic ceramics, they are often thermally stable at high temperatures. Moreover, if they are embedded in oxide-based hosts (e.g., yttrium aluminum garnet (YAG)[31]), they become suitable candidates for use in oxidizing environments like air. This offers an advantage over bare metals such as tungsten, which degrades in the presence of oxygen. Among the well-known rare earth emitters, Erbium (Er) stands out due to its high emittance at wavelengths around 1.5 μm, making it suitable for GaSb cells which are commonly used in TPV systems [32]. Ytterbium (Yb) [33] and Holmium (Ho) [34] have also been highly studied in this context.

2.2.1.3 Photonic Crystals

One of the most promising methods for reaching high spectral control in TPV systems is Photonic Crystal (PhC) emitters. In scales of micro or nano, periodic geometries are utilized to manipulate electromagnetic waves and make their emittance spectrum suitable for the TPV cells' bandgap. PhC emitters can be categorized into three major categories based on their structure: one-dimensional (1D), two-dimensional (2D), and three-dimensional (3D). Another kind of similar type is multilayer emitters, which are practically like 1D PhCs. Although 1D and 2D PhC emitters are mostly exploited in literature, 3D PhCs are scarce due to their fabrication complexity and limited performance improvement.

1D PhCs are made of alternating planer layers with contrasting indices of refraction. These emitters are generally easier to fabricate by deposition techniques. Chan et al. [35] built a Si/SiO_2 1D PhC combined

with a micro-combustor reactor for a TPV system comprising a InGaAsSb cell. The operating temperature reached 1073 K with a maximum system efficiency of 2.5%. Using the same Si/Si/SiO_2 1D PhC emitter, Lenert et al. [36] reached a system efficiency of 3.2% at an operating temperature of 1285 K. Multilayer stacks are similar to 1D PhCs, however, they are not always periodic. Chirumamilla et al. [37] demonstrated a highly compact periodic HfO_2/W multilayer emitter. The spectral efficiency was 80% and could maintain its structural integrity after 6 hours at 1673K.

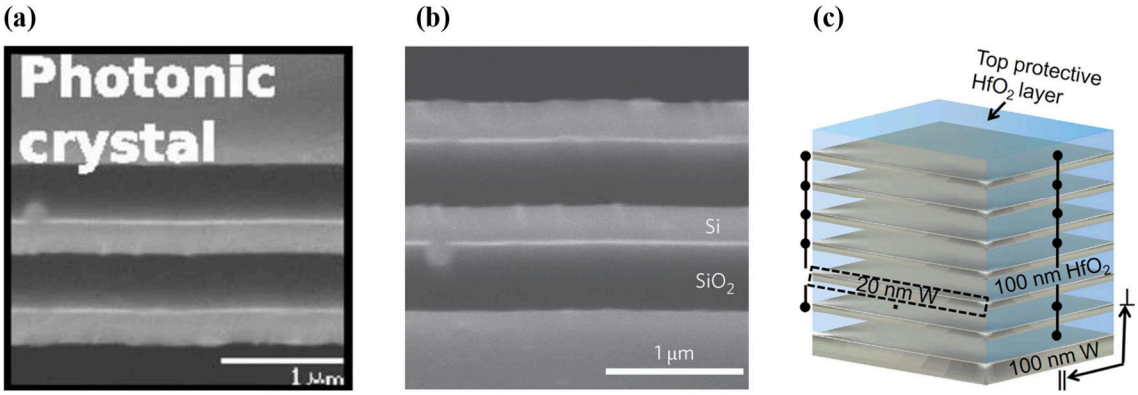


Figure 2-2 (a,b) Si/SiO_2 1D PhC [35] [36] and (c) HfO2/W multilayer

2D PhCs are designed by engraving periodic holes or patterns into a surface. These structures are typically more flexible and thermal shock resistant as compared to 1D PhC due to their monolithic construction. By adjusting the geometry of the periodic design, a suitable emittance spectrum can be achieved without any ARC, which prevents the risk of delamination due to stress caused by successively depositing materials with different thermal expansion coefficients. Two materials, which are the most common substrates in 2D PhCs are tungsten and tantalum, according to their thermal stability and high in-band emittance. Araghchini et al. [38] fabricated a tungsten 2D PhC emitter with a spectral efficiency of 31% at 1230 K. Yeng et al [39] built another 2D PhC tungsten-based emitter which exhibited a spectral efficiency of 45% and had no degradation after 10 hours of operation at 1200 K in vacuum. Rinnerbauer et al. [40] worked extensively on tantalum-based 2D PhC emitters, achieving a 54.4% spectral efficiency when operated at temperatures between 1200 and 1300 K.

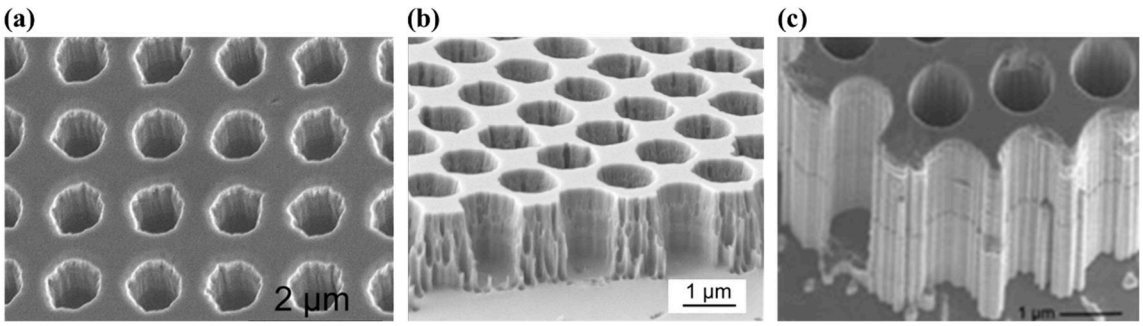


Figure 2-3 2D PhC (a,b) tungsten-based [38], and (c) tantalum-based [40] emitters

3D PhCs have a periodic index of refraction in all three dimensions, providing more degrees of freedom to design an emitter with greater control over its spectral and directional emissivity. However, due to their fabrication complexity, 3D PhCs production faces significant challenges. Aprin et al. [41] introduced a 3D PhC emitter consisting of HfO_2-coated tungsten with a high spectral efficiency of 67% which delivered a high in-band radiance at 20.3 W/cm^2. Moreover, Garin et al. [42] developed a 3D PhC emitter consisting of Si/SiO_2/Pt with a spectral efficiency of 49% at 1100 K which has no sign of degradation after an 8-hours durability test in a nitrogen environment. It is important to mention that neither of these 3D designs has yet been tested in complete TPV or STPV systems.

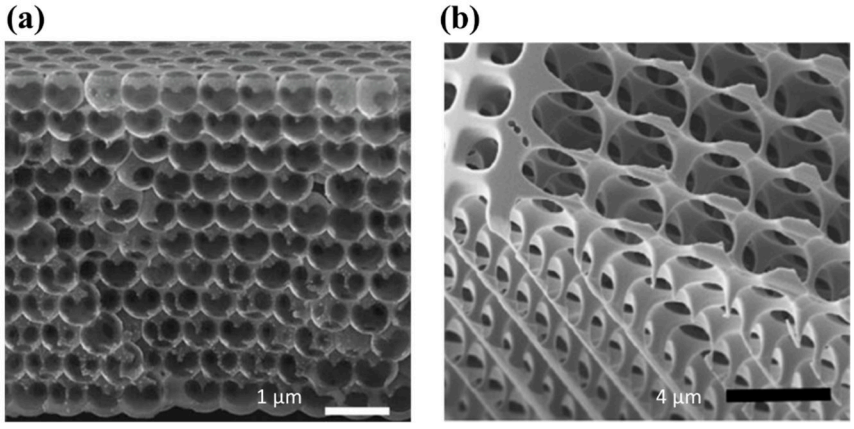


Figure 2-4 3D PhC (a) HfO_2-coated tungsten [41], and (b) consisting of Si/SiO_2/Pt [42]

Selective emitters like photonic crystals and multilayer materials offer great spectral control and can achieve higher efficiencies, but they are often complicated and expensive to make. On the other hand, bulk emitters are simpler, cheaper, and have proven thermal stability, making them easier to manufacture. Considering the challenges associated with PhC and multilayer emitters bulk emitters were utilized in this work as a practical option for creating a scalable and cost-effective TPV system that could be powered using single or multiple heat sources. In the next section, I will review the material-based emitters to explain why I chose this material for my bulk emitter design. As stated earlier, a bulk emitter refers to refractory material radiating photons without engineered spectral selectivity.

2.2.2 Tungsten-Based Emitters

Tungsten is frequently investigated as an emitter material in literature due to its excellent high-temperature performance. The following section reviews tungsten-based emitters, summarizing their properties, fabrication methods, and reported results.

Cokbas et al. [43] developed a tungsten emitter enclosed in a quartz bulb filled with argon or xenon to prevent oxidation at high temperatures. Tungsten was selected for its thermal stability and spectral behavior, emitting strongly in the visible and near-infrared where GaSb cells are most responsive, while suppressing longer wavelengths. Using a Fresnel lens and secondary concentrator, the system reached temperatures around 1900 K under solar concentrations of up to 4600X. At this condition, the reported TPV efficiency was 19%, increasing to 27% with spectral filtering.

Heinzel et al. [44] designed a 2D photonic crystal emitter by patterning tungsten surfaces with periodic gratings, using holographic lithography followed by SF_6-based dry etching. The grating periods ranged from 1.4 to 2.0 μm, with depths around 0.5 μm, aiming to enhance emission through surface plasmon coupling in the near infrared. The emitter was experimentally tested in vacuum and heated up to 1200 K, where spectral emissivity was measured using FTIR spectroscopy. Results showed a clear enhancement;

emissivity peaked at 70% around 1.6 μm, compared to about 30% for unstructured tungsten. Although the design showed strong wavelength and angle dependence, the experiment confirmed that micro-structuring tungsten surfaces can significantly improve spectral selectivity at high temperatures.

Lin et al. [45] experimentally demonstrated a three-dimensional tungsten photonic crystal emitter with a complete photonic bandgap structure tailored for TPV applications. The emitter was fabricated through a multilayer silicon-based process involving mold patterning, tungsten deposition, and chemical-mechanical polishing to build a freestanding structure with sub-micron periodicity. It was operated under vacuum and heated resistively up to ~1535 K, showing a sharp emission peak at 1.5 μm with a narrow spectral width of 0.9 μm. This emission is well-aligned with the GaSb bandgap, making it suitable for TPV conversion. Compared to a blackbody at the same temperature, the photonic crystal showed a much narrower spectrum and nearly four times the peak power density. Theoretical modeling suggested an optical-to-electric efficiency of around 34% and an electric power density of ~14 W/cm². These results highlight the strong spectral selectivity and high conversion potential of 3D tungsten-based PhC emitters, though the structure was not tested in a full TPV system.

Sai et al. [46] made tungsten surface gratings with tiny rectangular cavities to boost selective emission for TPV systems. They used electron beam lithography and dry etching on single-crystal tungsten, making patterns about 1 to 1.2 microns wide and up to 0.78 microns deep. Heated to 1400 K in an argon-hydrogen mix to avoid oxidation, these gratings had much higher emissivity in the near-infrared compared to flat tungsten, producing power densities near 20 kW/m² in the 0.9 to 1.7 micron range. The microcavity effect gave angle-independent emission that matches well with GaSb cells. While the structures might degrade above 1400 K due to surface diffusion, adding oxide coatings like HfO_2 could help protect them. Overall, this study shows tungsten gratings can be strong, reliable selective emitters for high-temp TPV applications.

Andreev et al. [47] developed a solar TPV system featuring a cylindrical tungsten emitter enclosed within a vacuum chamber to prevent oxidation. The emitter, illuminated by a 0.45 m² pseudoparabolic facet

mirror combined with a secondary quartz lens, achieved solar concentration ratios up to 4000X, allowing the tungsten to reach temperatures between 1500 and 2000 K. The system utilized 1×1 cm GaSb PV cells arranged around the emitter. Under direct sunlight, the STPV modules attained emitter temperatures near 1900 K, resulting in an estimated overall system efficiency of approximately 10%. The research highlighted the importance of spectral selectivity, sub-bandgap photon recycling through reflective coatings, and the effect of emitter aperture absorptance on efficiency. These findings underscore tungsten's suitability as a high-temperature emitter material when combined with effective optical concentration and environmental control for STPV applications.

Chen and Zhang [48] developed a one-dimensional complex tungsten grating by combining two binary gratings with different periods, which creates a broad and stable emission peak between 0.8 and 1.6 microns. Their simulations showed emissivity above 0.8 in this range, making it a good match for GaSb TPV cells. The grating uses shallow grooves, which makes it easier to fabricate and keeps performance consistent even if the ridge height varies by about 15%. The structure stays stable at high temperatures, due to tungsten's low thermal expansion,. Overall, this design offers a practical and scalable way to get efficient, selective emission from tungsten emitters in TPV systems.

Ungaro et al. [49] presented a solar TPV system using a planar tungsten absorber/emitter structure enhanced by laser micro texturing and a dielectric coating. The system was tested under simulated solar illumination, reaching emitter temperatures up to 1400 K in a vacuum environment. The tungsten substrate, chosen for its high thermal stability and reflectance, was coated with a 160 nm Si_3N_4 dielectric layer to tailor spectral emission and improve efficiency. GaSb photovoltaic cells with a bandgap of 0.67 eV captured the emitted radiation. The microtextured tungsten surface showed high solar absorptance (~90%) before and after annealing at 1700 K, confirming its thermal robustness. The experimental setup achieved an overall power conversion efficiency of 6.2% at a solar concentration factor of approximately 2500X, closely matching thermodynamic models.

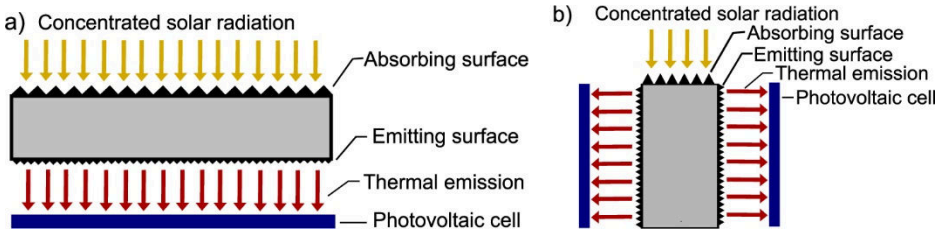


Figure 2-5 Diagram of a) a flat STPV system and b) a cylindrical STPV system, both with solar absorber and thermal emitter [49].

Kopper and Leite [50] did a thorough screening of bilayer emitters that can handle really high temperatures (around 1800 °C) for TPV systems. They found that tungsten substrates coated with thin layers like aluminum nitride (AlN) or magnesium oxide (MgO) work well. These bilayers improve the emission spectrum by cutting down on photons with energies below the PV cell bandgap, which means more of the emitted light can be converted to electricity. The AlN on tungsten showed about a 5.6% boost in efficiency compared to bare tungsten, making it a great match for GaSb cells. They also showed that tweaking the thickness of the coating helps balance efficiency and power output but stressed the importance of stability at high temperatures to keep the emitter durable. Overall, their bilayer approach looks like a practical way to get better performance from tungsten bulk emitters in TPV setups.

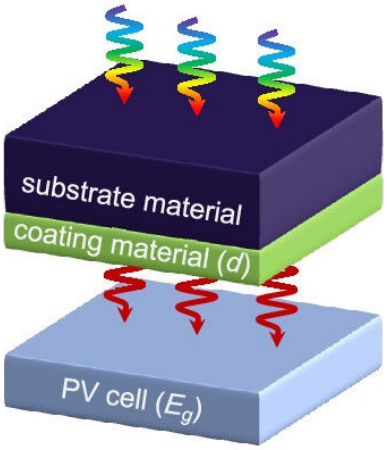


Figure 2-6 Bilayer emitter consisting of bulk substrate and a coating layer [50]

After reviewing the literature on tungsten emitters, it's clear that tungsten is the most practical choice for a bulk TPV emitter. It can withstand very high temperatures because of its high melting point and thermal stability, which is essential for efficient photon emission. Besides that, tungsten is also a great absorber, effectively converting incoming radiation into heat to maintain its temperature. Its excellent electrical conductivity means it can be heated efficiently by passing current through it, giving more flexibility in how the emitter can be operated. All these qualities make tungsten a dependable and versatile option for designing a bulk emitter.

2.2.3 Micro Heaters and Tungsten Integration

In this work one of the heat sources used to power the TPV system is a microheater in the form of a thin tungsten film heated via Joule heating. While Joule heating is not particularly useful for practical TPV systems, using Joule heating provides for a convenient method of raising the emitter temperature in a controlled manner, which is ideal for conducting experiments. In a practical multisource TPV system, the microheater could be powered using a fuel source or radiation rather than Joule heating used in the experiments conducted in this thesis.

A microheater is a compact heating device that produces heat via Joule heating, ultrasonic methods, or radiation. Its operating temperature is influenced by electrical, mechanical, and thermal factors, as well as by its materials and geometric configuration. The diameter of the resistive filament generally ranges from 100 nm to 100 μm. While early microheaters often employed metallic materials, modern high-temperature applications typically require ceramic-based materials due to their superior thermal resistance, leading to a shift toward metal-ceramic composites [51].

Microheaters offer several advantages, including low power consumption, rapid thermal response, efficient heat confinement, strong mechanical stability, and reliable fabrication yield [52]. Microheaters are

used as heating elements in fuel cells [53], and have further application in electronics and substrate heating [54].

Tungsten is commonly used in microheaters because of its excellent thermal and electrical properties, high melting point, and good thermal stability. It can operate at temperatures up to 1200 °C; however, it remains stable in oxygen-rich environments only up to around 400 °C [55]. Its relatively low cost also makes it a practical choice for reliable, high-temperature heating applications. Several studies have explored its suitability for microheater applications by examining film characteristics, deposition conditions, and thermal behavior on different substrates.

Verbrugghe et al. [56] investigated using tungsten thin films for integrated microheaters, specifically for gas sensor applications. They deposited the tungsten using DC magnetron sputtering on silicon substrates with a 1 μm SiO_2 insulating layer. The structure included a thin interface layer and a thicker top layer, with a total film thickness of around 600 nm. After annealing the samples at 500 °C for 30 minutes, the films showed low resistivity (27 μΩ·cm when sputtered at 0.1 Pa) and remained stable and well-adhered. Even after 300 hours of continuous operation at 400 °C, the heaters showed no signs of failure or resistance drift.

In another study, Xu et al. [57] designed a high-speed tungsten microheater for phase-change switching. This heater used an ultrathin 55 nm tungsten layer deposited by DC sputter on a sapphire substrate, chosen for its strong thermal conductivity and insulation. The structure was patterned using photolithography and reactive ion etching. Under rapid electrical pulses, the microheater reached temperatures up to 1664 K. It also held up well under stress; after 10,000 thermal cycles the resistance varied by less than 0.1%.

By selecting tungsten as the heating layer, and since it's commonly deposited using thin-film techniques, the focus now shifts to different sputtering methods. It is important to understand these methods for achieving good film quality and reliable microheater performance.

2.2.4 Deposition Processes

Surface engineering has come a long way, especially with the rise of plasma- and ion-based techniques that improve how coatings stick, how they're structured, and how well they perform. Due to advances in control systems and vacuum technology, these methods are now widely used in different industries. Figure 2-7 shows some of the main surface engineering methods currently used to improve material properties through thin coatings [58].

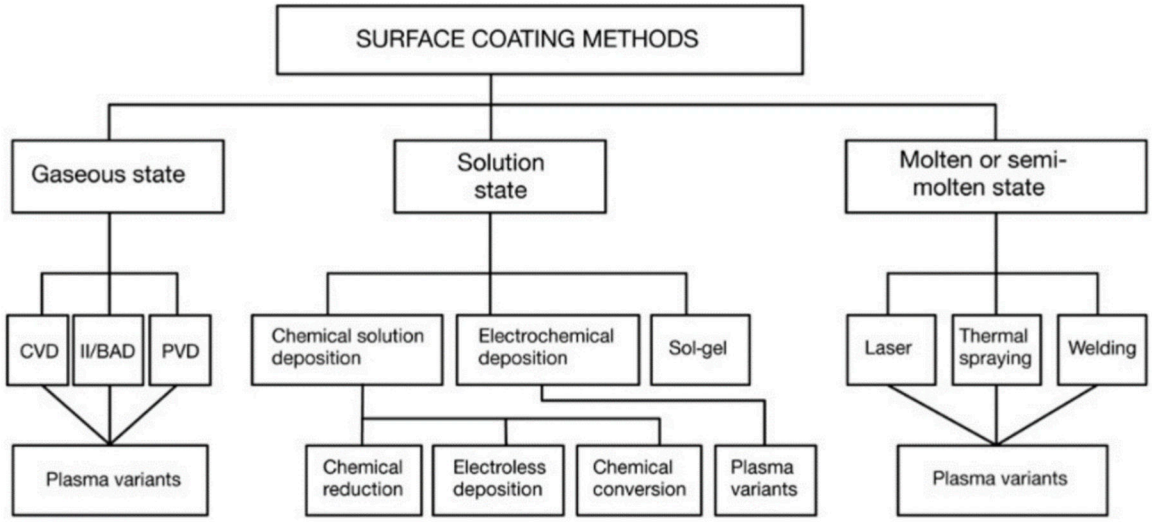


Figure 2-7 A general classification of surface engineering techniques [58].

In the following sections, the focus will be on surface coating methods that operate in the gaseous state, which are widely used for depositing thin, functional layers.

2.2.4.1 Gaseous State Processes

Gaseous state processes involve surface engineering techniques where the coating or treatment material transitions through a gaseous or vapor phase before being deposited or modifying the surface. The primary coating subgroups are chemical vapor deposition (CVD) and physical vapor deposition (PVD). In CVD, gaseous reagents serve as the source of coating material, while in PVD, at least one coating material is evaporated or atomized from a solid within the coating chamber [58].

Chemical Vapor Deposition (CVD) is a vacuum-based technique where reactive gases form a solid coating on a substrate. It's commonly used to improve surface durability, reduce friction, and enhance thermal performance. CVD can also be combined with PVD layers to achieve better overall coating properties [59].

Physical Vapor Deposition (PVD) is a method where material from a solid source is turned into vapor and then deposited onto a surface, building the coating atom by atom. The film can be just a few atomic layers thick or several microns. It doesn't just change the surface, it also affects the layer between the coating and the substrate, which can influence the final properties. PVD is usually done in vacuum or plasma to keep the process clean and reduce contamination [60].

PVD is widely used for thin, durable coatings and includes methods like sputtering. Here, the focus is on PVD, since previous studies used DC magnetron sputtering, which is a common PVD technique, to deposit tungsten layers.

2.2.4.2 PVD Deposition

PVD processes involve atomizing or vaporizing material from a solid source and depositing it onto a substrate to form a coating. PVD is a reliable vacuum coating method widely used to improve wear and corrosion resistance. It plays a key role in many functional applications, from cutting tools and molds to optical coatings, decorative parts, dies, and blades [61]. Additionally, PVD can produce coatings with excellent adhesion, uniform layers, tailored structures, graded properties, controlled morphology, and a wide variety of materials and characteristics [62]. Evaporation and sputtering are the two main PVD coating methods in the gaseous state. Both involve removing material from a target at low pressure and depositing it onto a substrate. Evaporation uses high-vacuum conditions, which reduce gas adsorption but produce larger grains and weaker adhesion. It's faster but better suited for thicker coatings where surface detail isn't critical. Sputtering, on the other hand, offers better control over surface quality, roughness, and composition.

Although slower and sometimes limited by substrate temperature, it's still widely used and continues to evolve to meet new demands [63].

2.2.4.3 Evaporation and Sputtering

In this section, two different PVD methods are explored to better understand their role in coating development. PVD reactors typically consist of a vacuum chamber and two electrodes connected to a high-voltage power supply, as shown in Figure 2-8.

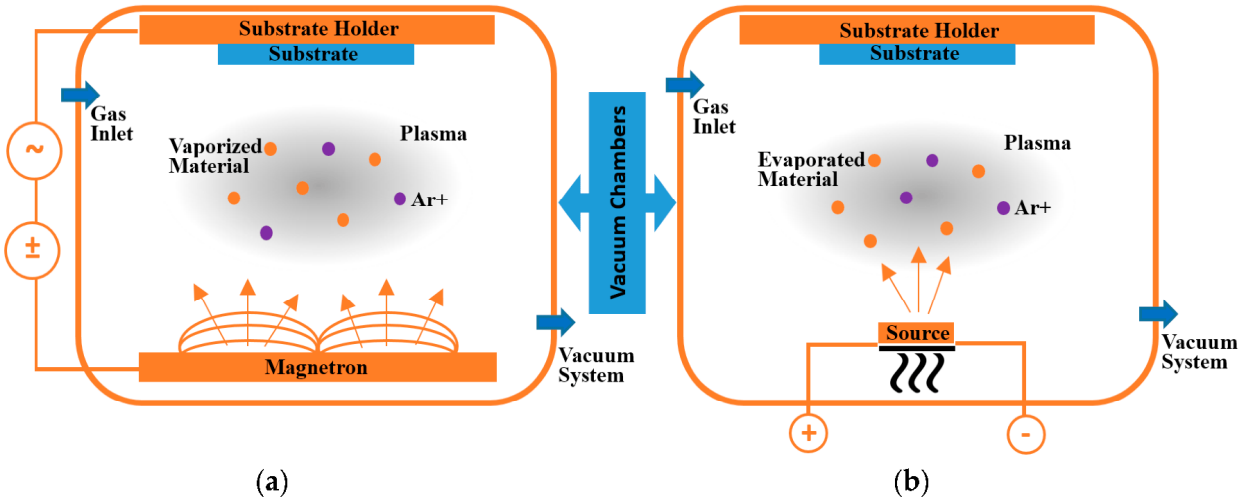


Figure 2-8 Illustration of two common PVD techniques: (a) sputtering and (b) evaporation using ionized argon (Ar^+) gas [64]

In magnetron sputtering, thin films are created by ejecting atoms from a target material placed near a magnetron in a vacuum chamber. An inert gas is introduced and accelerated by a high voltage between the target and substrate, causing ionized atoms to bombard and dislodge atoms on the target which are subsequently deposited onto the substrate. This ion-driven process forms a solid thin layer. The substrate can also be cleaned beforehand by reversing the voltage, a step known as cathodic cleaning [65].

In evaporation, a solid material is heated using techniques like resistive heating, inductive coils, or electron and laser beams until it turns into vapor. In e-beam evaporation, the target acts as a cathode and is

bombarded by electrons in high vacuum until it reaches a temperature high enough to release atoms. These atoms interact with gas molecules in the chamber, creating plasma that accelerates the sputtered species and enables the formation of dense, well-layered coatings with improved adhesion to the surface [60].

Compared to evaporation, sputtering is a cleaner method that produces denser films with less stress, thanks to its low-to-medium temperature operation. The deposition rate and film stress can be adjusted by tuning power and pressure, and larger targets help improve uniformity and control over thickness. Still, there's a chance of contamination from impurities in the source, and some materials can't be used due to their high melting points. While evaporation doesn't offer the same level of thickness control, it allows for high deposition rates with fewer limitations on film thickness [66]. Table 2-1 compares the main features of these two PVD methods.

Table 2-1 Sputtering versus Evaporation parameters comparison [64]

Parameters	Sputtering	Evaporation
Vacuum	Low	High
Deposition rate	Low (except for pure metals and dual magnetron)	High (up to 750,000 A min^{-1})
Adhesion	High	Low
Absorption	High	Less absorbed gas into the film
Deposited species energy	High (1–100 eV)	Low (~0.1–0.5 eV)
Homogeneous film	More	Less
Grain size	Smaller	Bigger
Atomized particles	More Dispersed	Highly directional

2.2.4.4 Sputtering Process

Sputtering is a technique where energetic ions from heavy inert gas hit the surface of a target, transferring momentum and physically knocking atoms off the target. These atoms are mostly ejected in atomic form and used to form thin films [67]. To create ion bombardment in sputtering, the chamber is filled with an inert gas like argon at low pressure, and a discharge is generated between the cathode (target) and anode (substrate). Argon ions strike the target with energies between 100 and 1000 eV, ejecting atoms that deposit onto the substrate. In magnetron sputtering (Figure 2-9), magnetic fields are added to trap electrons near the target, increasing plasma density and sputtering efficiency while reducing unwanted

substrate heating. Depending on how the magnetic field lines are arranged, the setup can be balanced or unbalanced. Unbalanced magnetrons allow plasma to extend toward the substrate, enhancing low-energy ion bombardment and improving film growth [68].

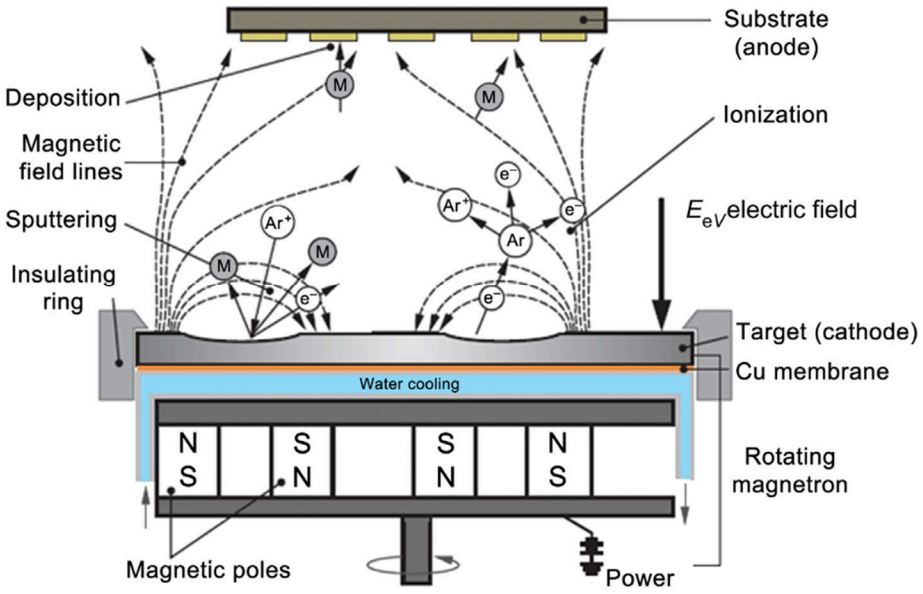


Figure 2-9 Diagram of a DC unbalanced magnetron sputtering setup [68]

Sputtering can be performed using direct current (DC), pulsed DC, or radiofrequency (RF) modes [69]. The basic setup for sputtering involves a direct current diode glow discharge with two electrodes: a negatively biased cathode and a positively charged anode. In this system, deposition can occur with the substrate grounded. If a constant voltage is used, it's called DC discharge; if the voltage pulses or switches polarity, it becomes pulsed or RF discharge, respectively. Each method has its pros and cons, particularly for depositing ceramics [70]. Sputtering begins with substrate preparation, where proper cleaning is key to achieving good coating adhesion. It’s often recommended to clean the substrates in an ultrasonic bath before placing them inside the chamber [71]. A key advantage of a vacuum sputtering chamber is its dual functionality, as it can be used for both substrate cleaning and subsequent coating deposition [65].

After the substrates are placed in the holders within the vacuum chamber, the deposition process follows four key steps, as outlined in Figure 2-10:

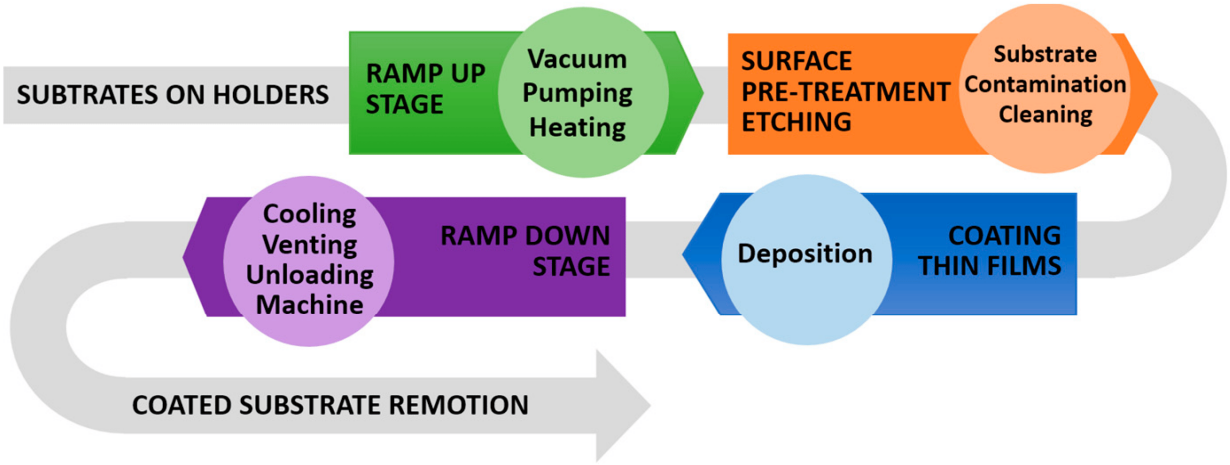


Figure 2-10 The processing flow for a classic PVD sputtering process [64].

The sputtering process begins with the ramp-up stage, where the substrate holder in chamber is gradually heated using heating element system, and pressure is reduced using vacuum pumps down to 10^{-5} bar with the primary pump and as low as 10^{-7} bar with the high-vacuum pump. Next comes etching, where the substrate is cleaned through cathodic plasma etching to remove surface contaminants and improve adhesion, which depends on factors like substrate hardness and surface quality. In the coating phase, the target material such as titanium, aluminum, or tungsten is deposited onto the substrate. Finally, during ramp down, the system is cooled and slowly returned to room temperature and ambient pressure using a dedicated cooling setup [64].

The absorber–emitter in this work as shown in Figure 2-11 has the form of a ceramic-based bulk emitter with thin films sputtered onto its surface. This type of emitter was chosen for its straightforward fabrication, lower cost, and proven thermal stability compared to more complex selective emitters. AlN is used as the substrate because it combines high thermal conductivity with excellent electrical insulation and can withstand high operating temperatures. One side of the ceramic is coated with a tungsten layer, applied by DC magnetron sputtering, which works both as an absorber of incoming radiation and as a resistive heater through Joule heating. The other side functions as the emitter, radiating within the desired spectral range for TPV conversion. This design takes advantage of tungsten's high melting point, strong thermal stability, and suitability for sputtering, resulting in a robust and scalable approach for practical TPV systems.

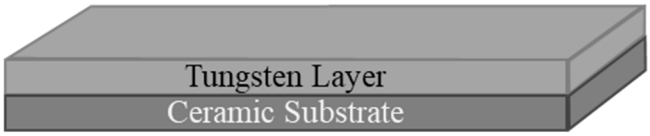


Figure 2-11 Absorber-emitter schematic

2.3 TPV Cell Overview

TPV systems work by converting heat, which is radiated from a hot emitter directly into electricity using PV cells [72]. This technology has been steadily gaining attention thanks to its potential in areas like thermal energy storage and waste heat recovery. In recent years, significant improvements in TPV cell performance have brought technology closer to practical, real-world applications, making it an exciting area of research and development [73].

This section focuses on the TPV cell, covering its history and the mechanism by which it generates electricity. It also highlights the real-world advantages of TPV technology and examines various TPV systems by analyzing their composition. Finally, it reviews previous TPV systems related to hybrid configurations and discusses the existing gaps and challenges in this area.

2.3.1 Historical Overview

TPV technology dates to around 1956, when Aigrain first introduced the concept in a series of lectures at MIT [74]. That same year, Kolm and others at MIT Lincoln Laboratory demonstrated early TPV systems. During the first couple of decades, most research in the US focused on military applications which were quiet power generators fueled by combustion. By then, the main heat sources (solar, nuclear, and combustion) and basic spectral control methods like selective radiators and filters had already been identified [75]. Silicon and Germanium were the primary PV cell materials studied; silicon needed very high temperatures, which brought engineering challenges, while Germanium worked at lower temperatures

but with limited efficiency [75]. Development slowed in the mid-1970s as the US Army favored thermoelectric generators and industry faced difficulties during the oil crisis [75].

Still, the energy crisis renewed interest in TPV, especially solar TPV (STPV), along with improvements in III–V PV materials such as gallium antimonide (GaSb) and indium gallium arsenide (InGaAs), plus advances in concentrator technologies [75]. Experience gained from solar PV concentrators and high-efficiency fossil fuel burners, like rare earth oxide and ceramic radiant burners, helped make TPV systems more efficient [76].

In the 1990s, TPV returned with military and space applications driving new companies to produce GaSb cells licensed from Boeing. One example was a propane-powered combined heat and power stove, which was tested in the late 90s [77]. TPV generators using radioisotope heat sources were considered for deep space missions, where sunlight is scarce. Hybrid cars equipped with combustion-TPV generators were also demonstrated [78]. Around this time, industrial waste heat recovery became an exciting new application [74], and fundamental research started on Near-field TPV (NF-TPV), which uses nanoscale gaps to boost photon flux to the PV cell and enhance power output beyond classical limits [79].

2.3.2 Fundamentals of TPV Energy Conversion

Before explaining how a TPV cell operates, it's important to understand the basics of semiconductors. A semiconductor is a material with electrical conductivity that lies between that of a conductor and an insulator [80]. The invention of the transistor in the late 1940s and early 1950s greatly advanced the understanding of solid-state semiconductor theory [81].

Semiconductor materials come from group IV elements, or combinations of groups III-V and II-VI (shown in Figure 2-12), leading to different properties. Si, a group IV element, has atoms arranged in a stable lattice where each atom bonds to neighbors with eight electrons. Due to its well-established technology, silicon is the most used semiconductor in solar cells [82].

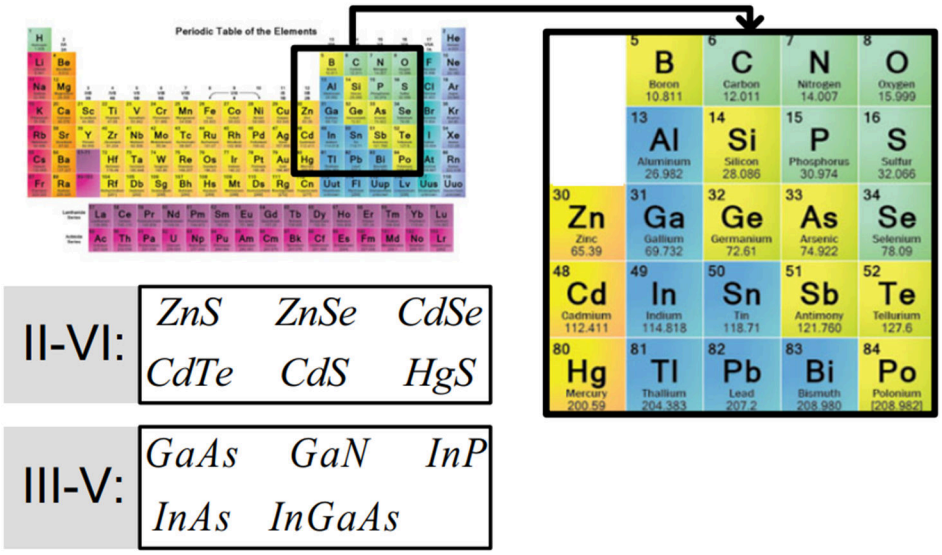


Figure 2-12 The periodic table showing the semiconductor groups [83]

In semiconductors, electrons usually stay locked in the valence band, so they can't conduct electricity. But when energy from heat or light hits the material, some electrons get enough energy to jump across the band gap into the conduction band, where they can move freely and create an electric current. This energy gap between the valence and conduction bands, named band gap, plays a big role in how the material behaves and how it responds to external energy sources [84].

To change how semiconductors conduct electricity, impurities are intentionally added through doping. When atoms from group V are added to a group IV semiconductor, it becomes N-type, gaining extra free electrons. If group III atoms are added instead, the material becomes P-type, with more "holes" that act like positive charges. When N-type and P-type materials come together, electrons and holes move toward each other, forming a region without free charges called the depletion zone. This zone creates an electric field and voltage that help separate charges which is an important part of how solar cells produce electricity.

When N-type and P-type materials are joined, the extra electrons in the N-type side naturally move toward the P-type side, while the holes in the P-type side shift toward the N-type side. As electrons leave

the N-type region, they leave behind positively charged ions, and as holes move away from the P-type side, negatively charged ions remain. This exchange creates an electric field at the junction, forming a depletion region without free charge carriers. This electric field generates a built-in voltage, which is essential for devices like photovoltaic cells to function.

TPV systems, like Solar cells, utilize this effect to produce electricity. The N-type layer, rich in electrons, provides negative charge carriers that, when energized by sunlight, flow toward the cell's front surface to create current. The P-type layer, with its electron "holes," acts as positive charge carrier. When these two layers meet, the PN junction forms an electric field that pushes excited electrons towards electrical contacts on the cell when light is absorbed, generating a steady flow of electric current.

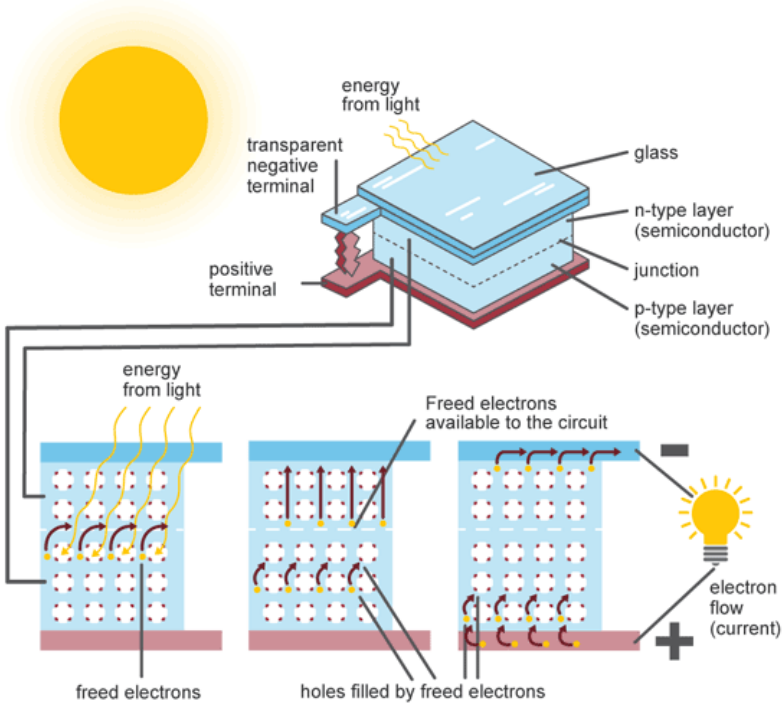


Figure 2-13 Schematic of a solar cell showing the n-type and p-type semiconductor layers, the PN junction, and the flow of electrons generated by light energy that produces electric current [85]

Key performance parameters of solar cells can be derived from the I–V characteristic curve, as illustrated in Figure 2-14 [86]. The I–V curve of a solar cell is generated by varying the voltage applied to

the cell and measuring the resulting current, then plotting current versus voltage. Its shape is influenced by factors such as material properties, doping concentration, and temperature. Key points on the curve include the short-circuit current (I_{SC}), where the current is maximum at zero voltage, and the open-circuit voltage (V_{OC}), the maximum voltage at zero current. The maximum power point (P_{mp}) represents the optimal operating condition where the product of current and voltage is highest, characterized by the voltage at maximum power (V_{mp}) and current at maximum power (I_{mp}) [87].

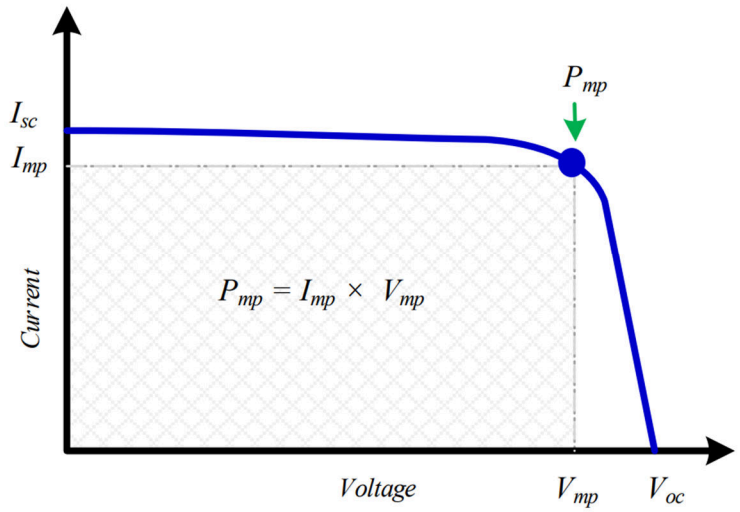


Figure 2-14 IV characteristic [86]

In a multisource TPV system, the addition of auxiliary inputs raises the emitter temperature, which in turn increases the radiative flux reaching the cell. As a result, both I_{SC} and V_{OC} would shift upward compared to a single-source case. In practical terms, the I–V curve would move toward higher current and voltage values, leading to a greater maximum power output. The more power delivered to the emitter, the higher the corresponding electrical generation from the TPV cell.

2.4 Background Studies on TPV Systems

This section reviews previous experimental TPV systems, focusing on the different heating methods used, the types and structures of emitter materials, and the TPV cells involved. Important details such as operating temperatures, efficiencies achieved, use of spectral filters, and the design of optical cavities are also examined. Finally, it is noted whether cooling systems were used, and a clear overview of each system's overall setup, performance, and power output is provided.

Considering powering TPV systems with fuel, Chan and colleagues [35] built a small, chip-scale TPV system powered by propane combustion in a silicon microreactor. The heat generated in the microreactor (up to about 800 °C) is transferred to a specially designed PhC emitter that focuses the thermal radiation on wavelengths best suited for their low-bandgap GaInAsSb solar cells. These cells, cooled by water, convert the radiation into electricity, while a power tracker ensures the system outputs electricity turn into useful current and voltage level. Under a thermal input of 13.7 W, the system produces 344 mW of electrical power with an efficiency of 2.5%, closely matching their theoretical predictions.

The authors also looked at where energy is lost, such as unwanted out-of-band photons and heat escaping from the reactor's sides, and suggested improvements to reduce these losses. They proposed that with better emitter designs, like metal photonic crystals and filters, efficiencies over 30% are achievable at higher temperatures (above 1000 °C). This work shows a promising step toward compact, efficient power sources that combine advanced materials and smart design, making portable TPV generators a real possibility for the future.

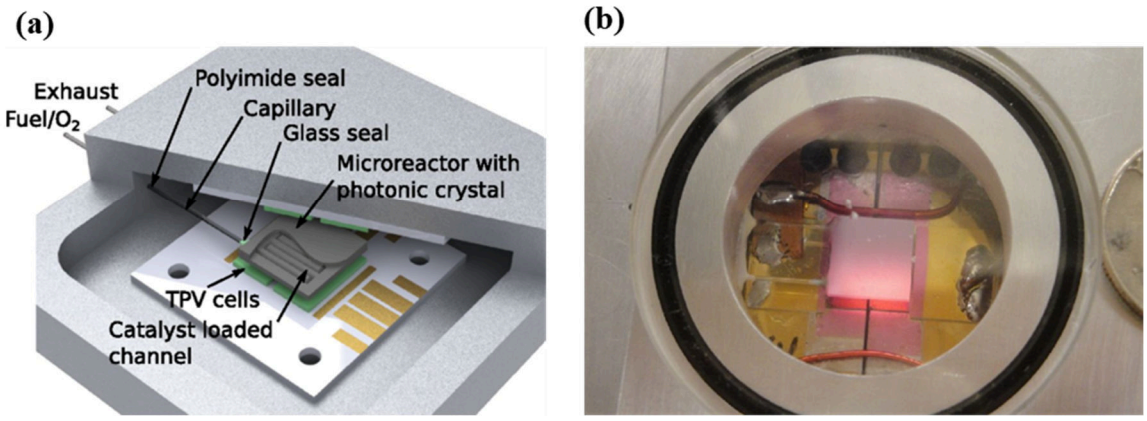


Figure 2-15 (a) CAD model with labels of the experimental micro-TPV system, (b) the micro-TPV system during operation ***[35]***

In another article, Doyle and colleagues [88] developed and tested a compact 25-Watt TPV power source combined with a rechargeable battery, to demonstrate a hybrid power application. Their system used propane combustion at around 103.5 KPa (15 psi), with a swirl air mixer to keep the flame stable and heat distribution even. The heart of the system was an emitter made of platinum foil coated with an anti-reflective layer to boost emission in the useful spectral range, supported by a tungsten backing that provided durability and could withstand high temperatures due to tungsten's high melting point (about 3422 °C). While operating under oxygen-enriched conditions, the emitter reached roughly 1458 K (1185 °C), achieving uniform heat and a higher fraction of radiation matching the PV cells' absorption spectrum. To improve efficiency, the emitter and GaSb PV cells were enclosed in a gold-plated chamber that helped recycle photons by reflecting those with too little energy back to the emitter. Additionally, the GaSb cells had dielectric filters directly applied to reflect about 80% of sub-bandgap photons, which reduced the amount of wasted heat.

The cells themselves were arranged in a carefully designed series-parallel "shingled" layout, optimizing voltage and current output. These GaSb cells had a bandgap close to 0.72 eV, with a fill factor (FF) of about 0.69 and a V_{OC} near 0.48 V per cell. To keep the cells cool, the system used copper fin heat sinks cooled by a powerful fan spinning at 9800 rpm, which kept the increase in cell temperature to less

than 20 °C and maintained their temperature below 80 °C during operation. Overall, this system achieved about 28 W of electrical power with an efficiency close to 3%. This work nicely illustrates how combining propane combustion heating, a tungsten-supported platinum emitter with specialized coatings, smart spectral filtering, and effective cooling can deliver a stable and reasonably efficient TPV power source suitable for portable applications.

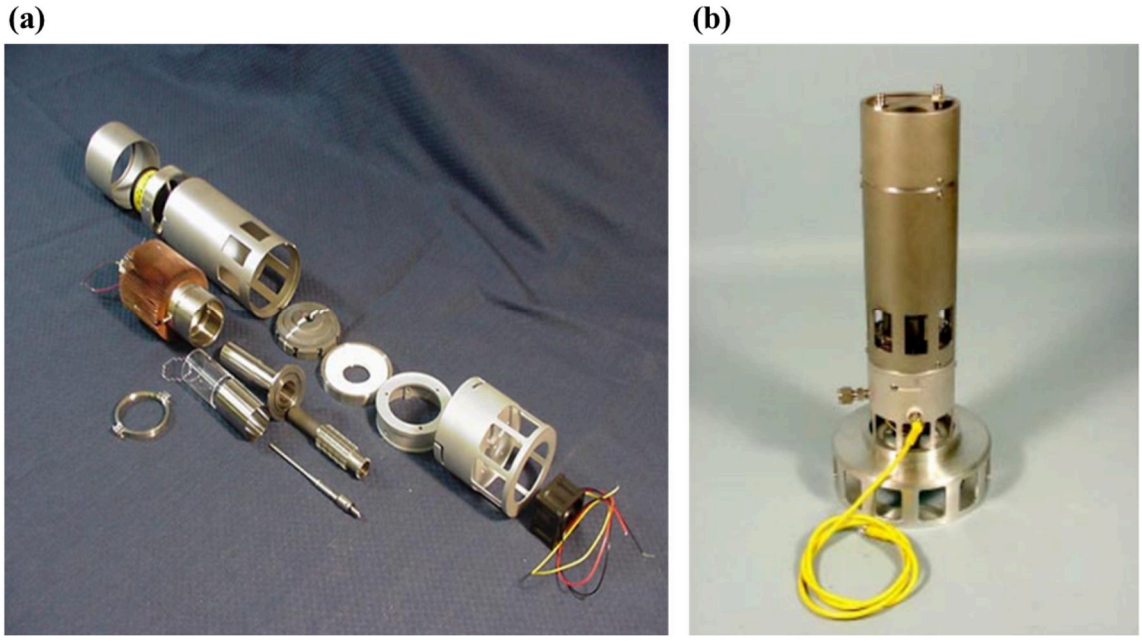


Figure 2-16 (a) Demonstration of prototype components, and (b) assembled prototype [88]

One of the studies that employed Joule heating to raise the emitter temperature was conducted by Liu et al [89] which compares the experimental performance of two common TPV cells: 0.72 eV GaSb and 0.59 eV InGaAs, under radiation temperatures ranging from 1073 K up to 1473 K. The testing setup uses a tungsten emitter heated resistively inside a quartz crucible and housed in a vacuum chamber to reduce heat loss and prevent oxidation. This design allows the emitter to reach stable temperatures as high as 1200 °C. The thermal radiation from the tungsten surface is directed at the TPV cells placed at controlled distances of 8 and 10 cm. Both GaSb and InGaAs cells are actively cooled with water-cooled heat sinks attached to their backsides to keep cell temperatures stable during operation. Moreover, the system did not include

spectral filters, so the spectral control depends on the tungsten emitter's emission characteristics and the cell properties themselves.

The results show that as the radiation temperature increases, both cells experience rises in I_{SC} and V_{OC}. However, the InGaAs cells produce higher power output and efficiency at lower temperatures because of their smaller bandgap, while GaSb cells perform better at higher temperatures. At 1200 °C and a distance of 10 cm, the maximum efficiencies measured were 28.91% for InGaAs and 23.10% for GaSb. Interestingly, the FF of the GaSb cell increased with temperature, mainly due to a decrease in series resistance, whereas the FF of the InGaAs cell decreased, linked to changes in shunt resistance. Overall, the study highlights how the choice of cell bandgap impacts performance depending on emitter temperature, suggesting InGaAs cells are better for lower-temperature TPV systems, while GaSb cells suit higher-temperature conditions.

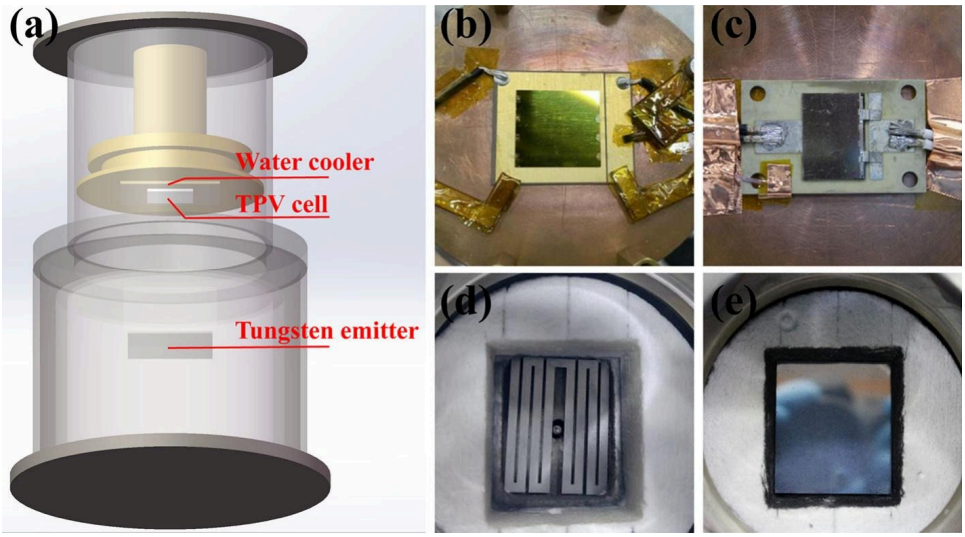


Figure 2-17 (a) TPV system sketch, (b,c) GaSb and InGaAs cell with water cooling on the back surface, (d) heating elements, and (e) tungsten emitter within a quartz crucible [89]

In another investigation conducted by Hang [87] a TPV system was developed that uses Joule heating to raise the emitter temperature, reaching up to about 1300 °C. The emitter was made by coating a substrate with a special high-temperature fractal paste and suspending it with tensioned Inconel wires to ensure even heating and precise alignment with the PV cells. For the PV side, low-bandgap InGaAs cells

from MicroLink Devices were used, with sizes between 0.25 and 1 cm². These cells were bonded using thermally conductive tape since direct bonding was challenging. Cooling was handled by a microchannel heat sink fed by water kept below 5 °C, which effectively kept the cells cool even when the emitter was very hot.

The system relied on the natural spectral properties of the emitter and the cells. The distance between emitter and cells was kept around 3 mm to maximize radiative transfer. The researchers carefully measured losses and found conduction through the suspension wires was minimal (less than 1%), while convection losses ranged between 6 and 8%, depending on the temperature. Electrical tests showed that as the temperature of the emitter increased both current and voltage from the cells increased. However, the overall power conversion efficiency stayed at about 1.1% at 950 °C, mainly because the emitter's spectrum didn't perfectly match the cells' absorption and because of some resistance from the bonding method.

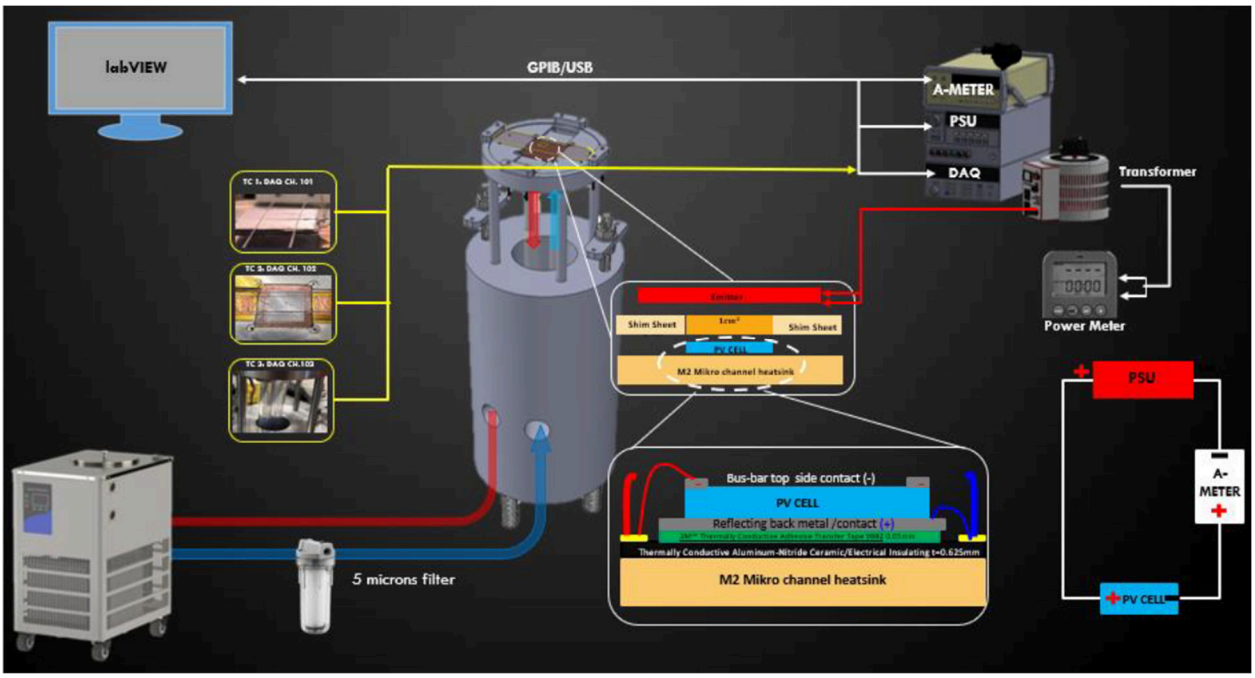


Figure 2-18 Overall demonstration of components of TPV system [87]

Talebzadeh et al. [90] experimentally studied a TPV system that used a Joule-heated tungsten filament embedded in a ceramic body as the heat source, integrated with a hemi-ellipsoidal optical cavity to enhance photon recycling. The emitter was spray-coated with black paint for uniform emission and positioned at one focal point of the cavity, whose interior was polished to a specular finish and extended with an aluminum ring to complete the geometry. Silver-coated annular reflectors with varying width-to-diameter ratios ($\omega/a = 0–0.8$) were installed at the minor axis, tuning the recycling factor (F_{rec}) from 0 to 0.735. Radiation was transmitted through a fused silica viewport onto a commercial GaSb PV cell, mounted outside the vacuum chamber and cooled by a fan. The setup operated under high vacuum (~10 mTorr) to suppress convection losses, with temperatures measured using K-type thermocouples and electrical output determined from I–V characteristics.

Two input powers were tested: 15 W and 30 W. At 15 W, emitter temperature rose from ~630 K ($F_{rec} = 0$) to ~900 K ($F_{rec} = 0.735$), while PV output increased from 0.045 μW/cm² to 9.62 μW/cm², an enhancement factor of over 210X. At 30 W, the emitter temperature increased from ~770 K to ~1100 K, with PV output rising from 1.94 μW/cm² to 155.7 μW/cm², corresponding to an enhancement factor of ~80X. Although absolute power densities were modest due to the large emitter–cell spacing, the results clearly demonstrated that photon recycling substantially improves emitter temperature and in-band photon flux.

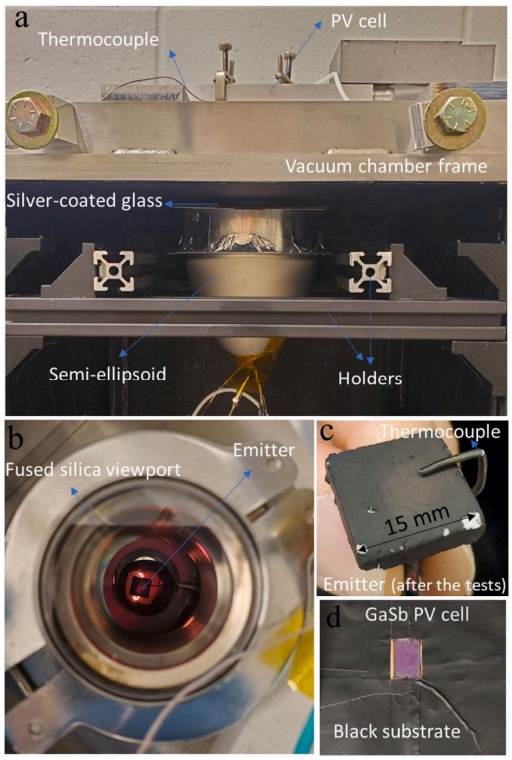


Figure 2-19 Experimental configuration for studying photon recycling effects on emitter temperature and output power [90]

Focusing on non-contact, light-driven heating methods, López and colleagues [22] improved the accuracy of TPV efficiency measurements by carefully considering the optical view factor (VF) between the emitter and the cell. They built an experimental setup where the emitter-to-cell distance is kept between 0.4 and 0.9 mm, resulting in high VFs from 0.91 to 0.98. This close arrangement allows multiple reflections between the emitter and the cell, forming an optical cavity similar to those found in practical TPV systems, and enables direct measurements of the conversion efficiency without relying on assumptions such as perfect blackbody behavior or estimates of the emissivity. Their emitter is a graphite surface heated by a 500 W continuous-wave laser at 915 nm, reaching temperatures up to 1592 °C as measured by a calibrated pyrometer. The TPV cells used are InGaAs devices with gold back reflectors from Antora Energy. Using a water-cooled calorimeter and a Peltier controller, these cells are actively cooled, maintaining temperatures near room temperature (around 30 °C).

The system achieved a peak TPV efficiency of 26.8% at 1480 °C and produced electrical power densities exceeding 4.3 W/cm² at 1592 °C. The authors highlight how important it is to maintain VFs for

realistic efficiency and power density measurements, since lower VFs can hide losses like series resistance. They also point out the difficulty in accurately measuring the effective cell illumination area because of partial masking from the holder, which can affect the precision of power density results.

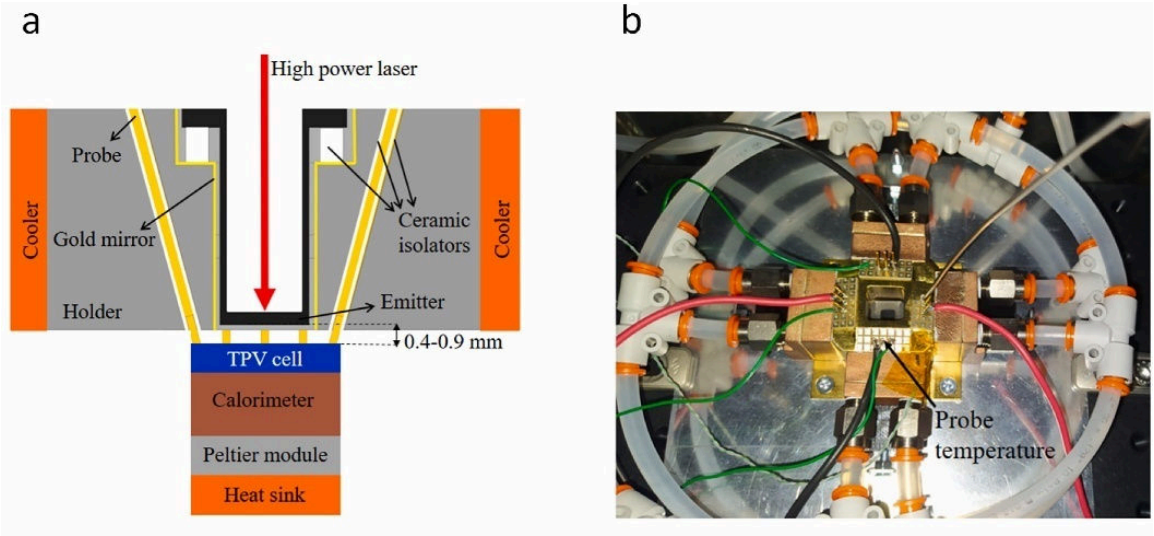


Figure 2-20 (a) Sketch of major components of the TPV system, and (b) top view of the setup including refrigration system [22]

Furthermore, Ungaro and his team [49] demonstrated a solar thermophotovoltaic system that uses nanostructured tungsten surfaces to boost efficiency under simulated sunlight. Their design includes a flat tungsten substrate with a laser-microtextured absorbing surface coated with an anti-reflective layer, along with a dielectric-coated emitting surface tuned to match the GaSb cell's bandgap around 0.67 eV. They used GaSb cells with an active area of 1.48 cm² and FF near 0.61, arranged in series on copper bases. Illumination came from an 808 nm continuous-wave laser diode stack, focused to simulate up to 2500 suns, comparable to what Fresnel lenses can concentrate. The whole system was kept in a vacuum chamber at about 10 mTorr to limit heat loss by convection and protect the materials. They controlled the emitter temperature up to roughly 1200 °C and placed the cells just 3 mm away to maintain a high VF of about 86%. The cells were cooled actively with water-cooled copper heat sinks, keeping them near 30 °C. A glass window filtered out longer wavelength IR to help reduce cell heating.

Their measurements showed the system reached a maximum efficiency of 6.2% at 149 W of laser power. This closely matched their thermodynamic model, which identified major losses from thermal emission on non-absorbing surfaces (about 23.6%), reflection (10%), and cell inefficiency (22.4%). The model also suggested that improving the cell's voltage and FF, along with adding a hot mirror filter, could push efficiency beyond 11% and up to 20% with ideal spectral control.

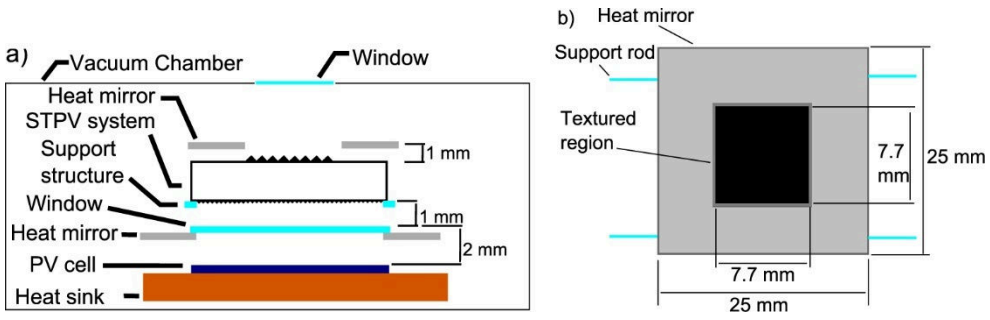


Figure 2-21 (a) Cross section of schematic, and (b) top view diagram of system setup [49]

In another study, Lenert et al. [21] developed a solar thermophotovoltaic (STPV) system that combined advanced nanostructures to improve efficiency under concentrated sunlight. They used a multiwalled carbon nanotube (MWNT) array as a broadband solar absorber that captures nearly all incoming sunlight. This absorber was integrated with a one-dimensional silicon/silicon dioxide photonic crystal emitter designed to selectively emit thermal radiation matching the bandgap of the InGaAsSb photovoltaic cells (around 0.55 eV). Both the absorber and emitter were fabricated on the same silicon substrate, ensuring efficient heat transfer between them.

The system was tested inside a vacuum chamber maintained below 0.5 Pa to minimize heat loss through convection and conduction. A xenon arc lamp was used to provide simulated solar irradiance at intensities ranging from 10 to 75 W/cm², roughly equivalent to up to 2500 suns of concentration. Although the emitter temperature was not directly measured, it was estimated to reach about 1285 K based on the electrical output of the PV cells and thermal emission modeling. The InGaAsSb cells were actively cooled

using water-cooled copper heat sinks, maintaining stable temperatures near room temperature throughout the experiments.

The STPV device achieved a peak efficiency of 3.2%, which is about three times better than previous results even at higher solar concentrations. This improvement comes from the nanophotonic design of the absorber and emitter, along with a carefully balanced emitter-to-absorber area. The authors believe that by enhancing the PV cells, adding spectral filters, and scaling the device, efficiency close to 20% could be achieved, highlighting strong potential for compact, efficient STPV systems.

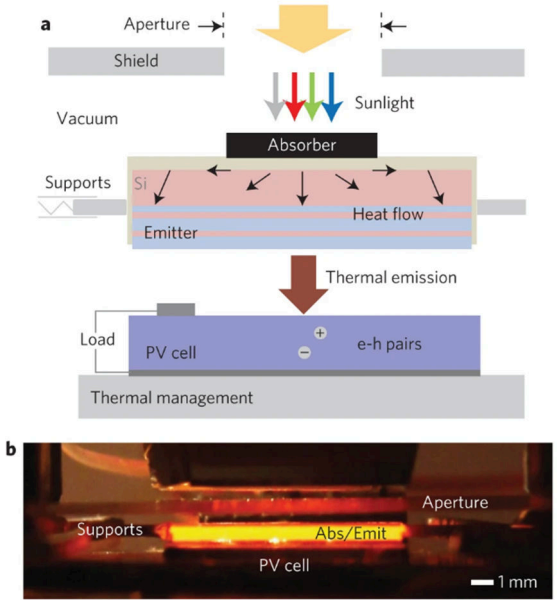


Figure 2-22 (a) Sketch of the TPV system, and (b) realistic vacuumed setup [21]

Employing concentrated solar irradiance, Datas and Algora [91] developed and tested a complete STPV system that used a Fresnel lens paired with a meniscus lens to concentrate sunlight by about 3183 times onto a tungsten cylindrical emitter coated with HfO_2. The emitter was placed inside a quartz chamber filled with argon to prevent oxidation and reduce heat loss through convection. Surrounding the emitter was a hexagonal TPV generator made up of 24 Germanium cells arranged in six shingled modules. These cells

were mounted on water-cooled brass heat sinks with thermal grease to ensure good cooling and electrical contact.

Outdoor tests under solar irradiance between 750 and 800 W/ m² showed the system produced short-circuit current densities (J_{SC}) up to 0.95 A/cm² and power densities around 62 mW/cm², with an overall solar-to-electric efficiency of about 0.8%. The relatively low efficiency was mainly due to cell overheating where temperatures reached about 120 °C, and losses in the concentrator optics that limited the emitter temperature. The authors noted that better cooling, improved electrical contacts, and enhanced concentrator performance could push efficiencies beyond 5%, with models suggesting more than 10% efficiency if the emitter and cavity design were further optimized.

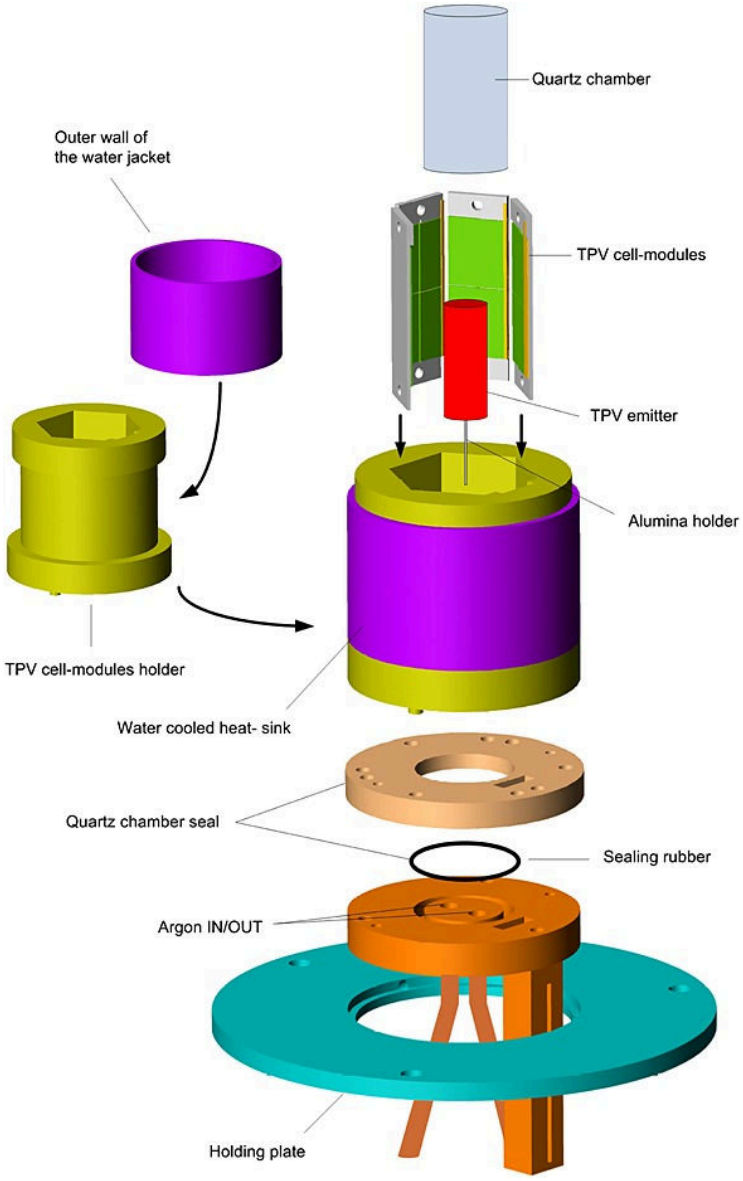


Figure 2-23Exploded view of the components making up the STPV system prototype [91]

With a halogen lamp serving as the heat source, LaPotin et al. [73] reported a TPV system that set a new efficiency benchmark, achieving more than 40% conversion from heat to electricity. The setup was designed with thermal energy grid storage (TEGS) in mind, operating with a tungsten emitter heated to extremely high temperatures, between 1,900 °C and 2,400 °C. To replicate the emitter's spectrum in a controlled setting, the team used a tungsten–halogen lamp paired with concentrator optics. Two types of

custom-engineered, multi-junction III–V TPV cells were evaluated: a 1.4/1.2 eV tandem (GaAs on top, GaInAs beneath) and a 1.2/1.0 eV tandem (AlGaInAs on top, GaInAs beneath). Both designs featured a gold back-surface reflector to reflect unused sub-bandgap photons back to the emitter, reducing heat losses and improving efficiency.

The cells were mounted on water-cooled copper microchannel heat sinks, with a heat-flux sensor sandwiched in between to directly measure the amount of absorbed heat. Under a 2,150 °C blackbody spectrum, each design reflected about 93% of the out-of-band radiation. As expected, efficiency increased with emitter temperature: the 1.4/1.2 eV cell reached a peak efficiency of 41.1 ± 1% and power output of 2.39 W/cm² at 2,400 °C, while the 1.2/1.0 eV cell peaked at an efficiency of 39.3 ± 1% and power output of 1.81 W/cm² at 2,127 °C.

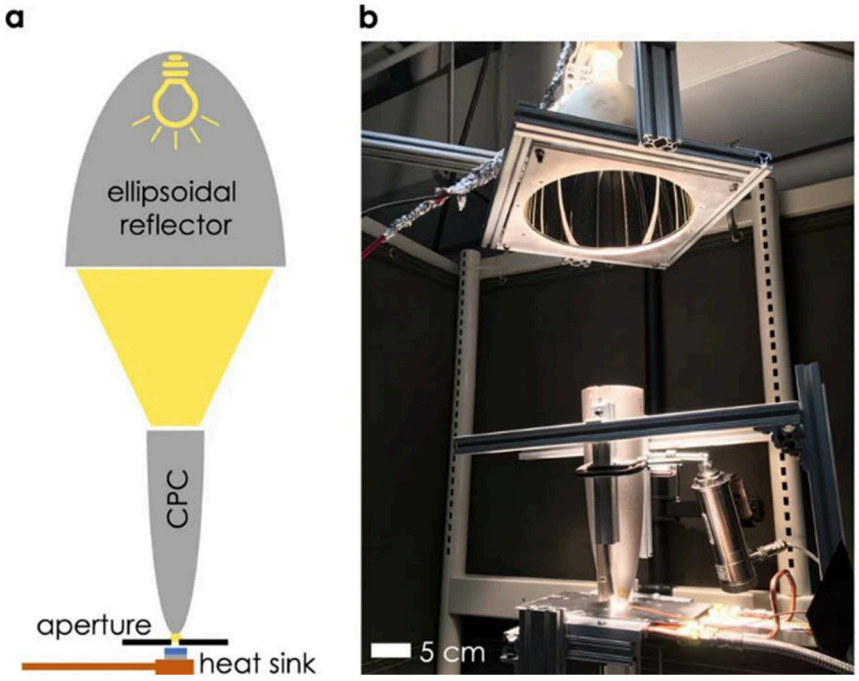


Figure 2-24 (a) Schematic, and (b) image of the concentrator setup [73]

Moreover, Li and Xuan [92] experimentally evaluated a hybrid solar thermophotovoltaic–thermoelectric (STPV–TE) system using a xenon-lamp-based solar simulator as the heat source. Light from a spherical xenon lamp was directed by a parabolic mirror, concentrated by a Fresnel lens, and further focused with a secondary prism concentrator onto a silicon carbide (SiC) absorber/emitter. The emitter was placed inside a reflective cavity to reduce thermal losses, with its temperature monitored by K-type thermocouples. Two Si/SiO_2 photonic crystal filters were used for spectral splitting. Filter 1, positioned before the emitter, reflected radiation with wavelengths ranging from 1,800 to 3,600 nm back to the emitter. Filter 2, situated in front of the thermoelectric (TE) modules, reflected wavelengths shorter than 1,800 nm toward a commercial GaSb TPV cell (Eg = 0.72 eV) and transmitted the rest to four Bi_2Te_3 TE modules. The TPV cell was mounted on a water-cooled plate, while the TE modules were thermally isolated. The entire assembly was housed in a vacuum chamber to minimize convection losses.

Experiments were performed over emitter temperatures from 800 to 1,100 °C, recording TPV and TE electrical outputs. In the hybrid configuration, the TPV cell's center temperature was reduced by 7.2 °C compared to the solo STPV system, while the TE modules operated up to 93.9 °C hotter than the TPV cell. At 1,100 °C, the hybrid system produced 636.8 mW from the TPV cell and 2.91 W from the TE modules, for a total of 3.55 W, which was over four times the output of the solo TPV system (0.86 W).

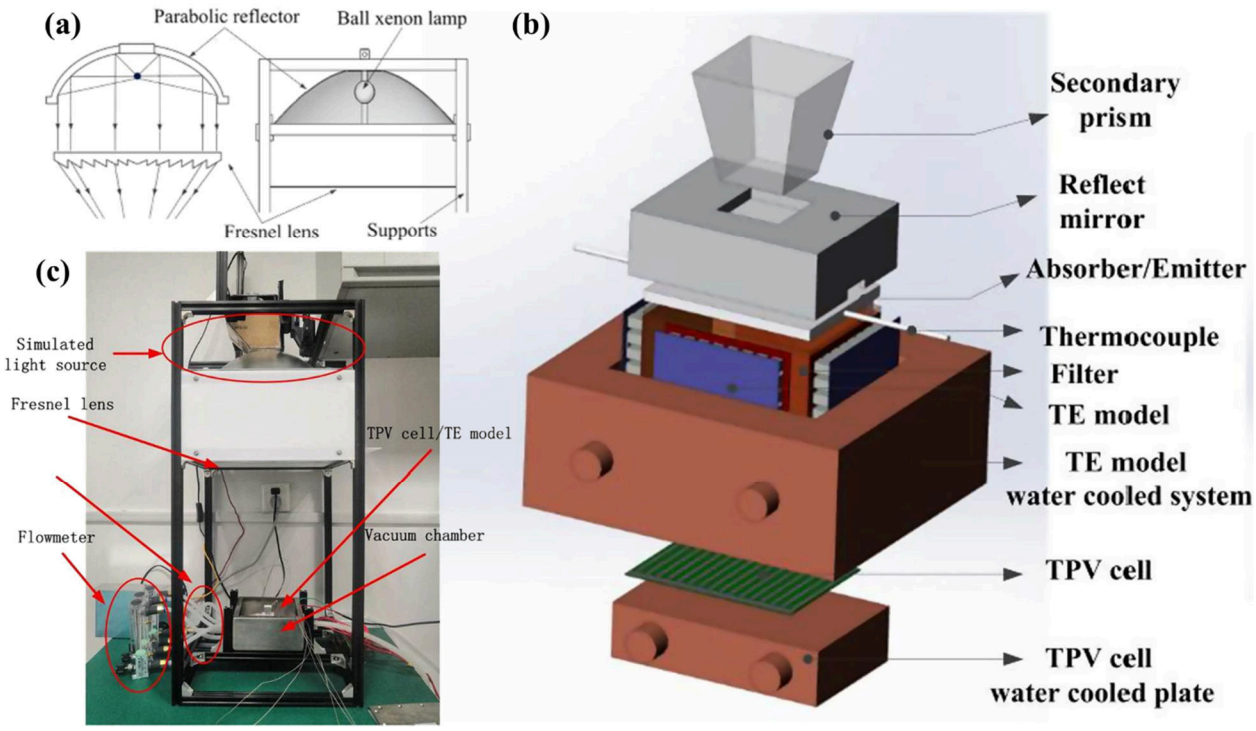


Figure 2-25 (a) sunlight simulator sketch, (b) STPV-TE 3D structure, and (c) diagram of STPV-TE system [92]

One of the advantages of reviewing previous articles was identifying a second heat source that not only provides high power but also powers the system through radiation. Based on this, a halogen lamp with a concentrator was selected for implementation in the setup.

2.5 Multisource Systems

This section reviews the literature on hybrid TPV systems that incorporate multisource heat power and discusses the fundamental operating conditions under which a multisource TPV system can function effectively.

2.5.1 Hybrid TPV System Background

Hussain et al. [93] explored the integration of TPV into hybrid solar–biomass power generation systems. They argued that TPV technology could effectively utilize surplus thermal energy produced during peak solar irradiance periods, thereby enhancing overall system efficiency and economic viability. Through a simulation-based study employing various semiconductor TPV cells, the research demonstrated significant potential for reducing biomass fuel consumption and increasing the solar fraction in concentrated solar power (CSP) plants. The study introduced three configurations: a stand-alone TPV system, a hybrid solar–biomass TPV system, and a TPV retrofit integrated into a central receiver tower of a hybrid power plant. One of the key findings was that integrating TPV systems at medium operating temperatures (around 1000 °C) could recover excess thermal energy that would otherwise be wasted, significantly improving power plant efficiency.

Additionally, the study mainly focused on medium-temperature operation, leaving opportunities for future exploration at a wider range of temperatures and through experimental validation.

Davis et al. [94], in a consultant report, detailed the development of a hybrid solar-natural gas TPV system aiming to enhance efficiency and energy density. The research involved building a modular, adjustable prototype to cater to diverse customer power needs. The innovative design incorporated solar apertures and advanced IR band-pass filters, along with a high-performance parabolic concentration system to significantly boost power density. The study reported that it achieved substantial improvements in overall efficiency, specifically 22.3% solar-to-electric and 15.6% gas-to-electric efficiencies.

However, the targeted high emitter temperatures (1600 °C) could not be attained due to material compatibility constraints, and vacuum sealing issues negatively impacted the system's overall operational potential, highlighting critical design and materials challenges. Further research could focus on resolving these material and design issues to fully exploit the potential efficiency gains and system performance.

Hussain et al. [95] focused on hybrid solar-biomass TPV systems specifically intended for regions with relatively low Direct Normal Irradiance (DNI) levels (below 1600 kWh/m²). The study proposed three geometric configurations: Dual TPV Cell Arrangement, Sliding TPV Cell Arrangement, and Heat Injected Emitter. Their analysis concluded that the "Heat Injected Emitter" configuration was optimal due to its simplicity, flexibility to operate in both solar and fuel modes, and ease of construction.

This configuration was identified as most suitable for achieving the desired temperature range (800°C-1800°C). However, the research was primarily theoretical, focusing on geometry-based analyses without experimental or comprehensive efficiency validation, representing a notable limitation. Future studies should include practical experimental validation to confirm theoretical predictions and to examine efficiency improvements in detail.

In their subsequent economic analysis, Hussain et al. [96] assessed the Levelized Cost of Electricity (LCOE) for hybrid solar-biomass TPV systems. The research emphasized that the economic viability of TPV systems heavily depends on significant reductions in TPV cell costs, achievable through increased production scales. They indicated that operating temperatures should ideally be below 800°C to maintain economical biomass consumption and achieve competitive LCOE compared to conventional CSP-biomass Rankine cycle plants.

The study evaluated various scenarios, highlighting that TPV cell production volume increases could significantly reduce costs, making TPV technology economically viable for broader deployment. Future research could further explore detailed cost breakdowns and evaluate the impacts of advanced manufacturing techniques on overall system economics.

Guazzoni and McAlonan [97] addressed the multifuel capabilities of TPV systems for military applications, specifically targeting diesel and other liquid hydrocarbons through advanced fuel atomization techniques. The study introduced a novel fuel atomization method where liquid fuel was atomized through compressed air, creating finer droplets and improving combustion efficiency. The system used selective emitter treatments and optical shielding to enhance performance, achieving efficiency improvements at higher emitter temperatures (1000 °C and 1300 °C).

While the findings indicated promising potential for portable, lightweight, and multifuel power generation, the absence of numerical analysis remains a significant limitation, emphasizing the need for further practical evaluation.

2.5.2 Fundamental Operating Principles of Multisource TPV Systems

To understand the operation of a multi-source TPV system, two main principles must be considered. First, the absorber–emitter temperature is primarily elevated by a dominant, high-power source, such as a fuel-based burner or a concentrated renewable input, that serves as the main heating element. Alongside this primary source, additional radiant heat sources (Heat Source 1 to n in Figure 2-26), such as solar irradiation or laser power beaming, can act as auxiliary contributors. For these auxiliary sources to enhance the emitter temperature, the net radiative heat flux they deliver must remain positive. In practical terms, this requires the source temperature (T_1 to T_n) to be higher than the emitter temperature ($T_{Emitter}$). A clear example can be found in solar radiation: although the Sun's surface temperature is around 5800 K, the concentrated sunlight directed onto the emitter can locally provide radiative fluxes that exceed the emitter's surface temperature, thereby transferring energy effectively and supporting the main heating process. If this condition is not satisfied, auxiliary sources may fail to add heat or, worse, draw energy away from the emitter, reducing the system's performance.

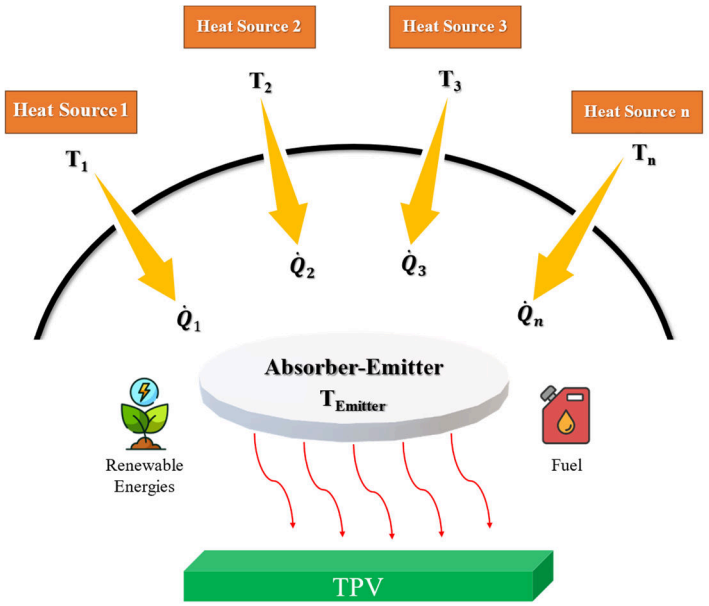


Figure 2-26 Schematic of a hypothetical multi-source TPV system

As illustrated in Figure 2-27, the radiative exchange between two surfaces, A and B, occurs simultaneously in both directions. The amount of radiation transferred from one surface to the other depends on the emissivity and absorptivity of each surface, as well as the geometric relationship defined by the view factors F_{AB} and F_{BA}, which are equal ($F_{A\to B} = F_{B\to A}$). According to Kirchhoff's law, for a given wavelength and temperature, a surface's spectral emissivity equals its spectral absorptivity ($\varepsilon = \alpha$). Therefore, the energy emitted by surface A and absorbed by surface B can be expressed in Equation *2.1*.

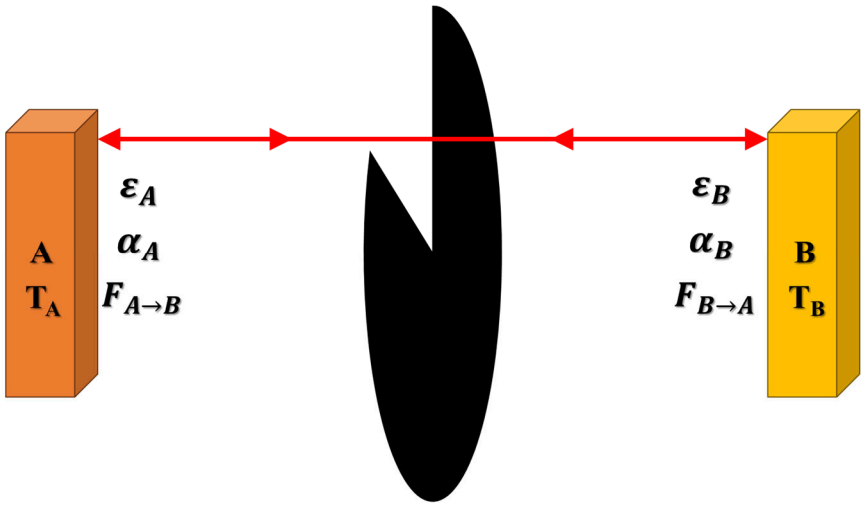


Figure 2-27 Radiative heat exchange between two surfaces A and B

$$E_{A\to B} \sim \varepsilon_A \cdot \alpha_B \cdot \sigma \cdot T_A^4$$
$$E_{B\to A} \sim \varepsilon_B \cdot \alpha_A \cdot \sigma \cdot T_B^4 \qquad 2.1$$

Since $\varepsilon_A = \alpha_A$ and $\varepsilon_B = \alpha_B$, the net radiative heat transfer between the two surfaces depends primarily on their temperatures.

In this context, the surface with a higher temperature emits more radiative energy, resulting in a net heat flow from the hotter surface to the cooler one. Consequently, for an auxiliary source to contribute positively to the emitter's heating, its effective temperature must be higher than that of the emitter. If the auxiliary source is cooler, the net heat flux reverses direction, and instead of increasing the emitter's temperature, it draws energy away, thereby reducing the overall performance of the system.

Second, while it might appear that a single heat source with total power equal to the sum of all sources could achieve the same emitter temperature, such reasoning overlooks real-world constraints. Factors such as the limited availability of carried fuel in space applications, the intermittency of solar irradiance, or fluctuations in renewable energy supply, make auxiliary inputs not only practical but often essential.

3 Chapter 3: Methods

3.1 Analytical

3.1.1 Simulated Thermal Performance of the Absorber–Emitter

As discussed in Section 2.2, The role of the emitter in a TPV system is to radiate photons that fall within the bandgap of the TPV cell when it is heated by a heat source. In this work the absorber–emitter is composed of a tungsten layer deposited on a AlN substrate and heated via Joule heating. To better understand the thermal behavior of the deposited tungsten layer on the substrate, a simulation was conducted using COMSOL Multiphysics. The main goal of the simulations is to determine the substrate's temperature at different input power levels during the Joule heating process. This simulation helps predict the temperature distribution and improves system performance.

COMSOL Multiphysics is a powerful simulation software used for modeling and analyzing physical systems. It provides a versatile platform for solving Multiphysics problems, including heat transfer, fluid dynamics, and electromagnetic analysis.

. The COMSOL simulations include an AlN substrate, with a tungsten layer deposited on top. By applying a voltage across two opposite sides ends of the tungsten layer, electric current flows through it, generating heat due to Joule heating. As the temperature of the emitter rises, thermal radiation occurs from all surfaces of the emitter simultaneously.

The AC/DC Module, Electromagnetic Heating, and Heating Circuit were utilized in the simulation. These modules are interconnected to model the joule heating process and predict the temperature distribution of the system. The governing equations linking these three modules are presented below.

3.1.1.1 Electrical Domain: Current Flow and Joule Heating

The electrical behavior of the tungsten emitter is governed by the charge conservation principle, expressed through the current continuity equation:

$$\nabla \cdot (\sigma \nabla V) = 0 \tag{3.1}$$

This equation ensures that the current entering any point in the conductor is equal to the current leaving it, in accordance with Kirchhoff's current law in differential form. In this expression, σ represents the electrical conductivity of tungsten (S/m), and V is the electric potential (V). Electric field $\boldsymbol{E}$ is then defined as the negative gradient of the electric potential:

$$\boldsymbol{E} = -\nabla V \tag{3.2}$$

This relationship describes how the electric field varies spatially within the conductor due to potential differences. The resulting current density J, representing the movement of charge carriers follows Ohm's Law and is defined as:

$$J = -\sigma \nabla V \tag{3.3}$$

The generation of heat due to the flow of current known as Joule heating is calculated through the following expression:

$$Q_e = J.E = \sigma \nabla |V|^2 \tag{3.4}$$

Here, Q_e is the volumetric rate of heat generation (W/m³) within the tungsten layer. This heat source term couples the electrical domain to the thermal domain and serves as the basis for predicting temperature rise in the system under electrical excitation.

3.1.1.2 Thermal Domain: Heat Transfer in Vacuum

The thermal response of the emitter is modeled using the transient heat conduction equation, which accounts for both heat diffusion and internal heat generation:

$$\rho_m C_p \frac{\partial T}{\partial t} = \nabla.(k \nabla \mathrm{T}) + Q_e \tag{3.5}$$

In this equation, ρ_m denotes the density of the material (kg/m³), c_p is the specific heat capacity (J/kg·K), and T represents temperature (K). The term k is the thermal conductivity of the material (W/m·K),

and Q_e is the heat source due to Joule heating, as described in the electrical domain. This equation enables the simulation to capture how heat propagates through the emitter material in both space and time.

As the emitter operates in a vacuum environment, heat loss occurs predominantly through thermal radiation rather than convection. This boundary condition is defined by the Stefan–Boltzmann law:

$$\mathbf{n} \,.\, (k\nabla T) = \varepsilon\sigma_{SB}(T^4 - {T_{ambient}}^4) \qquad 3.6$$

Here, $\mathbf{n} \,.\, (k\nabla T)$ represents the heat flux normal to the surface, ε is the emissivity of tungsten, and σ_{SB} is the Stefan–Boltzmann constant (5.67×10^{-8} W/m^{2}K^4). The term $T_{ambient}$ denotes the ambient temperature, such as the surrounding vacuum chamber walls. This condition allows the simulation to account for radiative heat losses from the emitter surfaces, ensuring a comprehensive thermal analysis under realistic operating conditions.

3.1.1.3 Material Properties

To achieve more accurate simulation results, the material properties including conductivity and resistivity, specific heat capacity, thermal conductivity, and emissivity used in the model are temperature-dependent and have been extracted from academic sources [98], [99], [100]. Initially, the temperature-dependent electrical resistivity and conductivity of tungsten were considered.

Resistivity (ρ) is measured in ohmmeters (Ω·m) and represents the resistance per unit length and cross-sectional area of a material. For instance, a material with a resistivity of 1 Ω·m exhibits a resistance of 1 ohm per meter in a cross-sectional area of 1 square meter. Conductivity (σ), on the other hand, is measured in Siemens per meter (S/m), where one Siemens (S) is the reciprocal of an ohm. This parameter indicates how easily a material conducts electricity. A material with a conductivity of 1 S/m allows a current of 1 ampere to pass through a 1-meter length with a 1-square-meter cross-section under a 1-volt potential difference. The relationship between these two quantities is expressed as follows:

$$\sigma = 1/\rho \qquad 3.7$$

The resistivity and conductivity of tungsten are plotted as a function of temperature in Figure 3-1. These visual representations provide insight into how tungsten's ability to conduct electricity changes with increasing temperature. As temperature rises, resistivity increases due to enhanced electron-phonon interactions, while conductivity decreases correspondingly [98].

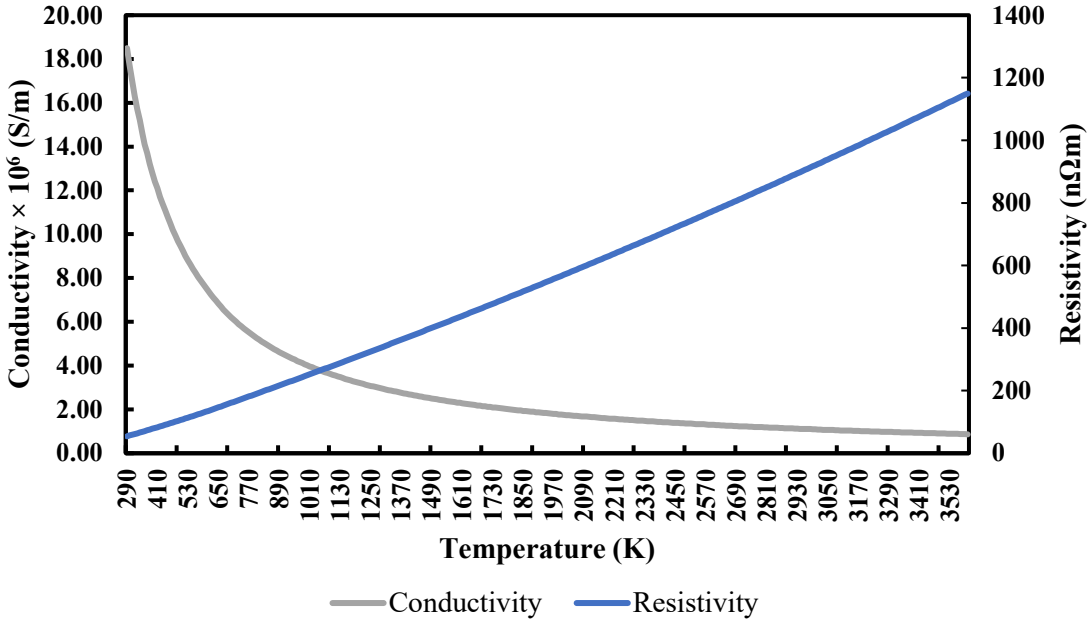


Figure 3-1 Tungsten electrical resistivity and conductivity based on temperature

Moreover, the relationship between the specific heat capacity and temperature of tungsten within the range of 273 to 3300 K is given by Equation (*3.8*) and the thermal conductivity of tungsten as a function of temperature is represented by Equation (*3.9*) [101].

$$C_P = 135.76 + (9.1159 \times 10^{-3})T + (2.3134 \times 10^{-9})T^3 - (6.5233 \times 10^5)T^{-2}\ (J/Kg.K) \quad 3.8$$

$$k = 108.34 - 1.052 \times 10^{-2}T + 23419.9/T\ (W/m.k) \quad 3.9$$

Furthermore, the total emissivity of tungsten as a function of temperature is shown in Figure 3-2 [98].

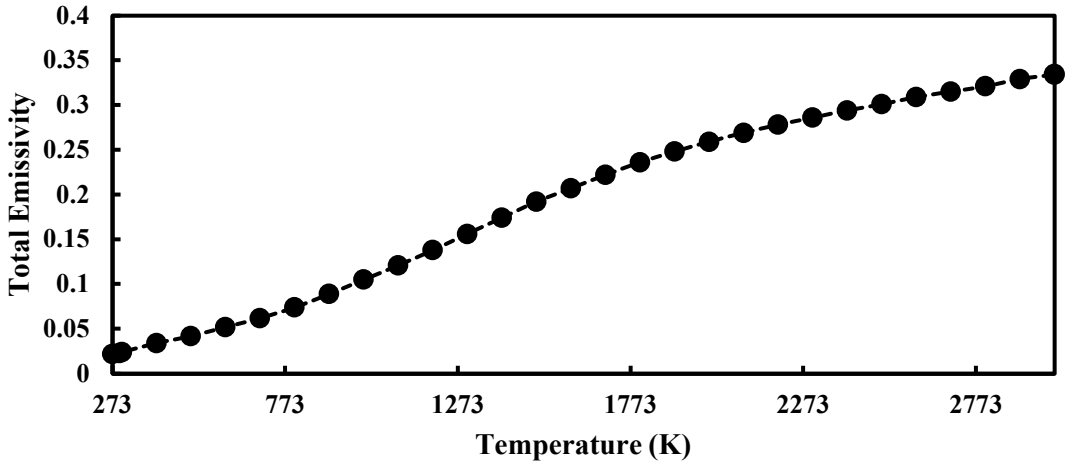


Figure 3-2 Total emissivity of tungsten based on temperature

Furthermore, as shown in Figure 3-3, the specific heat capacity and thermal conductivity of AlN vary as a function of temperature[99].

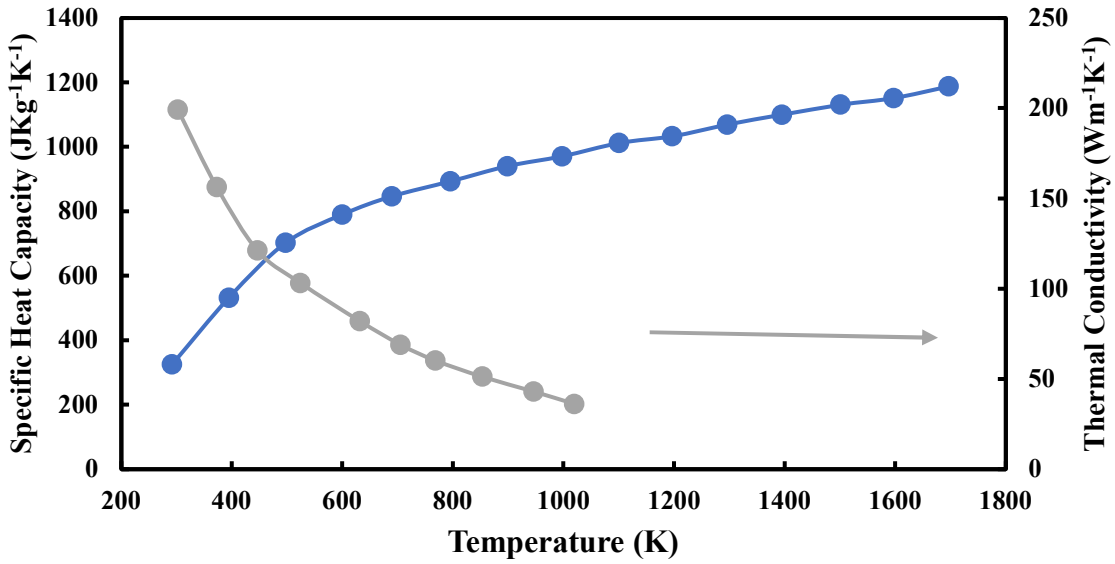


Figure 3-3 Specific heat capacity and thermal conductivity of AlN

Moreover, the emissivity relative to temperature, which has a great effect on the surface temperature in vacuum conditions, is plotted in Figure 3-4 [100].

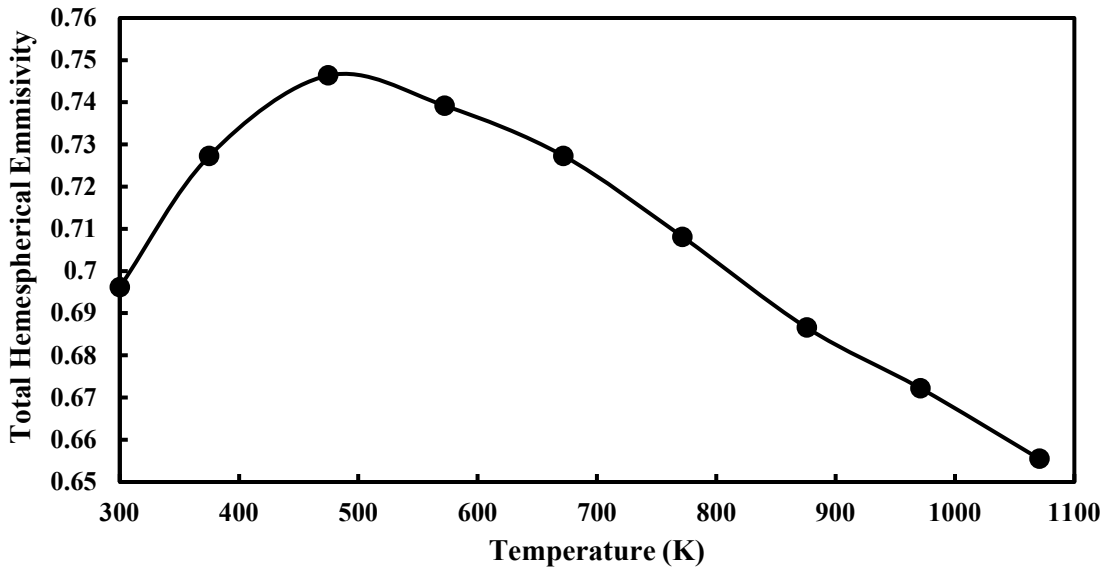


Figure 3-4 Total hemispherical emissivity of AlN relative to temperature

3.1.1.4 Mesh Independence and Convergence

To check the reliability of simulations, different mesh sizes were tested, and it was found that after a point, refining the mesh didn't significantly change the results, with no noticeable difference in key values like temperature and heat. Since the geometry of my model was quite simple and small, a coarse mesh with 172 mesh elements produced accurate outcomes. In the end, a coarse mesh that was both efficient and fast was selected.

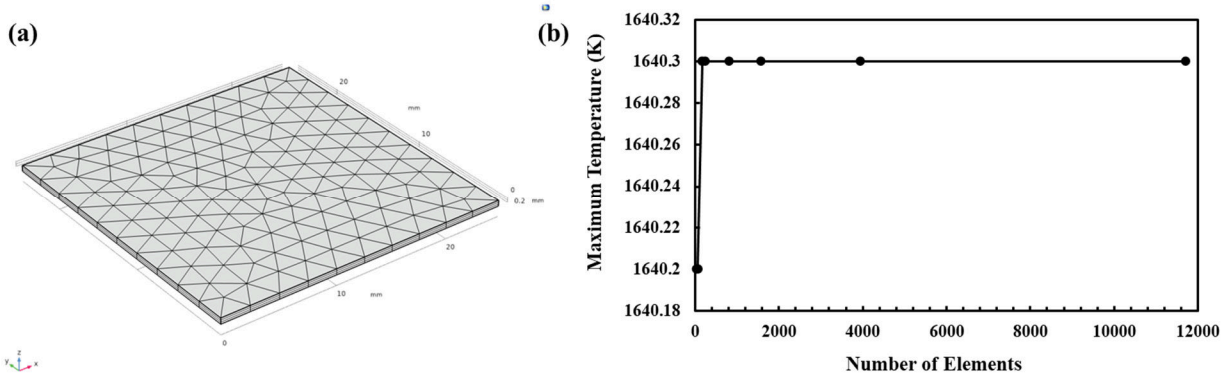


Figure 3-5 (a) Meshed geometry of the absorber–emitter (b) maximum temperature variation with mesh elements

To ensure numerical stability, a convergence study was performed alongside mesh validation. Solver tolerances (0.001) were carefully set, and the simulation was considered converged when residuals for key fields, voltage, current, and temperature, dropped below set thresholds and stabilized output values. This confirmed the results were reliable and not due to solver error.

3.1.1.5 Boundary Condition and Study

The initial conditions for the simulation are set with a temperature of 293.15 K, and the voltage within the layered shell is initialized at 0. By holding one edge of the tungsten layer as the grounded section and applying a sweeping method, the voltage is raised from 2 V to 10 V in 1-volt increments, and the thickness is increased from 50 nm to 1000 nm in 50-nanometer steps.

3.1.2 Numerical Analysis of the Thermophotovoltaic System

3.1.2.1 Numerical Evaluation of In-Band Photon Radiation

In the initial stages of the analytical analysis of the TPV system, a quantitative comparison of the amount of in-band photons for different kinds of TPV cells is carried out. Three types of TPV cells, namely Si, GaSb, and InGaAs, with bandgaps of 1.1 eV [102], 0.72 eV, and 0.6 eV [103], respectively, are considered. The first thing to determine is the spectral span, that is, the range of wavelengths that the TPV cell can absorb and convert into electrical energy. The bandgap energy of the TPV cell material determines the spectral range of photons that can generate current. The corresponding wavelength value is given by [104]:

$$E_g(eV) = \frac{1.24}{\lambda_{bg}(\mu m)} \rightarrow \lambda_{bg} = \frac{hc}{E_g} \tag{3.10}$$

Next, the TPV cell is powered with two 5 W/cm^2 heat sources, under separate and simultaneous conditions. To find the input temperature of the emitter, the Stefan–Boltzmann law (Equation *3.11*), which evaluates the total emissive power radiated from a blackbody, is used:

$$E = \sigma_{SB}\, T^4 \ (W/m^2) \tag{3.11}$$

Where σ_{SB} is the Stefan–Boltzmann constant ($5.67 \times 10^{-8}\ W/m^2 \cdot K^4$) and T is the temperature in Kelvin. For calculating emissive power of each specific wavelength, Plank's law of blackbody radiation (E_b) stated in Equation *3.12* is exploited:

$$E_b(\lambda, T) = \frac{2\pi hc^2}{\lambda^5} \times \frac{1}{e^{\frac{hc}{\lambda k_B T_{em}}} - 1} \ (W/m^2 \cdot m) \tag{3.12}$$

Which c is the speed of light in a vacuum ($3 \times 10^8\ m/s$), λ is the wavelength of the emitted radiation, h is Planck's constant ($6.626 \times 10^{-34}\ J.s$), k_B is the Boltzmann constant ($1.38 \times 10^{-23}\ J/K$) , and T_{em} is the temperature of the thermal emitter in Kelvin (K).

Finally, by integrating the in-band spectral emissive power over the span of bandgap wavelength (Equation *3.13*) the overall output power from the TPV cell was calculated.

$$\int_0^{\lambda_{bg}} E_b(\lambda, T)\, d\lambda \tag{3.13}$$

3.1.2.2 Analytical Comparison of Single-Source and Multi-Source TPV System

In this section, the theoretical framework and equations for determining the output power from the TPV systems are presented. To determine the electrical output generated by the TPV cell, both the current and voltage must be evaluated. The relation between the current density J and output voltage V of a TPV cell is given by Equation *3.14*:

$$J = J_{sc} - J_0\left(e^{\frac{qV}{k_B T_{cell}}} - 1\right) \ (A/m^2) \tag{3.14}$$

Two main sections of this relation are the J_{sc} represented by Equation *3.15*, and J_0 which represents the recombination losses in the TPV cell, i.e., the leakage current when there is no illumination, as stated in Equation *3.16* [105]:

$$J_{sc} = q \cdot \int_0^{\lambda_{bg}} \frac{q_i(\lambda) EQE(\lambda)}{hc/\lambda} d\lambda \ (A/m^2) \tag{3.15}$$

$$J_0 = 2.555 \times 10^{-4} \cdot T_{cell}^3 \cdot e^{\frac{-E_g}{k_B T_{cell}}} \ (A/m^2) \tag{3.16}$$

Where q is the quantity of the electricity of electron ($1.602 \times 10^{-19}\ C$), T_{cell} is the temperature of TPV cell in Kelvin, EQE is the external quantum efficiency, and q_i is the net spectral radiant heat flux of the cell can be obtained from Equation *3.17*:

$$q_i(\lambda) = VF \cdot \varepsilon(\lambda, T) \cdot E_b(\lambda, T) \ (W/m^2 \cdot m) \tag{3.17}$$

Which represents the radiation energy incident onto the cell surface. Here, VF denotes the view factor between the emitter and the TPV cell, ε is the emittance of the emitter surface, specifically the AlN ceramic sheet used in this setup, and E_b refers to the blackbody radiation spectrum, as described in Equation *3.12*. Finally, by sweeping the voltage in Equation *3.14* and identifying the point where the product of current density and voltage is maximized, the corresponding output power can be calculated:

$$P_{mp} = J_{mp}V_{mp} \ (W/m^2) \tag{3.18}$$

As stated in Equation *3.15* the external quantum efficiency (EQE) is essential for calculating the J_{SC}. EQE quantifies the overall efficiency of converting incident photons into collected charge carriers. It accounts for both the absorption of photons and the subsequent collection of generated carriers. Illustrated in Equation *3.19*, EQE is defined as the ratio of the number of charge carriers collected by a photovoltaic cell to the number of incidents photons hitting incident onto its surface [106].

$$EQE = \frac{Electrons/sec}{Incident\ photons/sec} \tag{3.19}$$

Here, the EQE values are taken from the datasheet provided by the TPV cell manufacturer and are illustrated in Figure 3-15.

Moreover, the VF is required to evaluate the heat flux, as indicated in Equation *3.16*. VF represents the fraction of radiation emitted from the emitter that reaches the TPV cell surface. Due to the geometric complexity of the setup and the lack of a direct analytical formula for calculating VF, a simulation approach was adopted. Using the Surface-to-Surface Radiation physics module in COMSOL Multiphysics (Figure 3-6), the simulation was carried out with the actual geometrical parameters and material properties of the experimental setup. The VF was then extracted from the computed radiation exchange results.

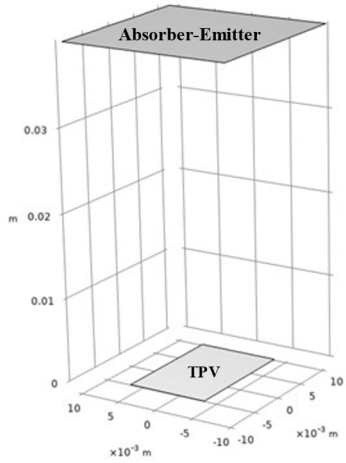


Figure 3-6 Numerical evaluation of VF using COMSOL simulation

Furthermore, another parameter which is important for determining the output power of TPV systems is the ratio of the actual output power to the multiplication of I_{SC} and V_{OC} is known as the FF, and it is represented by the following equation:

$$FF = \frac{I_{mp}V_{mp}}{I_{SC}V_{OC}} \tag{3.20}$$

For modeling the multi-source TPV system and demonstrating its advantages over a single-source configuration, two heat sources were considered, each varying in temperature from 500 K to 1270 K. Initially, the output power of the TPV cell was calculated separately for each source using the governing equations presented earlier. These individual contributions were then added to represent the total output in the single-source mode. Subsequently, the same two sources were used simultaneously to power the system, and the output power under this combined operation was calculated. Finally, an enhancement plot was generated to illustrate the improvement in output power, showing the ratio of the simultaneous dual-source mode to the combined output of the separate source mode at identical input conditions.

3.2 Experimental

3.2.1 External Instrumentation and Support Systems

The experimental setup, illustrated in Figure 3-7, is described in this section.

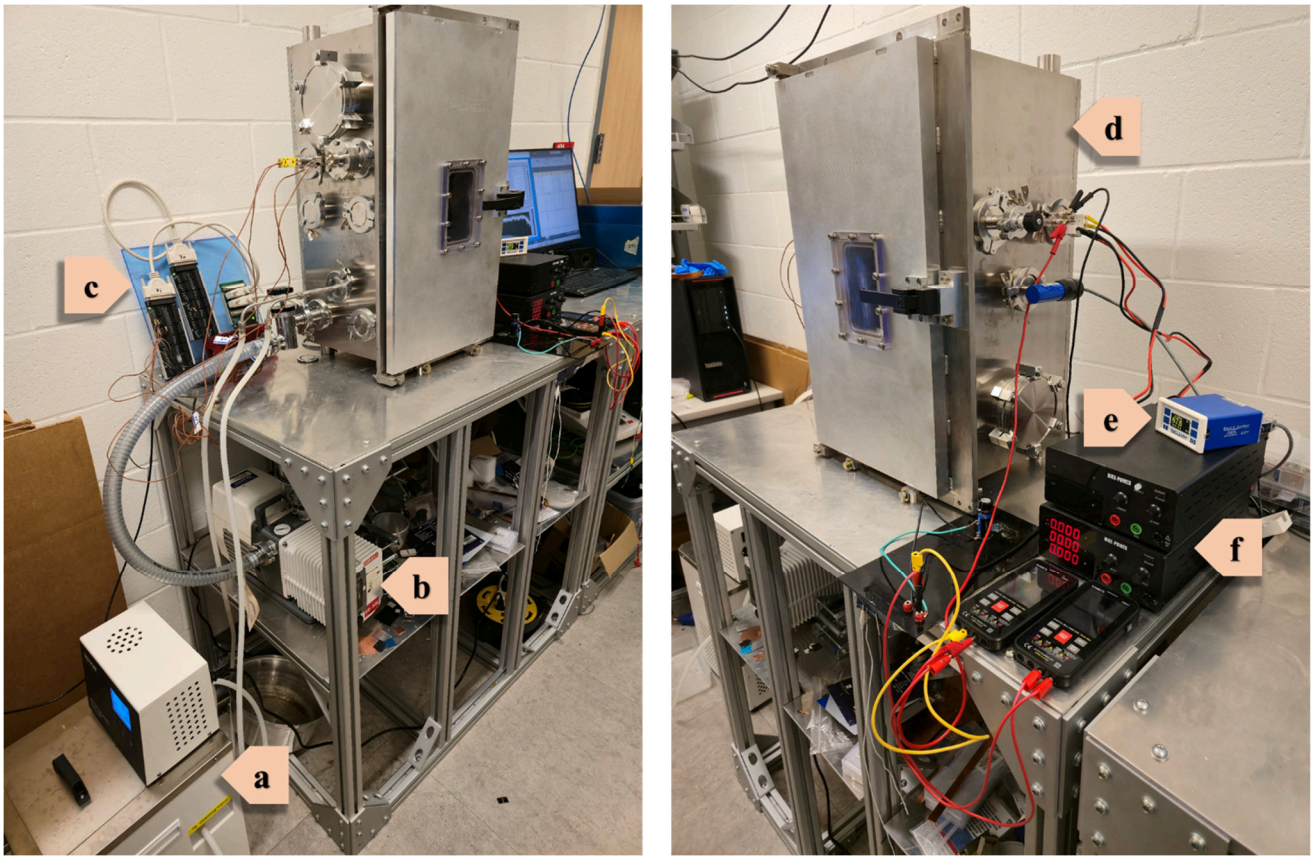


Figure 3-7 External instrumentation comprises (a) chiller, (b) vacuum pump, (c) LabJack T7 data acquisition system, (d) vacuum chamber, (e) benchtop gauge controller and (f) power supply

3.2.1.1 Vacuum Pump, Chamber, and Gauge Controller

The TPV testing apparatus consists of a vacuum chamber, purchased from Kurt J. Lesker, with dimensions of 30.5 cm by 30.5 cm with a height of 61 cm (Figure 3-7d). The chamber is equipped with ports and feedthroughs to accommodate thermocouples and power connections. To achieve the required vacuum conditions, a Varian SD-301 pump (Figure 3-7b) is used, which has an ultimate pressure of 1.5×10^{-3}

Torr [107]. The vacuum level was monitored using the KJLC 375 benchtop gauge controller (Figure 3-7e), which is capable of measuring pressures ranging from 10^{-4} to 1000 Torr [108].

3.2.1.2 Data Acquisition & Power System

To record the temperature of the TPV system components during the experiments, a LabJack T7 data acquisition system (Figure 3-7c) was utilized. The LabJack T7 is a multifunctional analog and digital I/O device capable of high-precision voltage measurement and sensor interfacing. It features multiple input channels and supports various sensor types, making it a suitable choice for temperature monitoring in experimental setups.

For temperature sensing, K-type thermocouples were employed due to their reliability, wide temperature range, and compatibility with the LabJack T7. A thermocouple is a temperature sensor consisting of two dissimilar metal wires joined at one end, forming a junction where the temperature is measured. The K-type thermocouple specifically consists of Chromel (Ni-Cr) and Alumel (Ni-Al) alloys. It is one of the most widely used thermocouple types, offering a broad operating range from approximately −200 °C to +1260 °C, good sensitivity (~41 μV/°C), and robust performance in various environments. All thermocouples were calibrated using ice, room temperature, and boiling water as reference points to increase the measurement accuracy.

Two NICE-POWER variable DC bench power supplies (30V, 30A, 900W) (Figure 3-7f) were used to provide power to both heat sources in the setup: the emitter and the lamp. These units offer high-resolution output control, with voltage adjustable to 0.01 V and current to 0.001 A. They are designed for low-noise, low-ripple operation and can deliver continuous power at full load. Furthermore, two multimeters are employed to function as an ammeter and a voltmeter to measure the electrical power generated by the TPV cell.

3.2.1.3 Chiller

The laboratory chiller, model DC-0506, from VEVOR (Figure 3-7a) [109] is designed to deliver efficient and reliable cooling for long-term operations. It features a high-quality, fully enclosed compressor and a quiet, low-noise circulation water pump, ensuring fast cooling speeds and strong temperature stability. The chiller is equipped with a compact structure that allows for seamless integration into lab environments. With a power rating of 1000 W, it offers a temperature range from -5 °C to 100 °C, with an impressive temperature adjustment accuracy of 0.01 °C. The chiller's water tank has a capacity of over 5L, and the tank's size is 18 x 16 x 15 cm. The countertop water tank is made from durable 304 stainless steel, providing durability and resistance to corrosion. During testing, the chiller was set to -5 °C, and ethanol was chosen as the cooling fluid, due to its low freezing point of approximately −115 °C [110] to ensure reliable operation without risk of ice formation.

3.2.2 Internal Chamber Assembly and Experimental Setup

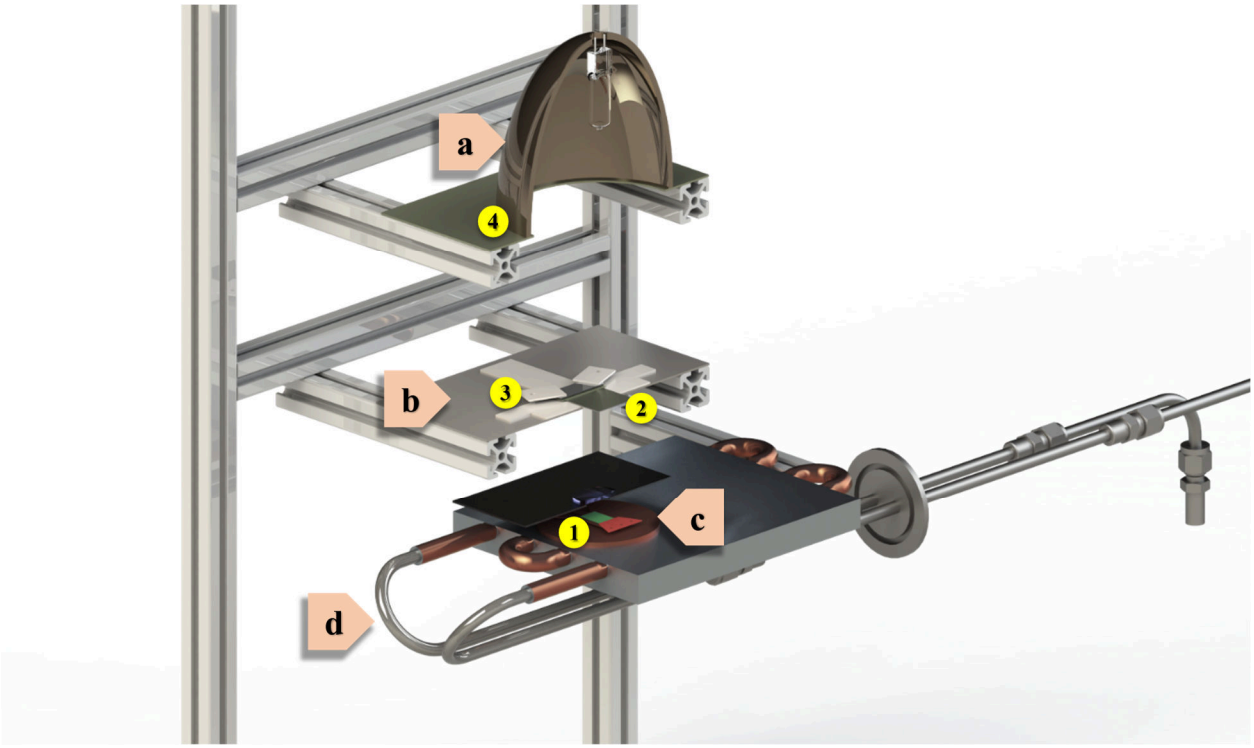


Figure 3-8 Internal chamber assembly comprising (a) light source, (b) emitter segment, (c) TPV circuit assembly, and (d) cooling system

Inside the vacuum chamber, the main experimental components are arranged along a common centerline to maximize optical and thermal coupling (Figure 3-8). These include: (a) the light source, (b) the emitter segment, (c) the TPV circuit, and (d) the cooling section. Aligning all segments coaxially ensures the convergence of light onto the emitter and a high VF from the emitter to the TPV cell, thereby optimizing power output.

To support and organize all components within the vacuum chamber, an aluminum extrusion frame was used as the inner structure. The extrusions have a cross-section of 20 × 20 mm and are assembled using corner brackets. This frame serves to maintain the alignment of both the first and second sources while also providing structural support for the cooling section.

Thermocouples, indicated by labels (1–4) in Figure 3-8, are placed throughout the assembly to monitor temperatures at critical locations and record thermal performance during operation.

3.2.2.1 Light source

For wireless powering of the system, a high-power light source is required to raise the emitter temperature and emit photons onto the TPV cell. Accordingly, a 150 W, 24 V halogen bulb is employed. To concentrate its output, the bulb is placed at the focal point of an aluminum cavity in the form of half an ellipsoid: the polished walls reflect and focus the light onto the second focal point, which is aligned with the emitter. To secure the bulb at the cavity's entrance, fractal paste [111] is applied to fill the gap, and the bulb's contacts are pressed into the paste. This method helps keep the bulb steady inside the cavity and ready for electrical connection. Finally, the entire light assembly is mounted on a tungsten sheet with a central circular cutout, which supports the half-elliptical reflector directly above the emitter segment. Figure 3-8a shows the whole configuration of the light source.

3.2.2.2 Emitter Segment

The tungsten sputtering target (Figure 3-9) used in the substrate deposition has a 3-inch diameter and is 0.250-inch thick. It has a purity of 99.95%, is not bonded, and was supplied by the *Angstrom Engineering* company.

Tungsten, also referred to as Wolfram, is among the densest elements, with a density of 19.3 g/cm^3 and an exceptionally high melting point of 3,410 °C. It exhibits a grayish-white, lustrous appearance and possesses remarkable hardness, making it challenging to machine or forge in its pure form. Tungsten also has a low vapor pressure of 10^{-4} Torr at 2,757 °C, contributing to its stability at high temperatures. Due to its unique physical and thermal properties, tungsten is widely utilized in various applications, including electric filament production, cutting tools such as drills and saws, and high-durability jewelry. Additionally, tungsten is employed in vacuum evaporation processes for manufacturing semiconductors, fuel cells, and sensors, where its high-temperature resistance and conductivity are advantageous [112].



Figure 3-9 Tungsten sputtering target [112]

The Tungsten target should be placed in the DC sputtering gun, and based on inquiry from Angstrom technicians, the input power should be 88 W/in^2. Considering the diameter of the tungsten target, the required sputtering power was determined using Equation *3.21*.

$$88\ W/in^2 \times 1.5^2\pi \approx 600\ W \tag{3.21}$$

Since the available equipment only accepts the target output power percentage, and not the power itself, the input power must be entered relative to the maximum output power of the sputter system, which is 1000 W. Therefore, the maximum target output limit will not be more than 60%.

For the deposition process, the AMOD PVD platform was used (Figure 3-10). It possesses a 500 mm by 500 mm baseplate, supports various PVD techniques, and can accommodate up to 6 sources [113].



Figure 3-10 AMOD PVD platform

After cutting the AlN ceramic sheets into square pieces with dimensions of 2 and 2.5 cm, they were cleaned using acetone, ethanol and deionized water to remove surface contaminants. After chemical cleaning, the substrates were carefully air-blown to ensure evaporation of the solvents while avoiding any physical contact with the surface. This method was chosen to preserve the original surface smoothness and prevent unintentional roughening, which could affect the quality of subsequent thin-film deposition.

The cleaned AlN substrates were mounted to the platen with Kapton tape (Figure 3-11) and loaded into the sputter chamber. The chamber was pumped down to 2^{-6} Torr, and the preheating process was then initiated. The platen was heated to 200 °C with the ramp rate set to 80 °C/min. The flow rate of the Argon gas inside the chamber is 18 SCCM. For better results and fine cohesion, the sputtering is performed as shown in Figure 3-12, in separate steps, beginning with a preconditioning phase followed by two deposition phases. The output power during the preconditioning phase is set to 10% of the maximum output power and a ramp rate of 5 W/min. Completing preconditioning phase, the first section, to have better cohesion, the power was set to 25% of the rated power, and the deposition rate was at 1.8 Å/s. After 1000 Å deposition,

the second phase of sputtering began, and the input power percentage for this stage was on the safe side and was 40% of the maximum power output, which increased the deposition rate to 3 Å/s. In this phase, the thickness target was 9000 Å, and in total, the final thickness of the deposited tungsten film was 1µm. Finally, the samples were subjected to a flow of nitrogen gas, and the chamber was vented after the samples reached room temperature.

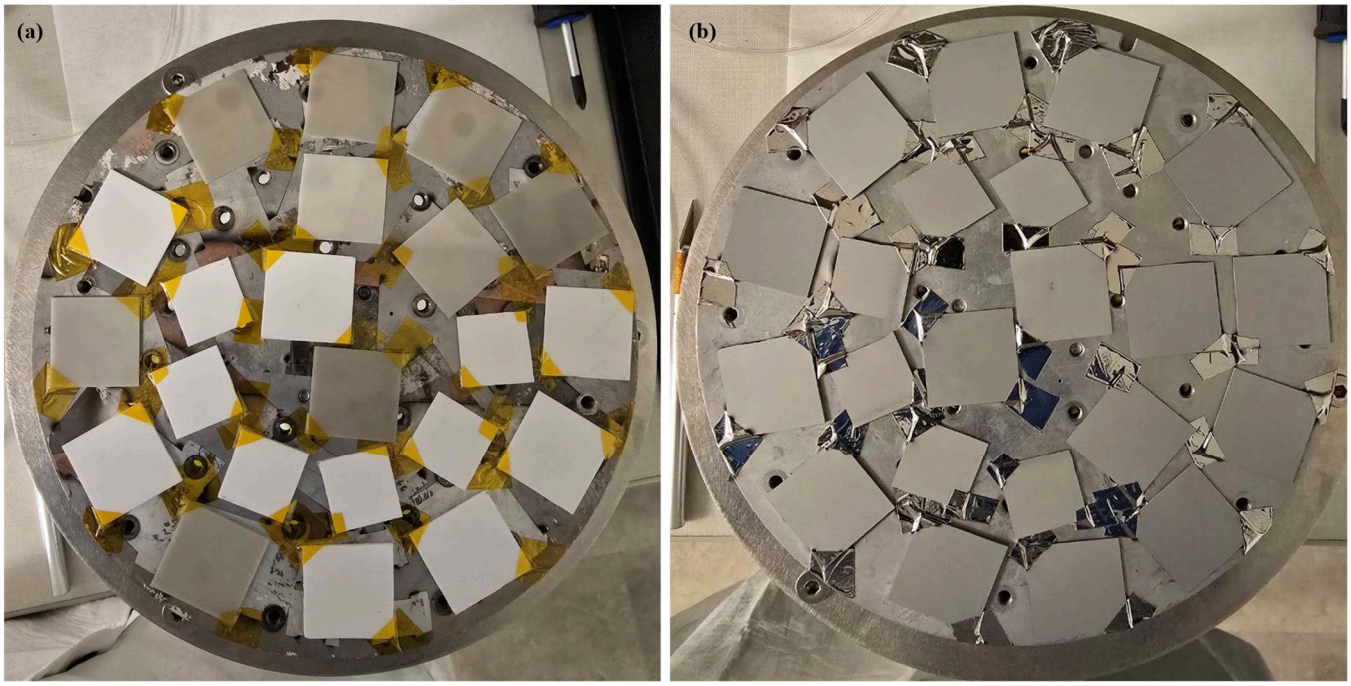


Figure 3-11 AlN substrates (a) before and (b) after depositing tungsten onto their surface

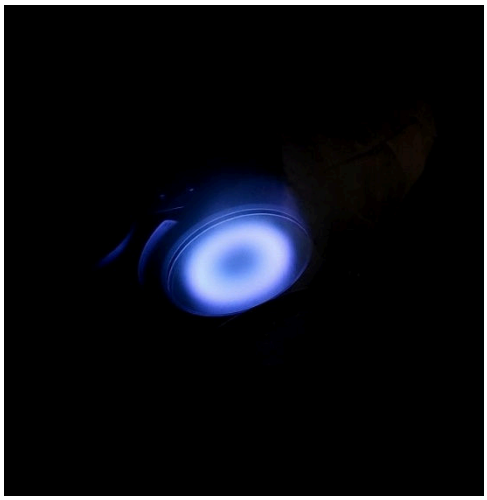


Figure 3-12 Tungsten target during sputtering

To analyze the spectral behavior of the absorber-emitter, the most suitable method was to determine its spectral emittance and reflectance. Accordingly, the Shimadzu UV-2600 Ultraviolet-visible (UV-Vis) spectrophotometer, equipped with an integrating sphere attachment, was used to measure the reflectance of the substrate in the 220 to 850 nm range. For the 952 to 2500 nm range, a Vertex 70 Fourier Transform Infrared (FTIR) spectrometer, also equipped with an integrating sphere, was employed. In both cases, the absorber-emitter was placed in a two-sided view configuration, allowing measurements from both the tungsten and AlN surfaces. Both instruments operate by sending a beam, based on their respective spectral capabilities, onto the substrate, and the reflected signal is then recorded to determine the material's spectral reflectance.

To calculate the emittance of the substrate, the following relation is used:

$$Emittance + Reflectance + Transmittance = 1 \qquad 3.22$$

Since the substrate is completely opaque, the transmittance is 0 and the emittance is found from the reflectance and Equation *3.22*. The data obtained from spectrometry is demonstrated as follows in Figure

3-13. The side with Aluminum Nitride is referred to as AlN(W) and the side with tungsten is denoted as W(AlN).

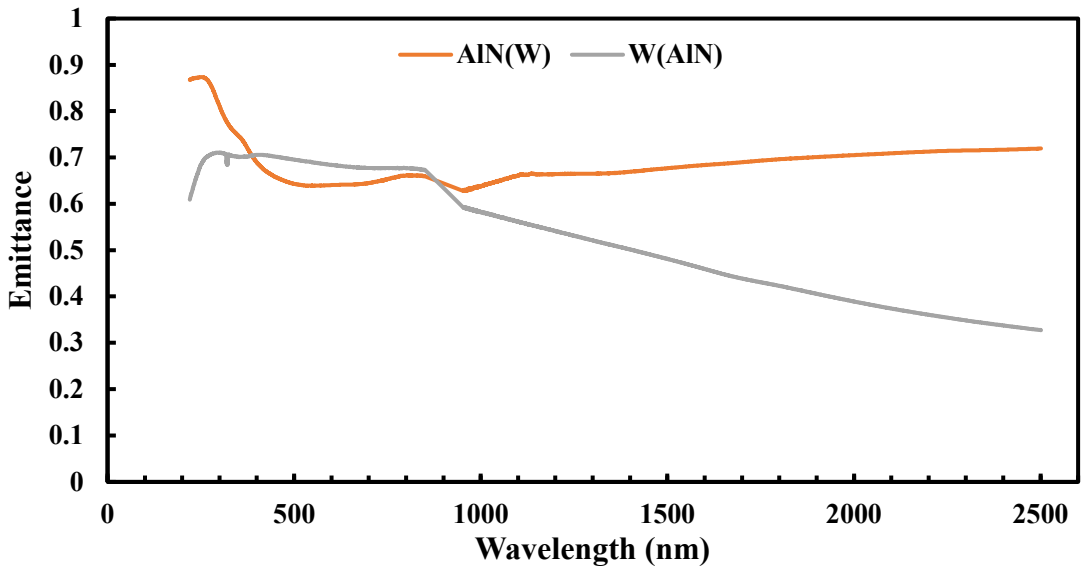


Figure 3-13 Spectral hemispherical emittance of the absorber-emitter

To power the custom absorber–emitter efficiently, a holder comprising multiple layers of materials that minimized heat losses while ensuring electrical isolation from the support was designed. A sheet of 304 stainless steel (Figure 3-14a) was used as the bottom layer. The relatively low thermal conductivity of the steel plate helped retain Joule heat within the emitter, while the high stiffness of the plate provides for a stable base. Additionally, its high melting point (approximately 1455°C [114]) ensures the support does not deform under intense heating, preserving alignment and structural integrity. The stainless-steel layer also features a 21 mm × 21 mm square cut-out centered directly beneath the emitter, whose dimensions are 25 mm × 25 mm, allowing heat and radiation to pass unobstructed to the TPV cell.

A 1 mm thick Al_2O_3 ceramic sheet is placed on top of the steel plate (Figure 3-14b). This ceramic functions as an electrical insulator, preventing current from leaking into the steel, and it also adds extra thermal resistance, which reduces the amount of heat the emitter losses to its surroundings. The

tungsten-coated emitter then sits directly on this ceramic, with its sputtered side facing upwards (Figure 3-14c).

To feed power into the emitter evenly, two small (3 cm × 1 cm) tungsten strips (Figure 3-14d) were placed across part of the tungsten emitter's surface near opposite edges. High-temperature, high-current wires (12 AWG silicone, rated -60 °C to +200 °C, 600 V/30 A) were attached to these tungsten strips. The wires sit right on the tungsten contacts, and to secure electrical and thermal insulation, they were held in place using matching 3 cm × 1 cm AlN ceramic blocks (Figure 3-14e).

Finally, four small Al_2O_3 ceramic blocks (Figure 3-14f), each with pre-formed screw holes, were used to clamp the entire assembly together while maintaining electrical isolation. The result is a compact, reliable assembly that confines the heat to the emitter and prevents stray currents from traveling into the rest of the setup. Figure 3-14 shows an expanded view of this assembly, highlighting each layer and connection.

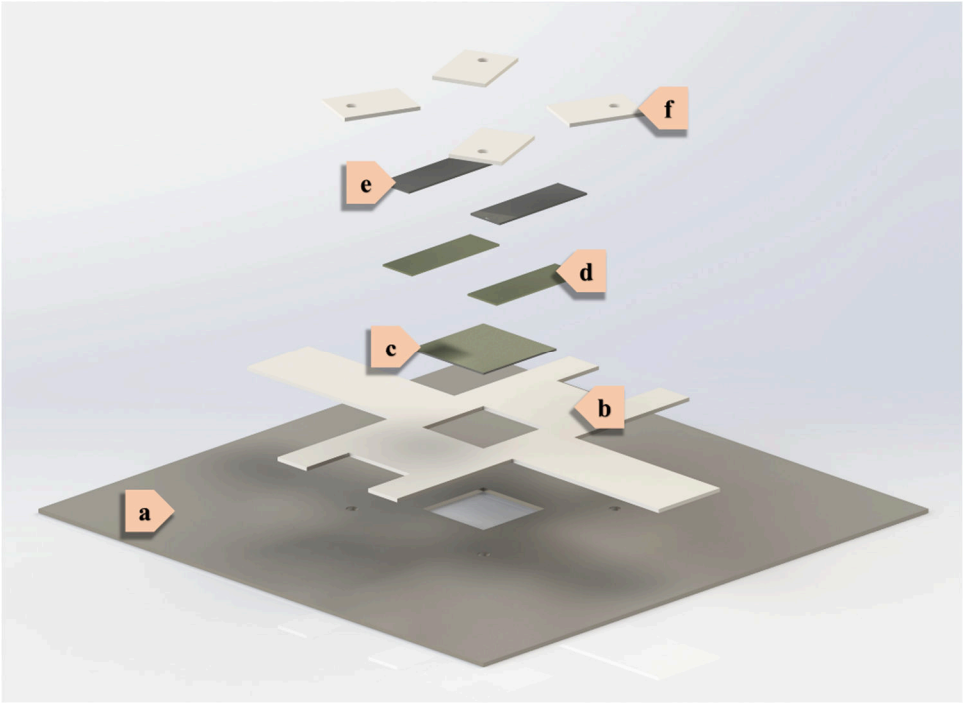


Figure 3-14 Expanded view of the assembled emitter segment, showing (a) the 304-grade stainless steel base, (b) Al_2O_3 insulation layer, (c) tungsten-coated emitter, (d) tungsten contact strips, (e) AlN ceramic blocks, and (f) Al_2O_3 ceramic blocks with pre-formed screw holes.

3.2.2.3 Thermophotovoltaic Assembled Circuit

GaSb TPV cells, sourced from JX Crystals (Figure 3-15a), were used within the TPV system. These cells feature a single-bus design and possess an EQE spectrum as shown in Figure 3-15b. The TPV cells have dimensions of 15 mm in length and 10 mm in width, with an ohmic contact bar width of 0.75 mm.

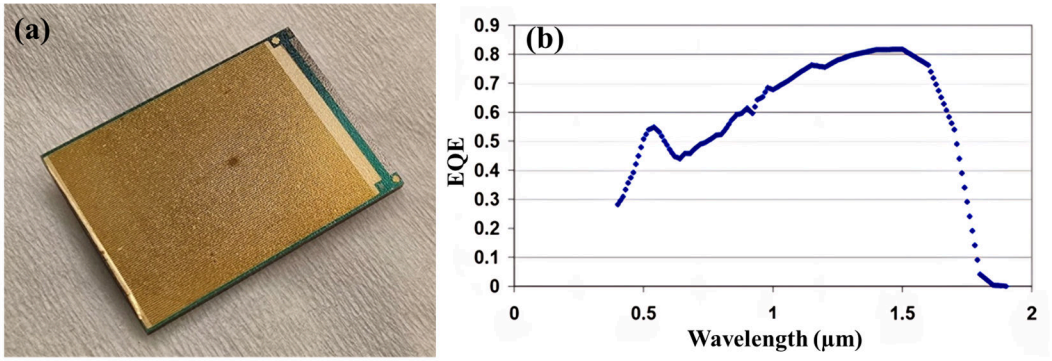


Figure 3-15 (a) GaSb TPV cell and its (b) external quantum efficiency

The TPV cell has a back contact and a top busbar, which, when connected, completes the circuit. The first step in the assembly process is to construct a back connector that ensures full contact with the back surface of the TPV cell. To achieve this, a copper sheet was cut into a rectangular shape with three connectors (Figure 3-16a) designated for the back surface. The TPV cell was then soldered onto the upper copper sheet.

A copper disk with a diameter of 6 cm and a thickness of 2 mm (Figure 3-16b) served as the base for all segments. To prevent electrical shorts between the upper sheet and the copper disk, a Thermalright Odyssey thermal pad (Figure 3-16c) [115] was used as an insulator. This pad also facilitated adhesion between the back surface of the sheet and the upper disk.

For the top surface, a PCB was cut into a trapezoidal shape (Figure 3-16d) and drilled to simultaneously connect the front busbar and clamp the TPV cell to the disk, ensuring improved electrical contact. Finally, two wires were soldered, one to the PCB and the other to the copper sheet, completing the TPV circuit (Figure 3-16e).

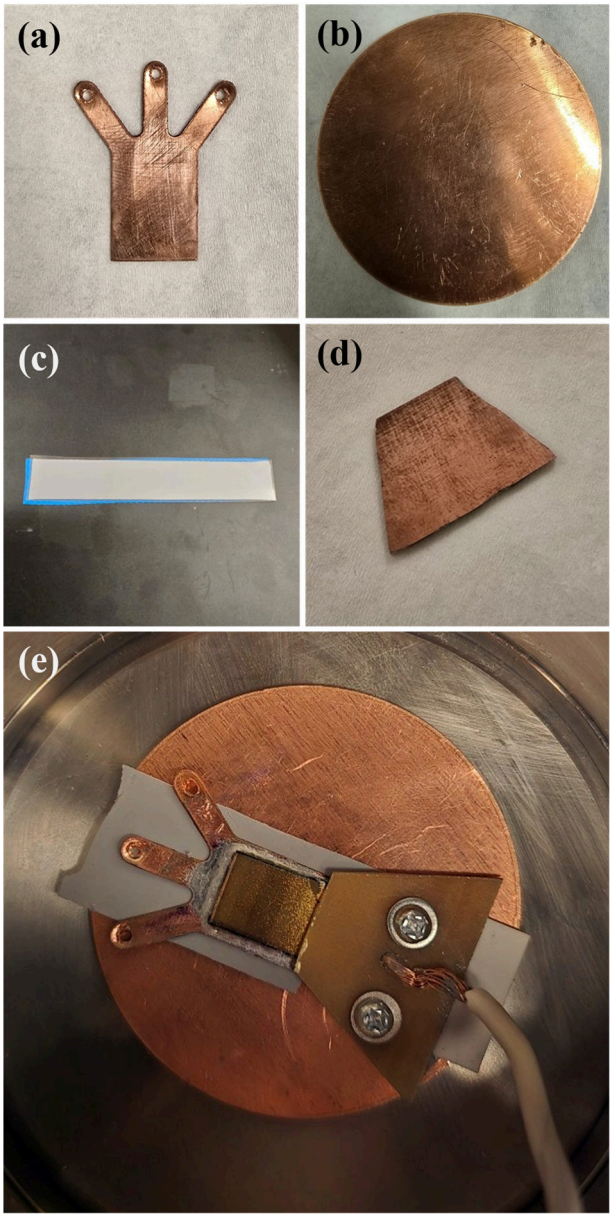


Figure 3-16 TPV cell (a-d) connectors and (e) assembled circuit

To manage radiation emitted to off-normal angles by the absorber-emitter, a black anodized aluminum baffle (shown in Figure 3-8c) measuring 10 cm × 10 cm with a thickness of 1 mm was utilized. This baffle was placed between the absorber-emitter and the TPV cell to limit the exposure of the TPV substrate to off-normal illumination. Additionally, the baffle serves as mechanical support for the spectral filter, described in the following paragraph, holding it securely above the TPV cell.

To harvest in-band photons from the emitter surface while simultaneously reducing unwanted heating by out-of-band radiation, a TECHSPEC OD 2.0 Shortpass spectral filter with a 1600 nm cut-off wavelength was employed [116]. As shown in Figure 3-17, this filter provides an average transmission of 95% at wavelengths below 1600 nm. Based on the TPV cell's EQE curve (see Figure 3-15b), the filter enhances system performance by allowing useful emitter radiation to reach the cell.

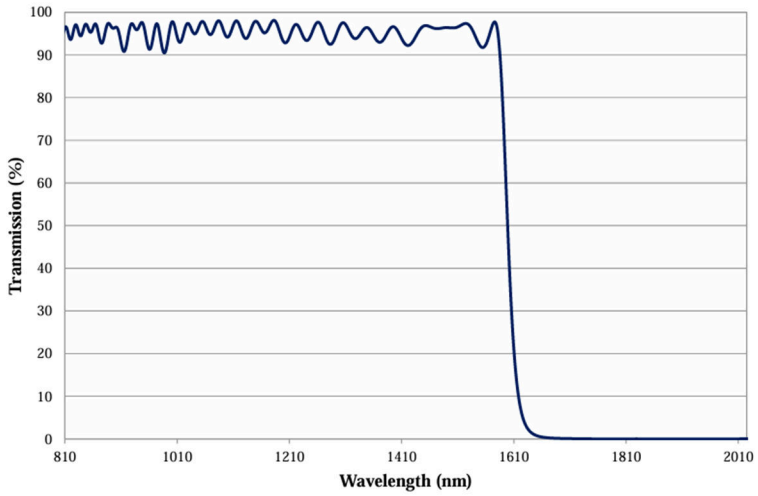


Figure 3-17 1600nm Spectral filter coating performance [116]

3.2.2.4 Cooling System

The Tubed Cold Plate series offers an efficient and economical solution for thermal management in applications where liquid cooling is preferred over air cooling. This cold plate, (Advanced Thermal Solutions TCP-1001 [117], shown in Figure 3-18, [117] is fabricated using a press-fit method to attach the copper tubes directly to the plate, ensuring optimal heat transfer without the use of thermal-insulating materials like epoxy. This direct, press-fit connection enhances heat transfer performance. The cold plate comes equipped with 3/8" push-to-connect fittings, ensuring a secure and reliable connection between the cold plate and the inlet/outlet tubing. The length of the cold plate is 152.0 mm, its width is 127.0 mm, and its height is 15.0 mm, with an overall length of 229 mm and four tube passes.



Figure 3-18 Tubed cold plate

Thermal specifications for the product will be provided in the following table:

Table 2 Thermal performance of tubed cold plate [117]

Flow Rate LPM(GPM)	Resistance (°C/W)	Differential Pressure (DP) kPA (psi)
1.9 (0.5)	0.021	3.58 (0.52)
3.7 (1.0)	0.016	10.82 (1.57)
5.7 (1.5)	0.013	21.16 (3.07)
7.6 (2.0)	0.012	35.16 (5.10)

To integrate the feedthrough into the closed-loop vacuum system, a liquid feedthrough (Figure 3-19) from KJLC was selected, specifically designed to enable fluid transfer while maintaining vacuum integrity. These feedthroughs are UHV welded to the designated flange type, ensuring a secure and leak-tight connection. The chosen model features a KF 40 flange with an outer diameter of 2.16 inches, a tube diameter of 1/4 inch, and a Swagelok termination type. This configuration ensures efficient and reliable fluid circulation within the closed-loop system.



Figure 3-19 Liquid feedthrough

To establish a secure and efficient connection between the chiller and the cooling plate within the cooling system, a 1/4-inch stainless steel tubing was utilized. Since both the chiller and the cooling plate feature 3/8-inch tube connections, appropriate fittings and adapters were required to ensure compatibility. For the connection between the chiller and the vacuum feedthrough, a Reducer, 1/4 in. Tube OD x 3/8 in was employed. Swagelok Tube Adapter (Figure 3-20a). Inside the vacuum chamber, where the 1/4-inch tubes interface with the cooling plate, a Bulkhead Reducing Union, 1/4 in. OD x 3/8 in. OD was used (Figure 3-20b).

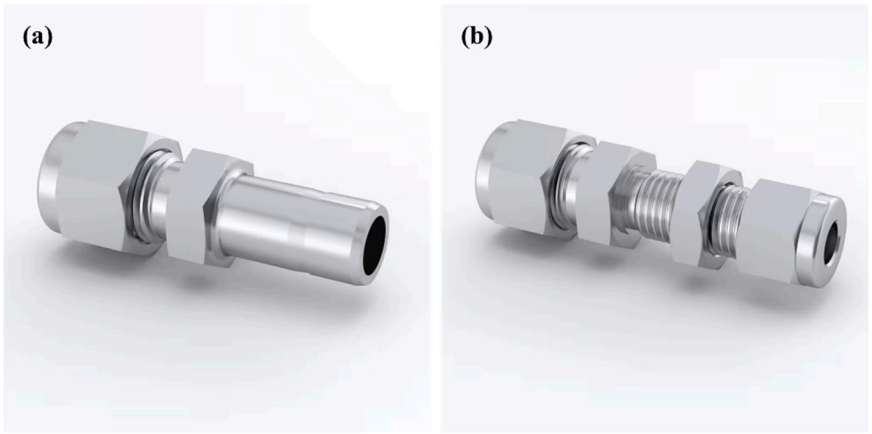


Figure 3-20 (a) Reducer tube adaptor, (b) bulkhead reducing union

3.2.3 Experimental Preparation and Data Acquisition

After assembling the cooling system by connecting the cooling plate and the fluidic feedthrough using stainless steel tubing, the cooling plate was secured inside the vacuum chamber. Subsequently, the TPV circuit configuration was mounted on top of the cooling plate. Due to the positioning of the feedthrough, the cooling plate was aligned at the mid-plane of the vacuum chamber, thereby ensuring that the TPV cell was also centrally positioned. Following the placement of the TPV cell, the black baffle, with a rectangular opening in the middle (Figure 3-21a), was positioned above the TPV to reduce the absorption of off-normal radiation. To secure the TPV cell firmly onto the cooling plate, enhance thermal contact, and improve cooling efficiency, metal zip ties (Figure 3-21b) were used to clamp the TPV circuit to the cooling plate. Additionally, a thermocouple (Figure 3-21c) was placed near the TPV cell surface to continuously monitor its temperature during operation. Finally, the spectral filter (Figure 3-21d) was placed on top of the baffle to transmit desired photon wavelengths to the TPV cell while minimizing unwanted radiation, and the TPV terminals were connected to the electrical feedthrough.

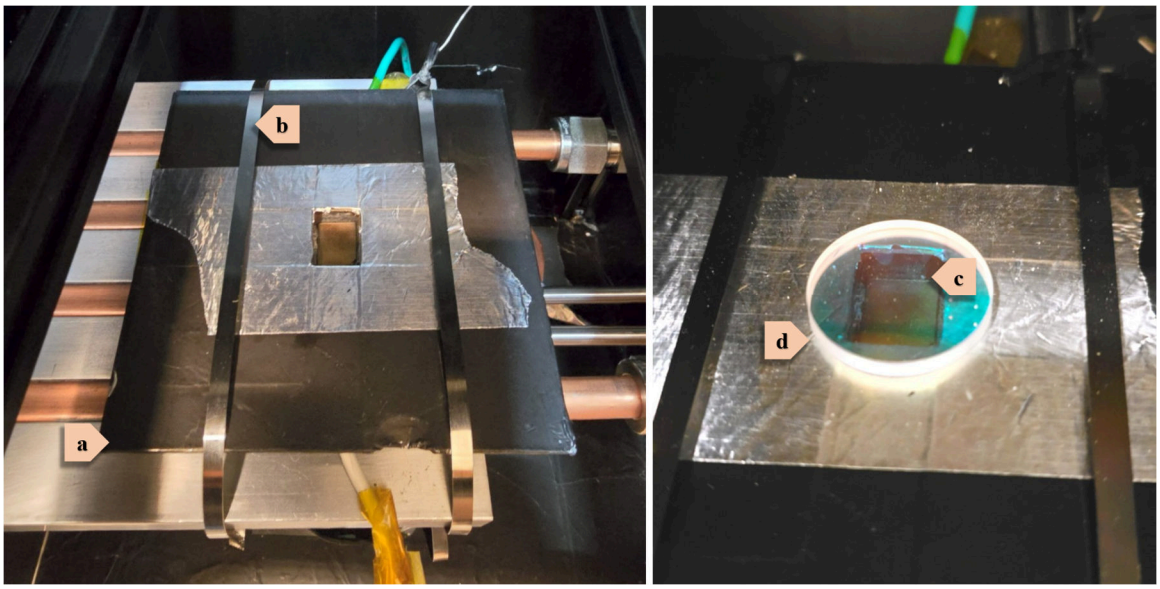


Figure 3-21 TPV system components on top of the cooling plate including (a) the black baffle with a rectangular opening, (b) metal zip ties, (c) thermocouple, and (d) the spectral filter

The next step involved positioning the emitter segment within the chamber. Initially, the ceramic insulation sheet (Figure 3-14b) was secured in place using Kapton tape, after which the remaining

components were assembled according to Section 3.2.2.2. To prevent direct irradiation from the halogen lamp from reaching the TPV cell, since the intended role of the lamp was solely to elevate the emitter temperature as a supplementary source rather than directly generate electricity, the absorber-emitter was carefully placed to avoid any light leakage.

Accurate temperature measurement requires placing the thermocouple on the emitting surface, additionally, because the AlN surface has higher emissivity, it was preferable for the AlN to face the TPV cell. Therefore, the absorber-emitter was oriented with the tungsten-coated surface facing upward, and the thermocouple was placed on the ceramic substrate, which is the emission side, to accurately measure its temperature. Additionally, another thermocouple was attached to the stainless-steel surface to monitor and quantify heat loss. To minimize heat conduction from the emitter assembly to the aluminum frame, ceramic insulation sheets were inserted at the points of contact between the stainless steel and the frame. Finally, with the emitter wires connected to the electrical feedthrough, this portion of the experimental assembly was completed and Figure 3-22 shows the whole layout.

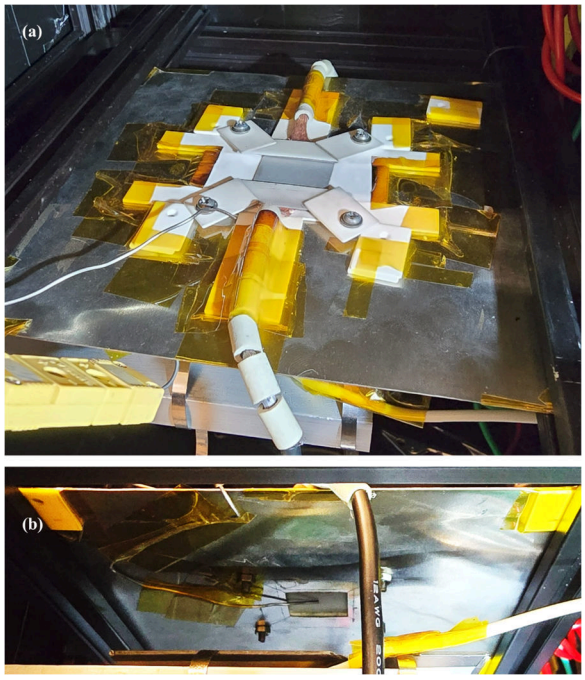


Figure 3-22 Emitter holder system viewed from (a) the top and (b) the bottom

To accurately position the light source above the emitter, the focal distance of the elliptical reflector was calculated. By adjusting this distance, the maximum achievable temperature from the halogen bulb source was obtained at the emitter surface. Additionally, a thermocouple was placed on top of the elliptical reflector holder sheet to monitor its temperature during operation. Also, the distance measured between the surface of the emitter, and the TPV cell surface was 4 cm, and this value was used when calculating the VF between absorber-emitter and TPV cell for further steps (mentioned in section 4.1.2.2). The completed assembly of the experimental setup inside the vacuum chamber is illustrated in Figure 3-23.

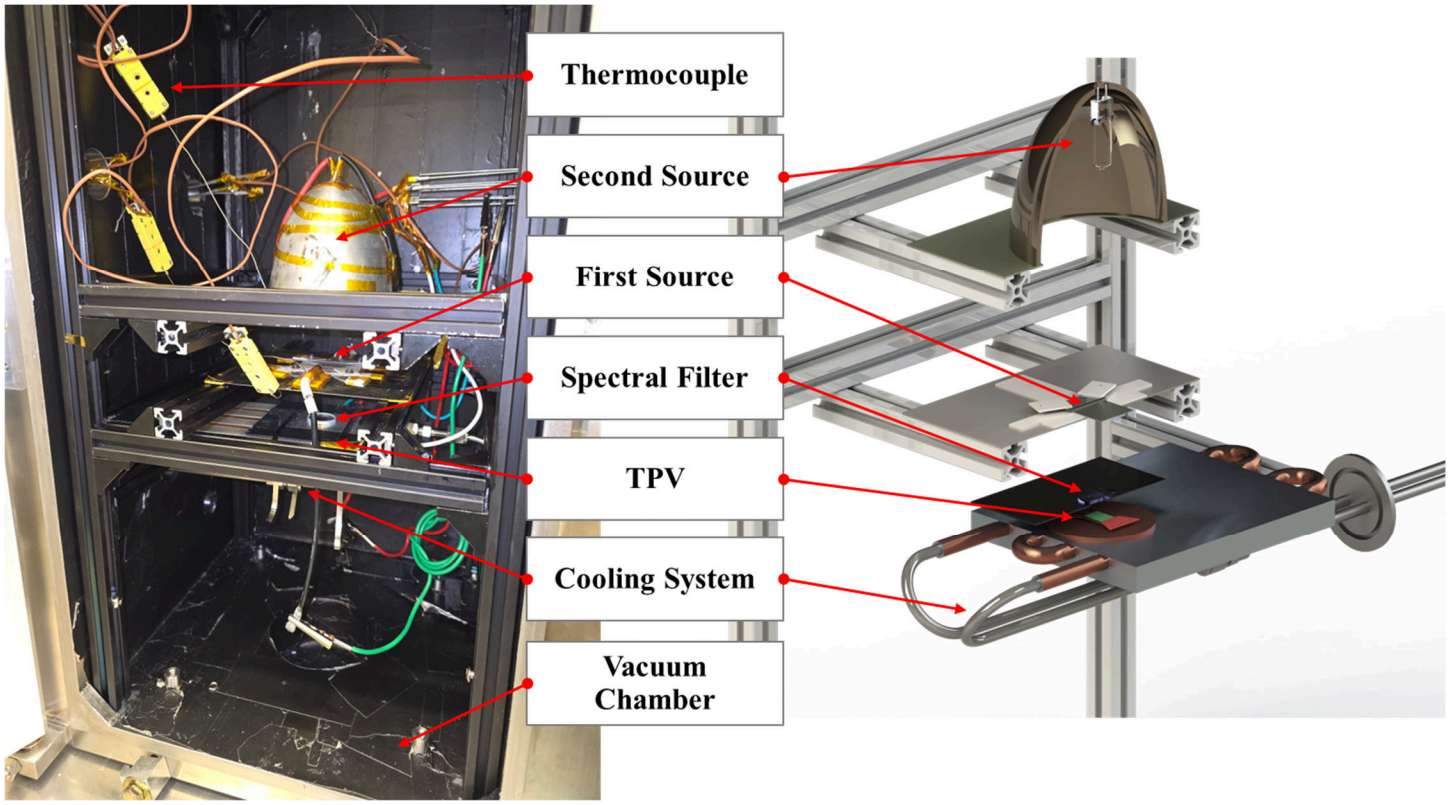


Figure 3-23 Completed experimental assembly

Initially, the absorber-emitter was tested to evaluate its thermal performance. The voltage varied from 1 to 10 V, and the corresponding temperatures were recorded at each step to assess the relationship with the applied electrical input.

Subsequently, to begin the experiment and conduct tests under both separate and simultaneous conditions, the vacuum chamber was first evacuated to a pressure of approximately 10 mTorr.

Simultaneously, the chiller system was activated to circulate an ethanol–water mixture, lowering the coolant temperature to –5 °C.

In the first step, the emitter was powered through five progressively increasing fixed power levels, each corresponding to nearly similar temperatures. At each power level, the electrical output of the TPV cell was measured using two multimeters, one as an ammeter and the other as a voltmeter. First, the I_{SC} and V_{OC} were recorded. Subsequently, to obtain the IV curve, the circuit shown in Figure 3-24 was used, in which the ammeter is connected in series and the voltmeter parallel with the TPV. By adjusting a variable resistor (potentiometer), the resistance was changed step by step, and the corresponding voltage and current values were recorded to plot the IV curve.

In experiments where both the lamp and Joule heating were used simultaneously to heat the emitter, the same five power levels, each corresponding to a unique temperature and previously used in separate heating tests, were applied again. In this step, the emitter was maintained at predefined power levels, while the halogen lamp was gradually powered up to provide additional heating. As the lamp power increased, the emitter temperature increased, which led to a rise in its electrical resistance and a drop in current. To keep the emitter power constant, the input voltage had to be increased accordingly. At each step, the TPV output was measured again, including I_{sh}, V_{oc}, and the IV curve, to determine how much the electrical output increased when both sources were working together.

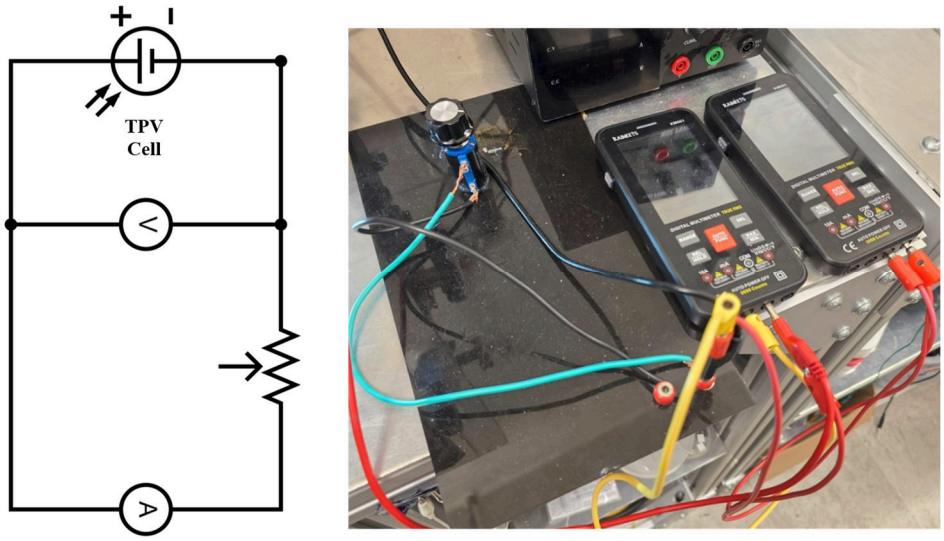


Figure 3-24 IV Curve circuit measurement

To process and present the results of three sets of data, the average was first calculated, followed by the standard deviation to accurately represent them in plots and graphs. The standard deviation was calculated using Equation *3.23*, as shown below:

$$s = \sqrt{\frac{1}{n-1}\sum_{i=1}^{n}(x_i - \bar{x})^2} \qquad 3.23$$

Here, the average value $\bar{x}$ was determined using the following equation:

$$\bar{x} = \frac{1}{n}\sum_{i=1}^{n} x_i \qquad 3.24$$

4 Chapter 4: Results & Discussion

4.1 Analytical

4.1.1 COMSOL Simulation Results for the Emitter

After running the simulation with the specified boundary conditions, one representative result is shown in Figure 4-1a. In this case, the substrate geometry is a square base measuring 25 mm on each side with a height of 0.5 mm. The tungsten coating thickness is 1 μm, and the applied input voltage is 10 V.

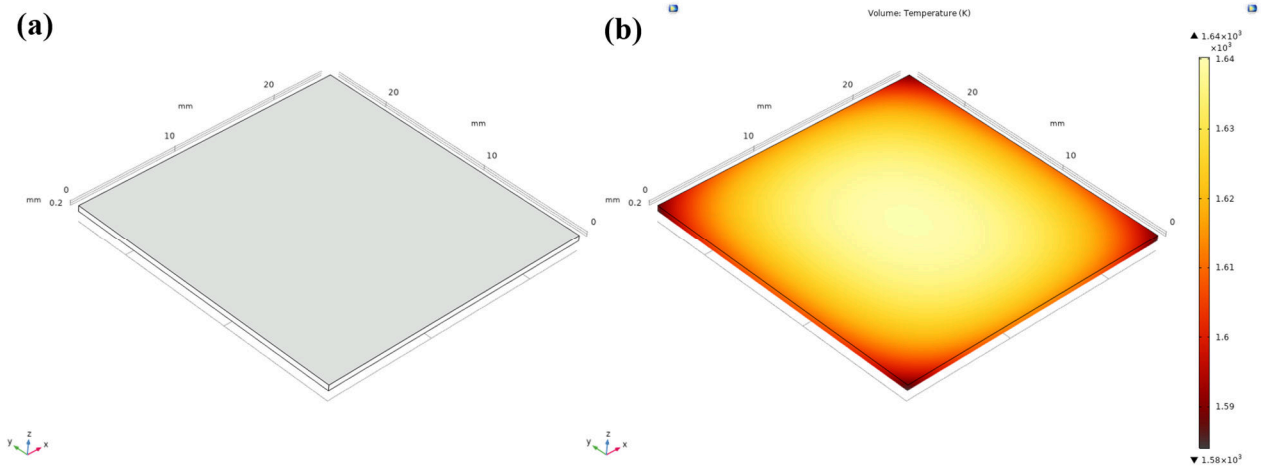


Figure 4-1 Simulation temperature result from the sputtered substrate with 1 μm tungsten layer and an input voltage of 10 V

Figure 4-1b illustrates the temperature distribution across the sputtered substrate. The maximum temperature, approximately 1640 K, occurs at the center of the substrate, while the minimum temperature, around 1580 K, is observed at the corners. The only mode of thermal loss in this simulation was surface radiation. Since the corners are more exposed to the colder surroundings and have a larger VF, they radiate more heat, resulting in slightly lower temperatures compared to the center.

The simulation output included current density and temperature distributions. To determine the temperature as a function of input power, the electrical power was calculated from the simulated current density and applied voltage using the following equation:

$$P_{in} = V \cdot I = V \cdot (J \cdot t \cdot w) \quad 4.1$$

where V is the applied voltage, $J(A/m^2)$ is the simulated current density, t is the thickness of the sputtered tungsten layer, and w is the substrate edge width through which the current flows.

Figure 4-2 shows the emitter temperature as a function of electrical input power for tungsten coatings ranging from 50 nm to 1000 nm in thickness. The simulations were performed by sweeping both the coating thickness (50–1000 nm) and the input voltage (2–10 V). As an example, at 50 nm thickness and 10 V, the coating consumed 21.91 W to reach 934.36 K, while at 1000 nm thickness and the same voltage, it consumed 228.39 W to reach 1640 K.

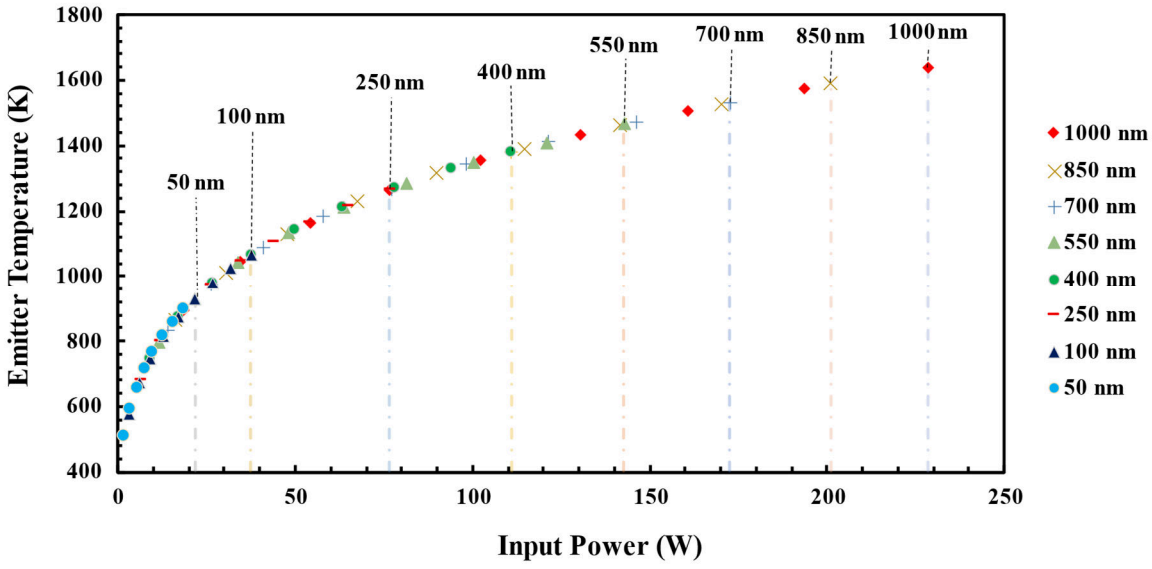


Figure 4-2 Emitter temperature relative to joule heating power for various sputtered tungsten thicknesses.

The same voltage range was applied uniformly across all samples (2 V to 10 V in 1-volt increments), and the results show that all curves follow a similar nonlinear trend, with the main difference

being the total power consumed at each voltage level, which increases with increasing thickness. This means that for a given target temperature, the required input power is similar across thicknesses, but the electrical characteristics differ: thin coatings have higher resistance and therefore lower current at a given voltage, whereas thicker coatings carry higher currents at lower voltages. For example, a 100 nm coating at 10 V carries only 3.742 A, while a 1000 nm coating at just 3 V carries 11.496 A.

In practical terms, extremely thin coatings may degrade under extended experimental use. Conversely, thicker coatings require currents exceeding 10 A to achieve the target operating temperature (~1200 K), which demands robust wiring and power components. Additionally, thicker layers increase fabrication costs due to longer sputtering times and greater material usage.

4.1.2 Analytical Performance Results of the Thermophotovoltaic Systems

4.1.2.1 Numerical Result from the Evaluation of the amount of In-Band Photons

Initially, the in-band emissive power was calculated for three different TPV cells (Si, GaSb, and InGaAs) in three different configurations, denoted as Cases 1 to 3, in Figure 4-3a. Figure 4-3b-d presents this analytical comparison, where the horizontal axis represents the wavelength (μm), and the vertical axis shows the spectral emissive power. The blue-shaded region corresponds to the power of the in-band emitted photons when the TPV system is powered by a single heat source with a power of 5 W/cm² (Case 1 in Figure 4-3). The yellow-shaded region represents twice the sum of the power of the in-band emitted photons when the TPV system is powered by a 5 W/cm² heat source (Case 2 in Figure 4-3). The pink-shaded region shows the power of the in-band emitted photons for the multisource condition wherein both heat sources are applied to the TPV system simultaneously (Case 3 in Figure 4-3a). In Case 3, the TPV system is powered by a total of 10 W/cm². The text boxes within each graph indicate the total in-band emissive power for each configuration.

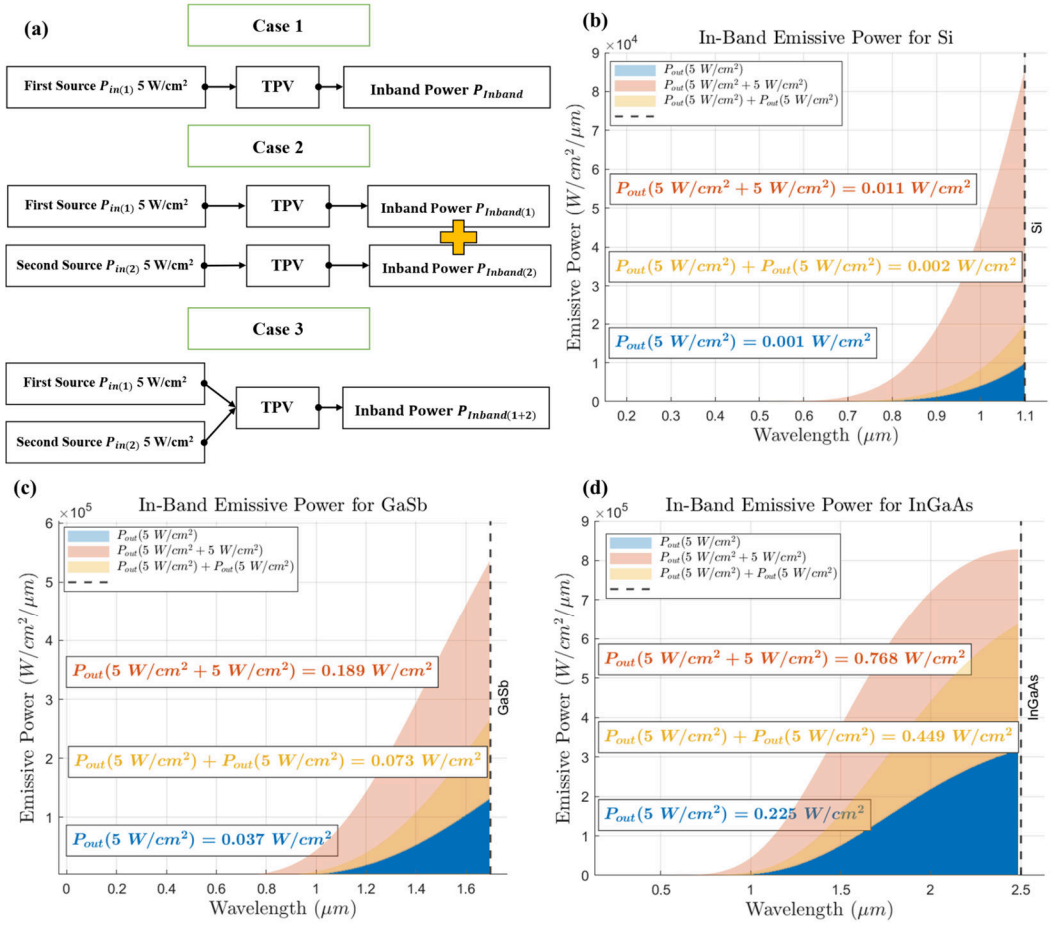


Figure 4-3 In-band emissive power of Si, GaSb, and InGaAs cells under single, separate, and simultaneous 5 W/cm² heat sources, showing enhanced output in multisource mode.

For the Si cell with a bandgap of 1.1 eV, the total in-band power increases from 0.002 W/cm² in case 2, where the emitter is powered by each 5 W/cm² source individually and the results are summed conceptually, to 0.011 W/cm² in case 3, where both sources act on the same emitter simultaneously. The output power from the GaSb cell, which has a bandgap of 0.72 eV, shows an increase from 0.073 W/cm² to 0.189 W/cm² when switching from case 2 to case 3. Finally, for the InGaAs cell with a 0.6 eV bandgap, the in-band power increases from 0.449 W/cm² to 0.768 W/cm².

Here, the enhancement factor is defined as the ratio of case 3 to case 2. Based on this definition, the results correspond to enhancement factors of approximately 5.5, 2.5, and 1.7 for Si, GaSb, and InGaAs,

respectively. This demonstrates that simultaneous powering from multiple heat sources significantly increases the total in-band emissive power, with the effect being more pronounced for materials with larger bandgaps.

4.1.2.2 Analytical Result of Single and Multi-Source TPV System Comparison

To compute the output power of the TPV cell, Equations *3.14* to *3.18* were applied. This required first estimating the VF, as described in detail in Section 3.1.2.2, which yielded a value of 0.0265. Additionally, the emissivity was needed to determine the net spectral radiant heat flux. Based on Figure 3-13, an average emissivity of 0.7 was adopted for the AlN radiating surface.

Using these parameters, MATLAB simulations were performed, producing the results shown in Figure 4-4. The horizontal and vertical axes represent the input power derived from corresponding emitter temperatures ranging from 500 K to 1270 K, which corresponds to 0.21–10.29 W/cm². The color bar in each plot indicates the TPV cell output power in mW/cm². Specifically, Figure 4-4a shows the total TPV output power when two sources operate individually (Case 2), with the total being $P_{out(1)} + P_{out(2)}$. In contrast, Figure 4-4b presents the TPV output power when the same two sources operate simultaneously (Case 3), with the output power denoted as $P_{out(1+2)}$. Finally, Figure 4-4c illustrates the power enhancement ratio, calculated as $P_{out(1+2)}/(P_{out(1)} + P_{out(2)})$, which quantifies the relative improvement of simultaneous powering the TPV system with the two heat sources (Case 3) as compared to applying the heat sources separately (Case 2).

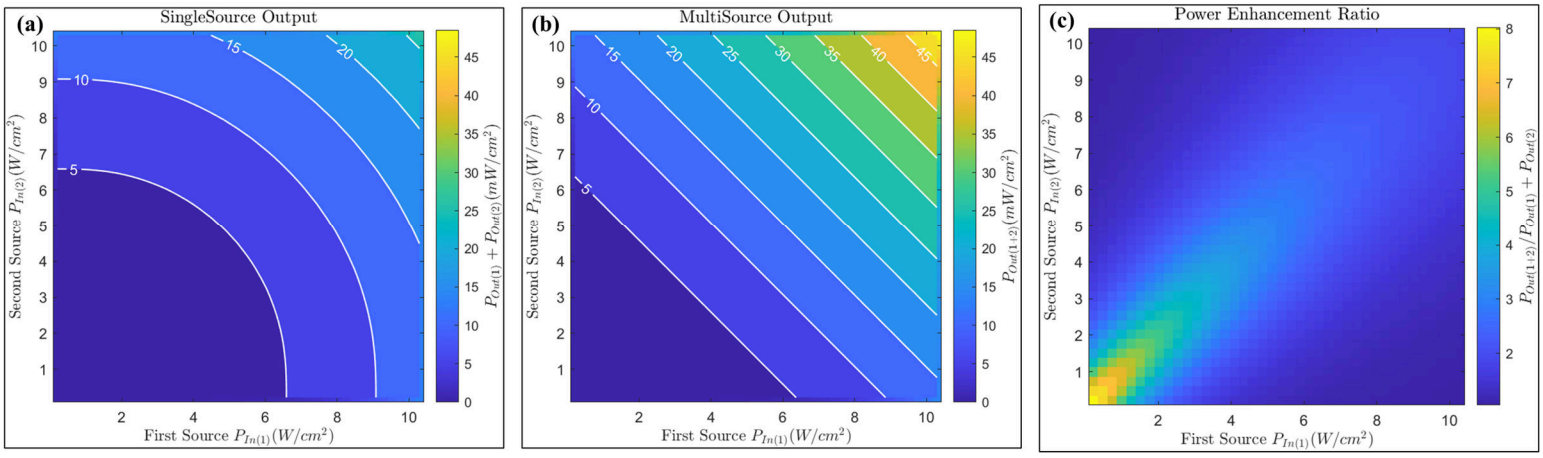


Figure 4-4 (a) the sum of the output power from a TPV system when it is powered by two sources individually (case 2) (b) the output power from a TPV system when it is simultaneously powered by two sources (case 3)). (c) the power enhancement (case 3/case 2) is achieved by powering the TPV system with two power sources simultaneously as compared to the power generated when the power sources are used individually.

From the heatmaps shown in Figure 4-4, it is evident that in the single-source configuration, the maximum output is 25.9 mW/cm², whereas in the multi-source configuration, the output for the same total input power rises to 48.52 mW/cm². In terms of enhancement, the highest ratio is approximately 802%, which occurs at the lowest input powers for both sources. At the highest output levels, the enhancement ratio decreases to about 187%, indicating that the relative benefit diminishes at elevated operating conditions as the system approaches its saturation limit.

These results suggest that in practical TPV designs, especially when multiple heat sources are available, strategically balancing their individual power contributions can significantly improve system performance. Notably, maximum gains occur at low to moderate input powers, making this strategy particularly beneficial for systems with constrained total energy supply.

4.2 Experimental

4.2.1 Absorber–Emitter Performance

This section focuses on evaluating the experimental performance of the absorber–emitter assembly. The absorber–emitter assembly was first tested independently, without integration into the TPV system, to evaluate its inherent thermal performance and to characterize the relationship between emitter temperature and electrical input power. The tests were conducted under vacuum conditions to prevent oxidation of the tungsten coating during high-temperature operation (Figure 4-5).

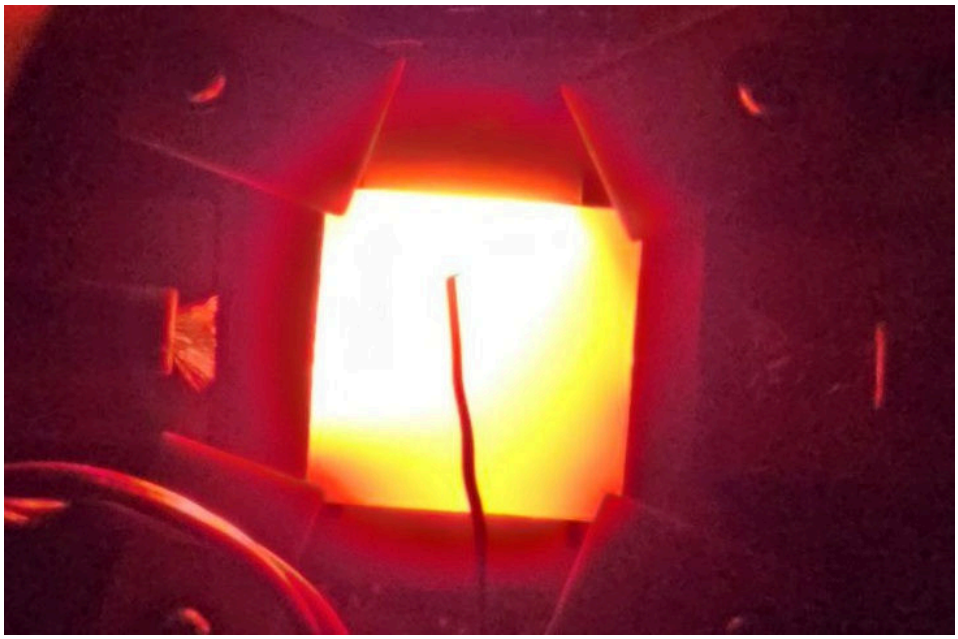


Figure 4-5 Absorber–emitter assembly during experimental testing

Figure 4-6 presents the measured temperature of the absorber–emitter as a function of the supplied electrical power. However, it is important to note that during testing, several sources of heat loss such as conduction through the stainless-steel support and wiring, as well as convection due to the limited vacuum level, were unavoidable and could not be precisely quantified. These losses resulted in a significant discrepancy between the supplied electrical power and the actual power delivered to the emitter surface.

Consequently, a more accurate estimation of the input power was calculated based on radiative heat transfer from the emitter's surfaces.

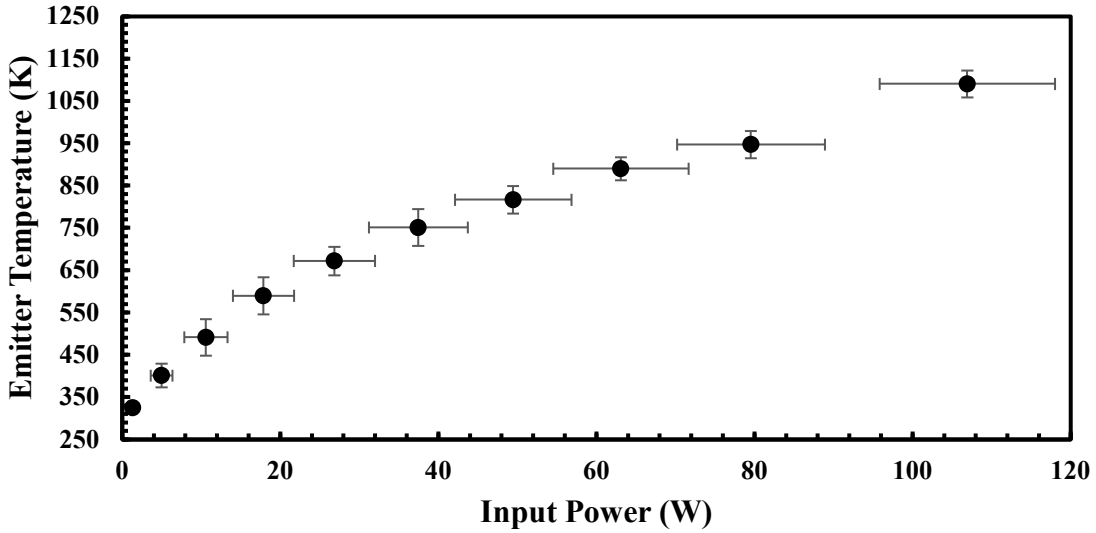


Figure 4-6 Absorber-emitter temperature relative to electrical input power

The actual power transferred to the emitter was determined using the Joule heating–based radiative loss model:

$$P_{actual} = \sigma \cdot \varepsilon_{AlN}(T) \cdot A_{AlN} \cdot \left(T^4 - T_{ambient}^4\right) + \sigma \cdot \varepsilon_W(T) \cdot A_W \cdot (T^4 - T_{ambient}^4) \qquad 4.2$$

where σ is the Stefan–Boltzmann constant, $\varepsilon_{AlN}(T)$ and $\varepsilon_W(T)$ are the temperature-dependent emissivities of the AlN substrate and tungsten layer, respectively, and A_{AlN} and A_W are their corresponding radiating areas.

In this approach, the emissivity was calculated as a function of temperature, and the resulting P_{actual} reflects the net radiative power responsible for the observed temperature rise. Figure 4-7 illustrates the relationship between the calculated actual input power and the emitter temperature.

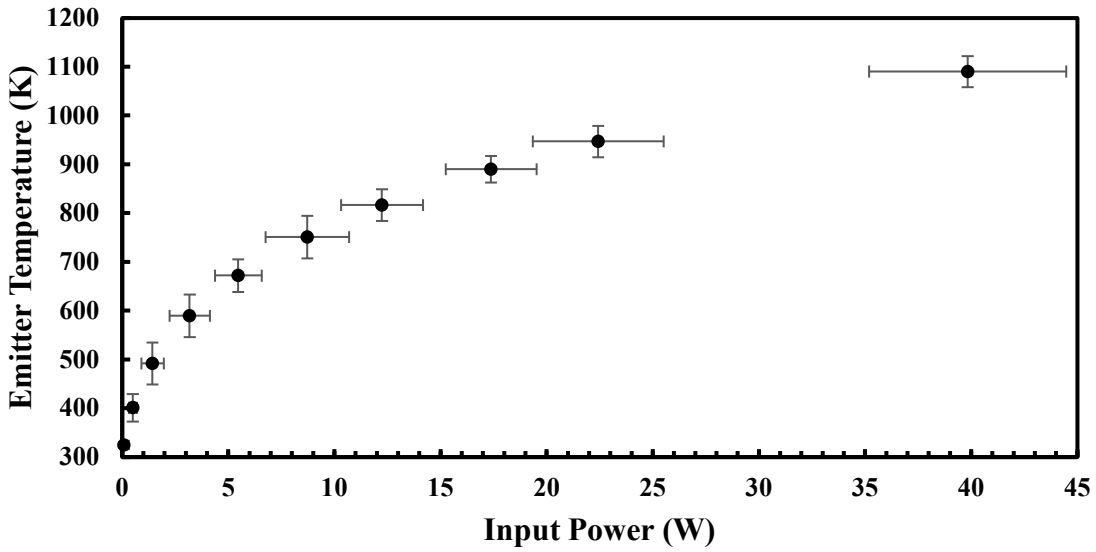


Figure 4-7 Emitter temperature relative to input power considering losses

As shown in Figure 4-7, when heat losses are taken into consideration the estimated input power is significantly reduced compared to the raw electrical input values. This corrected power measurement provides a more realistic basis for comparison with the simulation results, enabling a better understanding of the emitter's performance under practical operating conditions.

4.2.2 TPV Cell Performance Results

In this section, the experimental performance of TPV system is reported. First, the I-V curves were plotted for different experimental cases. Figure 4-8 presents six I-V curves measured at different emitter temperatures.

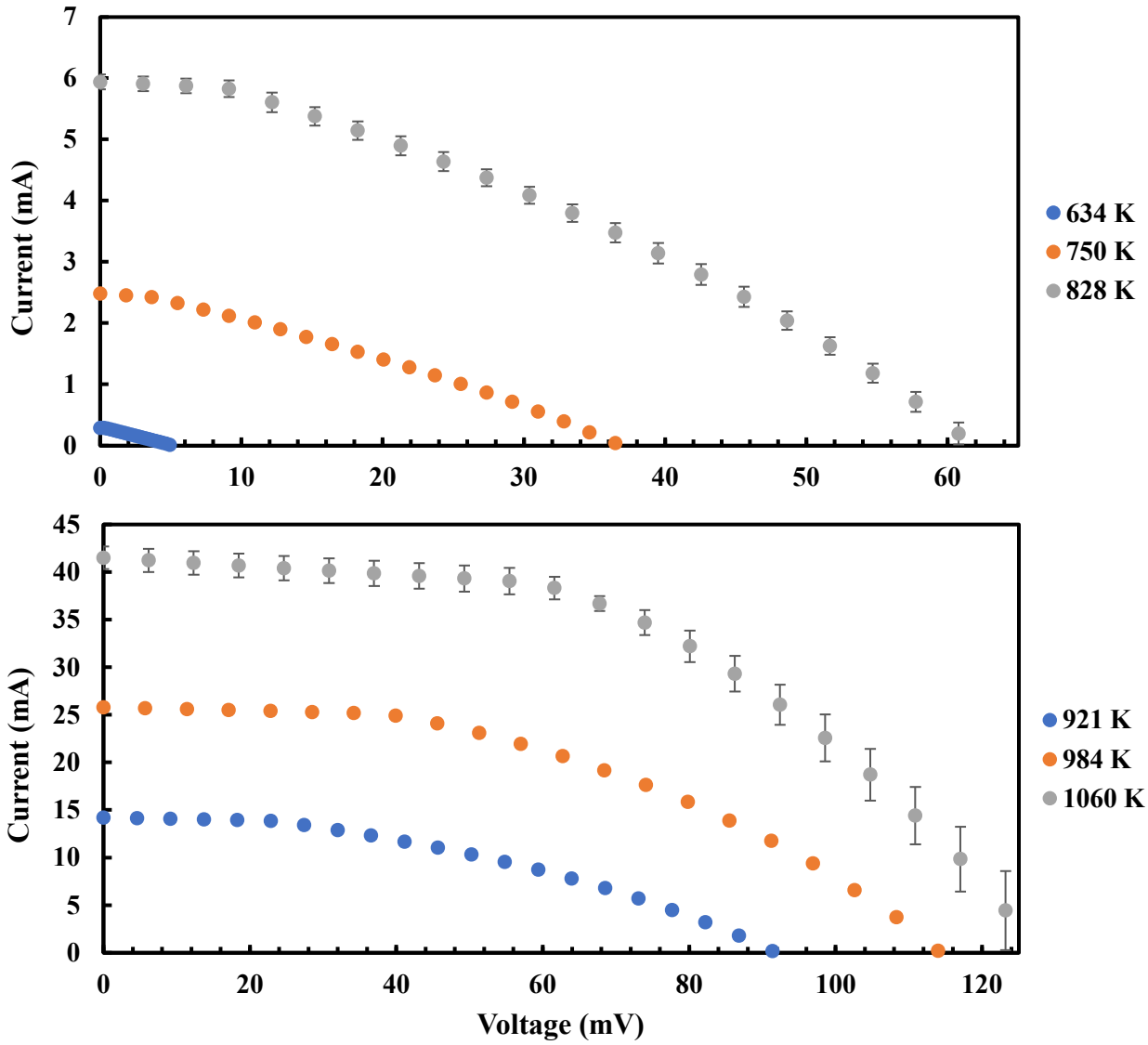


Figure 4-8 Measured IV curves of the TPV cell at various emitter temperatures.

Because recording I-V curves for every electrical power setpoint was both challenging and time-consuming, an alternative method was adopted to estimate the maximum power for each operating

condition. From the I-V curves measured at fixed setpoints (each repeated three times), the FF was calculated using Equation *3.23* as a function of temperature. These results are shown in Figure 4-9. A polynomial trendline was fitted to the data, resulting in Equation *4.3* for $FF(T)$. With this relationship, the maximum power at any setpoint could be calculated by multiplying I_{SC} and V_{OC} by the corresponding FF.

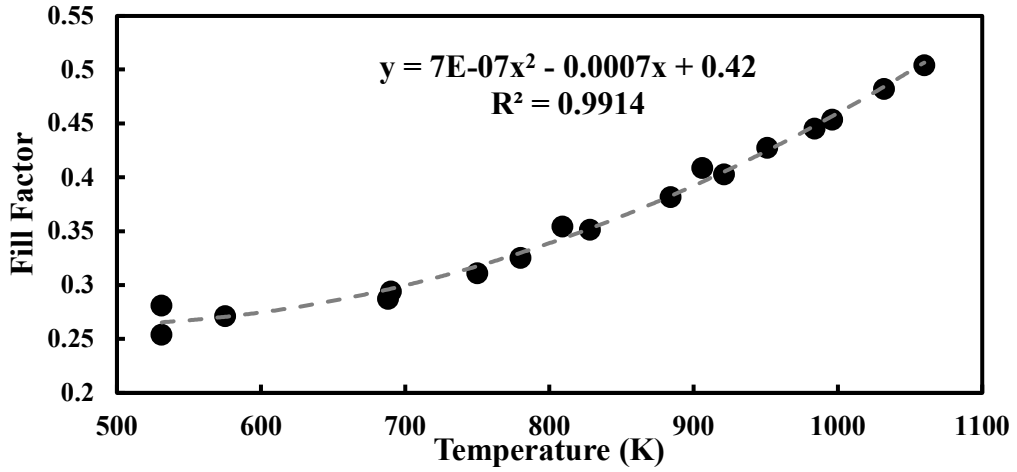


Figure 4-9 Experimental FF

$$FF(T) = 7E-7 \cdot T^2 - 0.007 \cdot T + 0.42 \qquad 4.3$$

Using the derived FF, the output power was plotted against emitter temperature (Figure 4-10). In this experiment, the maximum achieved emitter temperature was 1060 K, corresponding to an electrical output of 2.584 mW from the TPV cell.

A useful comparison can be made with the results reported by Liu et al [89], where the GaSb TPV cell produced 3.4 mW and 2.3 mW at an emitter temperature of 1073 K for view factors of 0.0091 and 0.0062, respectively. These values are in close agreement with the present work, given the small difference in emitter temperature and geometric configuration, and they support the validity of the experimental results obtained here.

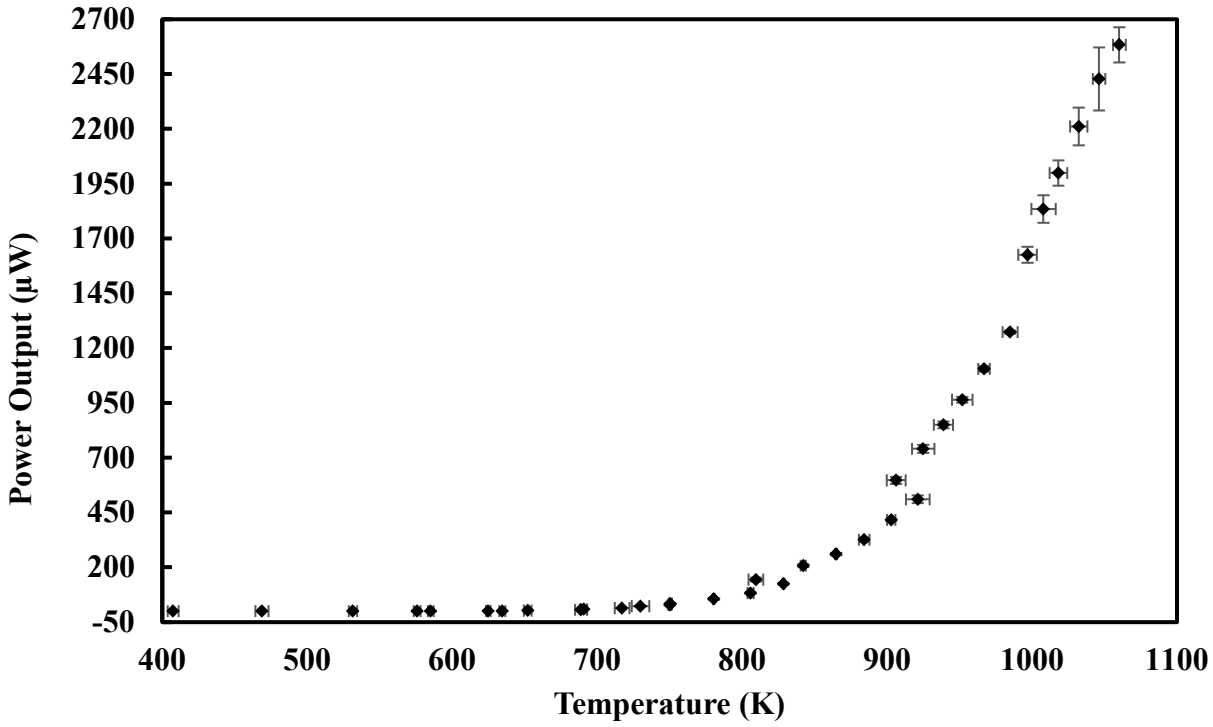


Figure 4-10 Measured TPV output power across different emitter temperatures

To evaluate the input powers, considering all conductive, convective, and parasitic radiative losses, the absorber–emitter temperature was used to calculate the radiative input power from each heat source when operated individually, according to Equation *4.4*. Only the AlN surface was considered here, as it directly faced the TPV cell:

$$P_{input} = \sigma \cdot \varepsilon_{AlN}(T) \cdot \left(T^4 - T_{ambient}^4\right) \qquad 4.4$$

The halogen lamp (second source) delivered between 0.08 and 0.619 W/cm², while Joule heating (first source) supplied between 0.41 and 3.77 W/cm². Figure 4-11 compares the TPV output power in multisource operation (color pillars) with the sum of outputs from each source operating individually (crossline bars) at the same total emitter power density.

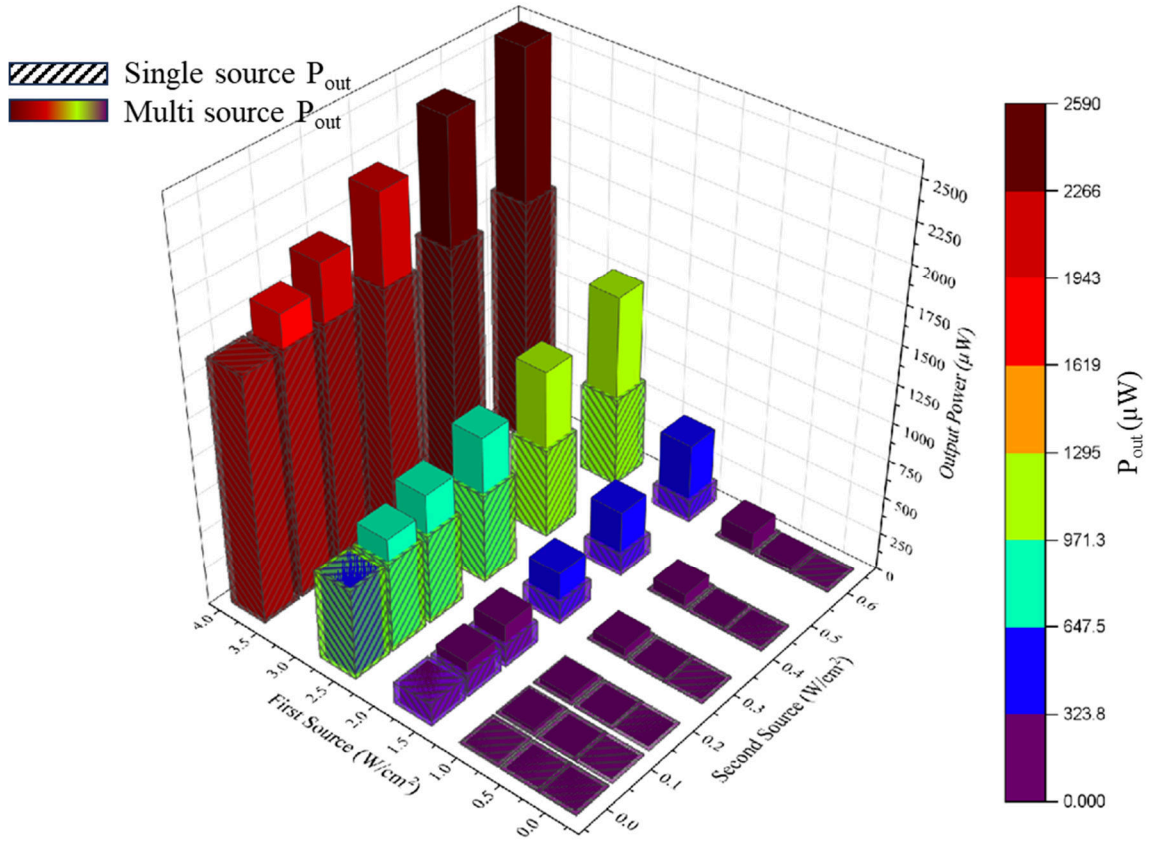


Figure 4-11 Comparison and demonstration of TPV system output power in multisource and separate modes across variations in emitter power density, with color pillars representing multisource operation and cross-line bars indicating separate source measurements

By dividing the electrical outputs by the TPV cell's active area (1.5 cm^2), the results were converted to output power density for direct comparison. Plotting the two conditions which are single-source and multi-source the results are shown in Figure 4-12. As previously mentioned, the power derived from Joule heating is referred to as the first source power, and the radiation from the halogen lamp incident onto the absorber-emitter provides the second source. Figure 4-12a shows the combined single-source operation (sum of outputs from the halogen lamp and Joule heating), Figure 4-12b shows multisource operation, and Figure 4-12c shows the enhancement ratio of multisource to single-source operation.

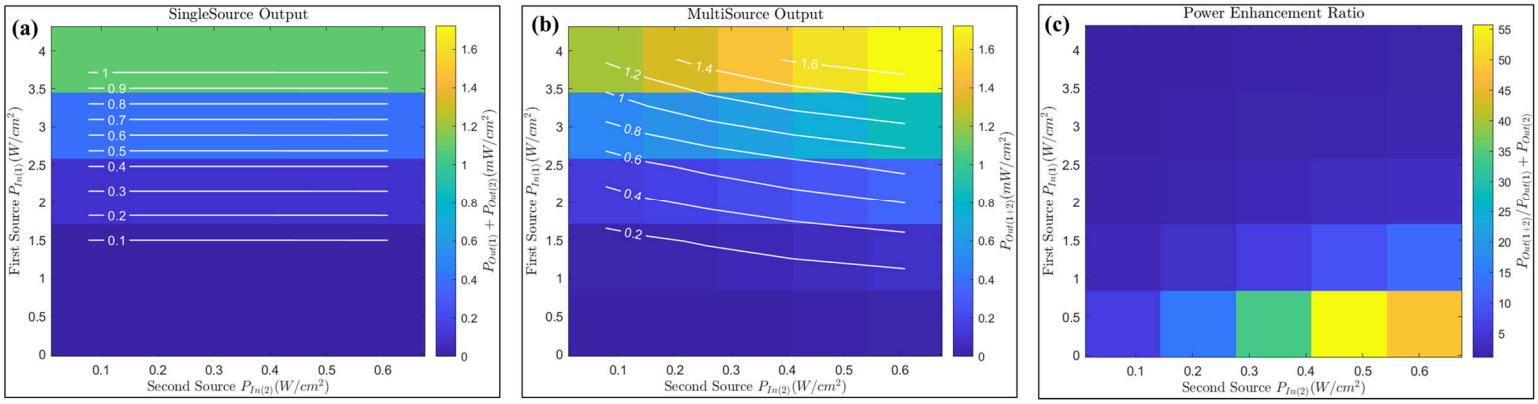


Figure 4-12 (a) the sum of the experimental output power from the TPV system when it is powered by halogen lamp and joule heater individually (case 2) (b) the output power from the TPV system when it is simultaneously powered by two heat sources (case 3). (c) the power enhancement (case 3/case 2) is achieved by powering the TPV system with two power sources simultaneously as compared to the power generated when the power sources are used individually.

The heatmap shown in Figure 4-12 reveals two key trends. First, the TPV output is mainly driven by the Joule heating source, while the halogen lamp plays a smaller, secondary role. Second, when both sources operate together, a clear synergistic effect appears. As seen in Figure 4-12b, the contour lines slope toward higher ($P_{in(2)}$), indicating that the addition of power form the second source boosts the output power more effectively than simply summing the contributions from each source alone. The results show that for a representative setpoint, the TPV output in single-source mode was 1.08 mW/cm², whereas multisource operation produced 1.72 mW/cm², an increase of 158%. The most pronounced enhancement occurred at low output powers, where the denominator in the ratio is small, meaning that even small absolute gains can lead to very large percentage increases. In these low-output cases, the enhancement ratio reached as high as 55.7 times.

4.3 Analytical–Experimental Correlation of Emitter and TPV System Performance

4.3.1 Absorber-Emitter Performance Comparison

In this section, the correlation of numerical and experimental results is studied. To compare the simulated results to the experimental results in Sections 4.1.1 and 4.2.1, the exact thickness of the sputtered tungsten film over the AlN ceramic sheet must be known. Scanning Electron Microscope (SEM) images were taken to capture cross-section images in micron resolution (Figure 4-13a) and images of the top surface (Figure 4-13b) of the absorber-emitter.

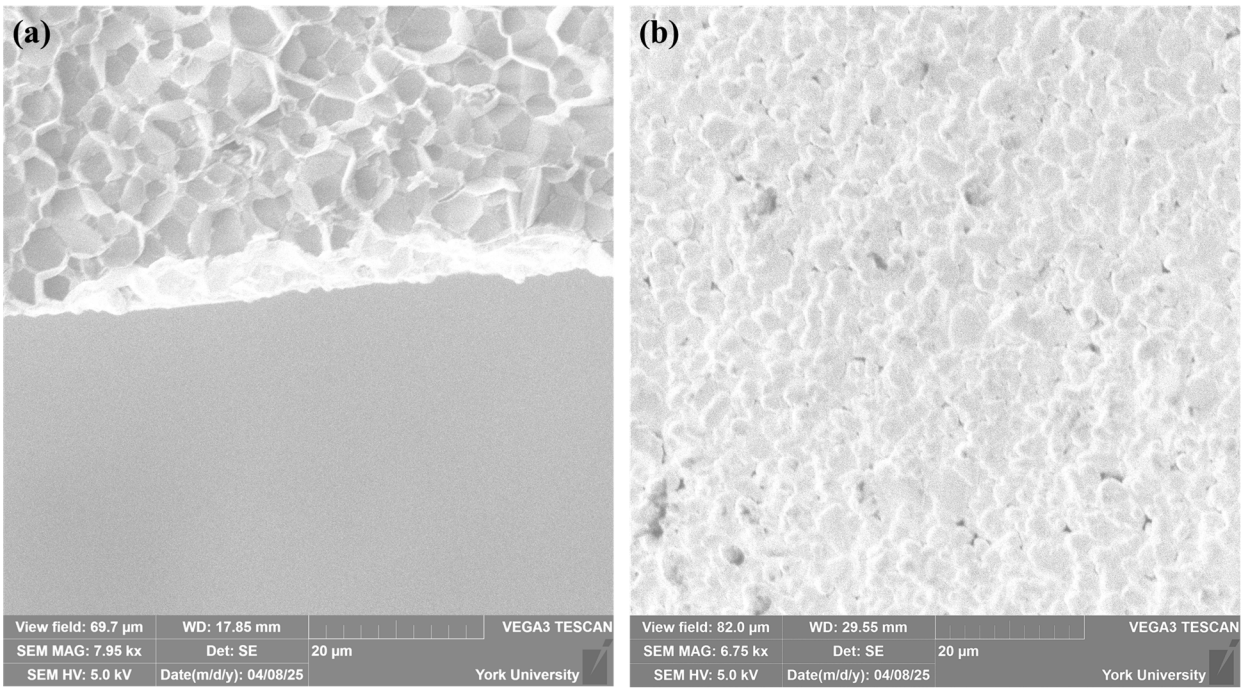


Figure 4-13 (a) cross sectional, and (b) top view SEM images of tungsten deposited onto a AlN substrate

However, as the SEM images appears in Figure 4-13, the thickness of the tungsten film could not be precisely determined because the tungsten did not form a planar layer with uniform thickness. Instead, the film exhibited significant roughness of surface, largely influenced by the underlying substrate's rough texture. In some areas of Figure 4-13a it can be seen that coating of the sputtered tungsten film is very thin and in Figure 4-13b the black spots represent holes in the coated surface. Moreover, since the tungsten

coating is not uniform, the electrical current does not distribute or flow according to the average thickness; instead, local variations in thickness dominate the current path and overall resistance.

Another method is using the electrical resistance and resistivity of tungsten in different powers and temperatures to find the thickness from experimental results. In this method, the resistance was found from the equation below:

$$R = V/I \tag{4.5}$$

Then, from temperature dependant resistivity $\rho(T)$ the thickness of sputtering can be obtained:

$$R = \frac{\rho \cdot l}{A} = \frac{\rho(T) \cdot l}{t \cdot w} = \frac{\rho(T)}{t} \rightarrow t = \frac{\rho(T)}{R} \tag{4.6}$$

In this case, since the substrate is square, the width and length are equal, then they can be crossed out them by each other. Averaging all three sets of data previously mentioned in the section 4.2.1 the value was **260 nm**.

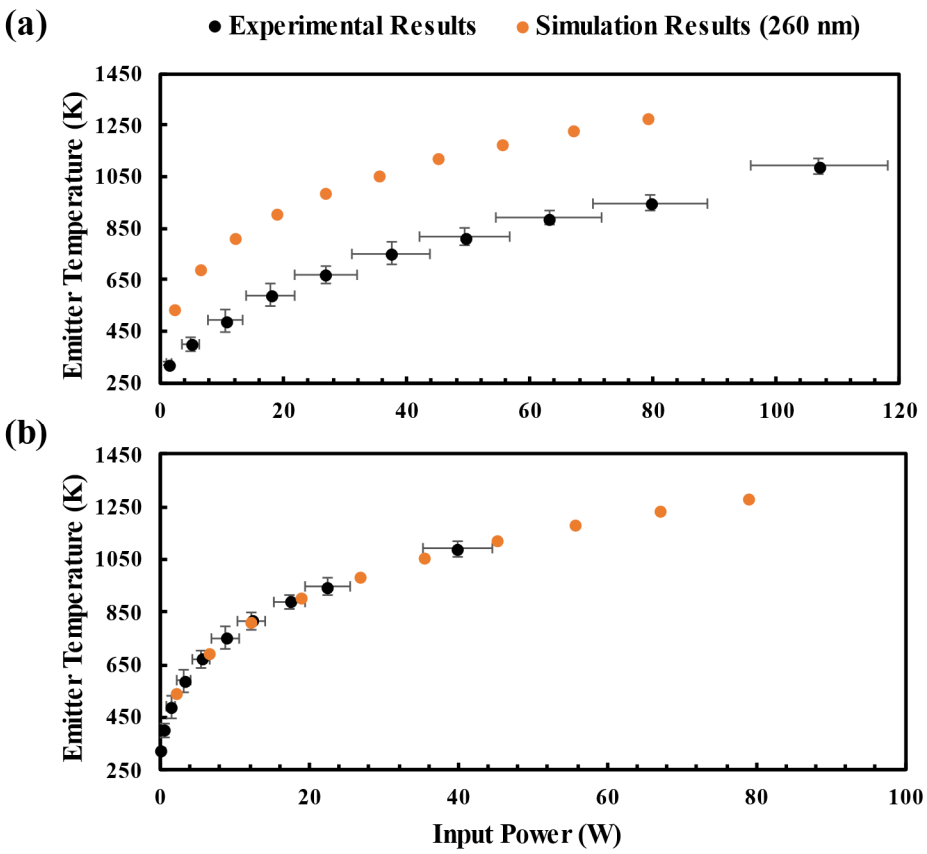


Figure 4-14 Comparison of experimental and simulated emitter temperatures with a 260 nm tungsten coating: (a) using supplied electrical power and (b) using radiative input power corrected

Figure 4-14 presents the comparison between the temperatures of the experimental and simulated tungsten film with a thickness of 260 nm as a function of the input power. In Figure 4-14a the experimental results are plotted against the electrical input power, and the simulation results are consistently higher than the experimental design. This deviation is attributed to unavoidable heat losses in the experimental setup, including conduction through the wiring and stainless-steel holder and power losses through surface radiation, as well as convection due to the limited vacuum conditions.

Using the actual input power estimated from Equation *4.2*, the input was calculated based exclusively on the radiative heat emitted from the AlN and tungsten surfaces, as determined by their temperatures and respective emissivity. The results, shown in Figure 4-14b, collapse much more closely onto the simulated trend showing that the model successfully captures the fundamental thermal behavior of

the emitter. However, a residual offset remains between the experiment and the simulation which can be explained by uncertainty in the tungsten film thickness assumed in the COMSOL model. Since the electrical resistance inversely proportional to film thickness, a slight deviation in thickness can shift the simulated input power for a given voltage. For example, a 10% deviation in thickness causes 10% error in the simulated power and a corresponding 20 to 30 K difference in emitter temperature near 1000 K.

4.3.2 TPV System Performance Comparison

This section presents how the experimental results of the TPV system align with theoretical predictions. Figure 4-15 presents the analytical prediction obtained using the same numerical modelling method, with the difference that the inputs were set according to the real experimental conditions. The vertical axis corresponds to the input power from Joule heating ($P_{in(1)}$), while the horizontal axis represents the input power from the halogen lamp source ($P_{in(2)}$). The color contours illustrate the single-source, multi-source, and enhancement cases as described earlier.

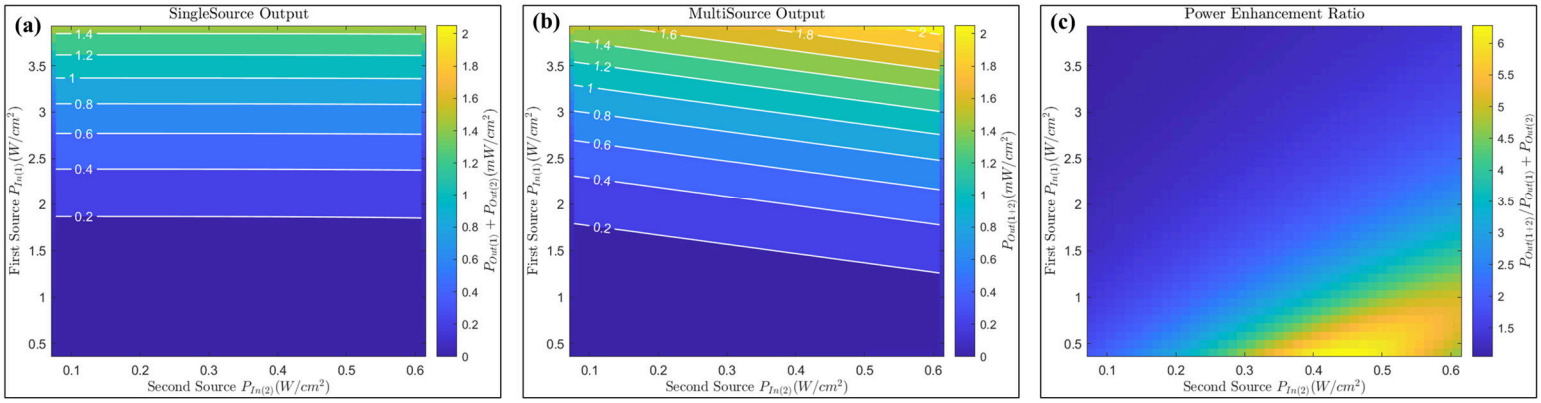


Figure 4-15 The output result from analytical modelling by utilizing experimental inputs

When comparing the analytical model with the experimental results shown in Figure 4-12, it is clear that the main trends in both are nearly identical. The single-source, multi-source, and enhancement plots display the same overall patterns, confirming that the model captures the essential physical behavior of the system. As expected, the experimental outputs are somewhat lower in magnitude, which can be attributed to conductive and convective heat losses, uncertainties in emissivity, and electrical losses in the TPV cell assembly. For example, the maximum output power in single and multi-source operation from the analytical model was 1.44 and 2.05 mW/cm², slightly higher than the corresponding experimental values of 1.08 and 1.72 mW/cm².

At very low outputs, the enhancement ratios in the experimental data appear much higher (up to 55.7 X), whereas the analytical prediction only rises to 6.28X. This difference occurs because, at very low

radiation levels and input powers, the TPV output is extremely small, and the measurement devices cannot capture it with high precision. As a result, dividing by a very small denominator leads to an artificially high ratio. At more practical operating temperatures, however, the enhancement predicted by the model reaches 142%, compared with 158% experimentally. Overall, the experimental enhancement lies between 1.2X and 2.0X, which is in good agreement with the analytical prediction.

5 Chapter 5: Conclusion & Future Work

5.1 Conclusion

The growing demand for efficient energy conversion and the recovery of wasted heat emphasizes the importance of technologies that can directly generate electricity from thermal sources. TPV systems are a strong candidate in this regard, as they can convert heat into power efficiently and reliably, without the need for moving parts. They are also flexible in scale, working for both small and large applications, and can run on different kinds of thermal sources. To push this idea further, this work looks at TPV systems that use more than one heat source. In this study, the potential of a TPV setup powered by dual heat sources is examined through three main objectives described below:

- Objective 1: Prove the concept of a multi-source TPV system analytically by applying established performance equations, including formulas for spectral in-band emissive power and electrical power output.

First, the in-band emissive power of three different TPV cells, namely Si, GaSb, and InGaAs with different bandgaps, was examined. In this analysis, Stefan–Boltzmann and Planck's law were applied to calculate the in-band emissive power. The next step was to investigate the TPV cell output and develop a model to simulate the generated electricity in a manner consistent with the experimental setup. By studying the relationship between emitter temperature (ranging from 500 to 1270 K) and the resulting current density and voltage, the values of V_{mp} and J_{mp} were determined, leading to the calculation of P_{mp}. In both cases, the advantage of multisource powering over separate powering was demonstrated, thereby fulfilling Objective 1. Coding was also used to compare analytical and experimental output results.

- Objective 2: Fabricate an absorber-emitter capable of reaching high temperatures under vacuum conditions.

An AlN ceramic sheet was selected and coated with a 1 μm tungsten layer using the DC sputtering method. An emitter holder was then constructed to electrically power the emitter and heat it through Joule

heating. Thermal performance tests of the absorber–emitter showed that by varying the voltage from 1 to 10 V, temperatures up to 1100 K could be achieved. Thus, Objective 2 was successfully accomplished, and the absorber–emitter was prepared for integration into the multi-source TPV system.

- Objective 3: Utilize the absorber-emitter developed in Objective 2 to construct a vacuum-based multi-source TPV system and experimentally validate the theoretical findings.

A multi-source TPV system was designed and successfully tested inside a vacuum chamber. The setup combined a halogen lamp as the radiative heat source, a GaSb TPV circuit, an active water-cooling system, and the custom absorber–emitter from Objective 2, which played a key role in the process. At peak operating conditions, the system generated 1.08 mW/cm² in single-source mode and 1.72 mW/cm² in dual-source mode, showing a 159% gain when both sources were used together. The experimental results followed the same trend predicted in Objective 1 through analytical modeling and coding, which confirmed the reliability of the theoretical approach.

5.2 Future Work

Although the multi-source TPV system was successfully demonstrated, and its advantages were shown through the results, several aspects of the design and assembly still require further investigation and improvement. These directions for future work are outlined below:

1) Analytical modelling

For future work, simulation modeling should be carried out to better understand and minimize heat losses in the setup. Such modeling could be used to optimize the emitter holder design and to simulate the effect of adding secondary sources on the emitter temperature, ultimately guiding improvements to the experimental setup.

A limitation of the analytical study is the lack of spectral emissivity data at different temperatures, which limits accurate prediction of TPV performance. Future work should include measuring or accessing this data to better assess system efficiency under real conditions.

2) Experimental setup and sub-assemblies

As discussed earlier, one of the main issues contributing to discrepancies in the results was the vacuum level at which the experiments were carried out. Significant heat was lost due to convective heat transfer, mainly because the vacuum pump could only reduce the system pressure to 10 mTorr. In addition, the presence of residual oxygen at this pressure may have led to partial oxidation of the emitter surface, further influencing its thermal behavior, potentially raising its temperature and improving overall performance.

The radiative heat source previously used, a halogen lamp, provided limited input power and was not sufficient to raise the emitter to the optimal operating temperature for the TPV cell. More powerful heat sources, such as laser power beaming, can be implemented to overcome this limitation.

Additionally, the emitter holder design played a critical role in performance. The tight attachment of the emitter to stainless steel improved the electrical connection but also caused generated heat and

incoming power to disperse across the stainless-steel sheet, resulting in substantial radiative heat loss. Future designs should focus on improving the holder to secure the emitter effectively while minimizing heat loss.

Furthermore, in this study, a plain tungsten deposition pattern was chosen for simplicity. Exploring different deposition geometries could lead to improved power transfer and efficiency. Other ceramic substrates, such as boron nitride (BN), may also be tested to evaluate the thermal and radiative performance of alternative materials.

Finally, enhancing the TPV circuit assembly to reduce electrical losses represents another promising area of improvement. In addition, modifying the assembly to increase its thermal contact with the cooling plate could improve heat conduction and further stabilize system performance.

3) Comparison and real-life applications

A practical next step is to compare the performance of the proposed system with other existing TPV systems, particularly in terms of overall efficiency. As discussed in earlier sections, raising the emitter temperature increases efficiency because it shifts the emitted spectrum closer to the TPV cell's bandgap, resulting in higher photon flux and more effective energy conversion. Such a comparison would highlight the advantages of the multi-source configuration more clearly and establish benchmarks for improvement.

Another important step is the development of a portable prototype. A compact, portable version of the multi-source TPV system would not only demonstrate its practical feasibility but also showcase its potential in real-world applications such as remote power generation, backup energy supply, and integration into hybrid renewable energy systems. This step would bridge the gap between laboratory-scale validation and broader practical implementation.

In addition, conducting a cost analysis of the proposed design would provide valuable insight into its economic feasibility and help identify trade-offs between performance, complexity, and scalability. This step would bridge the gap between laboratory-scale validation and broader practical implementation.

6 References

[1] K. V. Selvan and M. S. Mohamed Ali, “Micro-scale energy harvesting devices: Review of methodological performances in the last decade,” *Renewable and Sustainable Energy Reviews*, vol. 54, pp. 1035–1047, Feb. 2016, doi: 10.1016/J.RSER.2015.10.046.

[2] D. L. . Chubb, “Fundamentals of thermophotovoltaic energy conversion,” *Elsevier*, p. 515, 2007.

[3] T. J. Coutts, “A review of progress in thermophotovoltaic generation of electricity,” *Renewable and Sustainable Energy Reviews*, vol. 3, no. 2–3, pp. 77–184, Jun. 1999, doi: 10.1016/S1364-0321(98)00021-5.

[4] H. Daneshvar, R. Prinja, and N. P. Kherani, “Thermophotovoltaics: Fundamentals, challenges and prospects,” *Appl Energy*, vol. 159, pp. 560–575, Dec. 2015, doi: 10.1016/J.APENERGY.2015.08.064.

[5] R. Sakakibara *et al.*, “Practical emitters for thermophotovoltaics: a review,” *J Photonics Energy*, vol. 9, no. 3, p. 032713, Feb. 2019, doi: 10.1117/1.JPE.9.032713.

[6] O. V. Sulima and A. W. Bett, “Fabrication and simulation of GaSb thermophotovoltaic cells,” *Solar Energy Materials and Solar Cells*, vol. 66, no. 1–4, pp. 533–540, Feb. 2001, doi: 10.1016/S0927-0248(00)00235-X.

[7] S. Wojtczuk, E. Gagnon, L. Geoffroy, and T. Parodos, “InxGa1−xAs thermophotovoltaic cell performance vs bandgap,” *AIP Conf Proc*, vol. 321, no. 1, pp. 177–187, Jan. 1995, doi: 10.1063/1.47020.

[8] A. Datas, P. Bondavalli, and A. M. Pantaleo, “Embracing thermophotovoltaic electricity: Pathways to market adoption,” *Solar Energy Materials and Solar Cells*, vol. 283, p. 113419, May 2025, doi: 10.1016/J.SOLMAT.2025.113419.

[9] M. Giteau, M. F. Picardi, and G. T. Papadakis, “Thermodynamic figure of merit for thermophotovoltaics,” *https://doi.org/10.1117/1.JPE.14.042402*, vol. 14, no. 4, p. 042402, Feb. 2024, doi: 10.1117/1.JPE.14.042402.

[10] J. Islas, “The Gas Turbine: A New Technological Paradigm in Electricity Generation,” *Technol Forecast Soc Change*, vol. 60, no. 2, pp. 129–148, Feb. 1999, doi: 10.1016/S0040-1625(98)00036-5.

[11] A. Datas and A. Martí, “Thermophotovoltaic energy in space applications: Review and future potential,” *Solar Energy Materials and Solar Cells*, vol. 161, pp. 285–296, Mar. 2017, doi: 10.1016/J.SOLMAT.2016.12.007.

[12] C. Amy, H. R. Seyf, M. A. Steiner, D. J. Friedman, and A. Henry, “Thermal energy grid storage using multi-junction photovoltaics,” *Energy Environ Sci*, vol. 12, no. 1, pp. 334–343, Jan. 2019, doi: 10.1039/C8EE02341G.

[13] Y. Wang, H. Liu, and J. Zhu, “Solar thermophotovoltaics: Progress, challenges, and opportunities,” *APL Mater*, vol. 7, no. 8, Aug. 2019, doi: 10.1063/1.5114829.

[14] K. F. Mustafa, S. Abdullah, M. Z. Abdullah, and K. Sopian, “A review of combustion-driven thermoelectric (TE) and thermophotovoltaic (TPV) power systems,” *Renewable and Sustainable Energy Reviews*, vol. 71, pp. 572–584, May 2017, doi: 10.1016/J.RSER.2016.12.085.

[15] A. Licht, N. Pfiester, D. Demeo, J. Chivers, and T. E. Vandervelde, “A Review of Advances in Thermophotovoltaics for Power Generation and Waste Heat Harvesting,” *MRS Adv*, vol. 4, no. 41–42, pp. 2271–2282, Sep. 2019, doi: 10.1557/ADV.2019.342/METRICS.

[16] A. Datas, P. Bondavalli, and A. M. Pantaleo, “Embracing thermophotovoltaic electricity: Pathways to market adoption,” *Solar Energy Materials and Solar Cells*, vol. 283, p. 113419, May 2025, doi: 10.1016/J.SOLMAT.2025.113419.

[17] A. Datas, A. Ramos, A. Martí, C. del Cañizo, and A. Luque, "Ultra high temperature latent heat energy storage and thermophotovoltaic energy conversion," *Energy*, vol. 107, pp. 542–549, Jul. 2016, doi: 10.1016/J.ENERGY.2016.04.048.

[18] M. M. A. Gamel *et al.*, "A Review on Thermophotovoltaic Cell and Its Applications in Energy Conversion: Issues and Recommendations," *Materials*, vol. 14, no. 17, p. 4944, Sep. 2021, doi: 10.3390/MA14174944.

[19] L. Fraas, J. Avery, and L. Minkin, "Design of a portable fuel fired cylindrical TPV battery replacement," *9th Annual International Energy Conversion Engineering Conference, IECEC 2011*, Jan. 2011.

[20] C. Forman, I. K. Muritala, R. Pardemann, and B. Meyer, "Estimating the global waste heat potential," *Renewable and Sustainable Energy Reviews*, vol. 57, pp. 1568–1579, May 2016, doi: 10.1016/J.RSER.2015.12.192.

[21] A. Lenert *et al.*, "A nanophotonic solar thermophotovoltaic device," *Nature Nanotechnology 2014 9:2*, vol. 9, no. 2, pp. 126–130, Jan. 2014, doi: 10.1038/nnano.2013.286.

[22] E. López, I. Artacho, and A. Datas, "Thermophotovoltaic conversion efficiency measurement at high view factors," *Solar Energy Materials and Solar Cells*, vol. 250, p. 112069, Jan. 2023, doi: 10.1016/J.SOLMAT.2022.112069.

[23] Z. Wang *et al.*, "Selective emitter materials and designs for high-temperature thermophotovoltaic applications," *Solar Energy Materials and Solar Cells*, vol. 238, p. 111554, May 2022, doi: 10.1016/J.SOLMAT.2021.111554.

[24] E. Rephaeli and S. Fan, "Absorber and emitter for solar thermo-photovoltaic systems to achieve efficiency exceeding the Shockley-Queisser limit," *Optics Express, Vol. 17, Issue 17, pp. 15145-15159*, vol. 17, no. 17, pp. 15145–15159, Aug. 2009, doi: 10.1364/OE.17.015145.

[25] R. Sakakibara, “High-performance metallo-dielectric photonic crystals: Design, fabrication, and testing of a practical emitter for portable thermophotovoltaic generators,” 2021, Accessed: Aug. 05, 2025. [Online]. Available: https://dspace.mit.edu/handle/1721.1/139896

[26] W. R. Chan *et al.*, “Toward high-energy-density, high-efficiency, and moderate-temperature chip-scale thermophotovoltaics,” *Proc Natl Acad Sci U S A*, vol. 110, no. 14, pp. 5309–5314, Apr. 2013, doi: 10.1073/PNAS.1301004110/ASSET/43323F29-7D87-478C-8CDD-C8AE65DE2E76/ASSETS/GRAPHIC/PNAS.1301004110FIG05.JPEG.

[27] U. C. Pernisz and C. K. Saha, “Silicon carbide emitter and burner elements for a TPV converter,” *AIP Conf Proc*, vol. 321, no. 1, pp. 99–105, Jan. 1995, doi: 10.1063/1.47060.

[28] A. A. K. Azri *et al.*, “Research on micro-thermophotovoltaic power generators with different emitting materials,” *Journal of Micromechanics and Microengineering*, vol. 15, no. 9, p. S239, Aug. 2005, doi: 10.1088/0960-1317/15/9/S11.

[29] M. Shimizu, A. Kohiyama, and H. Yugami, “High-efficiency solar-thermophotovoltaic system equipped with a monolithic planar selective absorber/emitter,” *https://doi.org/10.1117/1.JPE.5.053099*, vol. 5, no. 1, p. 053099, Jan. 2015, doi: 10.1117/1.JPE.5.053099.

[30] L. Fraas, J. Samaras, J. Avery, and L. Minkin, “Antireflection coated refractory metal matched emitters for use with GaSb thermophotovoltaic generators,” *Conference Record of the IEEE Photovoltaic Specialists Conference*, vol. 2000-January, pp. 1020–1023, 2000, doi: 10.1109/PVSC.2000.916059.

[31] H. Yugami, H. Sai, K. Nakamura, N. Nakagawa, and H. Ohtsubo, “Solar thermophotovoltaic using Al2O3/Er3Al5O12 eutectic composite selective emitter,” *Conference Record of the IEEE Photovoltaic Specialists Conference*, vol. 2000-January, pp. 1214–1217, 2000, doi: 10.1109/PVSC.2000.916107.

[32] R. A. Lowe, D. L. Chubb, and B. S. Good, “Radiative performance of rare earth garnet thin film selective emitters,” *AIP Conf Proc*, vol. 321, no. 1, pp. 291–297, Jan. 1995, doi: 10.1063/1.47031.

[33] B. Bitnar, W. Durisch, J. C. Mayor, H. Sigg, and H. R. Tschudi, “Characterisation of rare earth selective emitters for thermophotovoltaic applications,” *Solar Energy Materials and Solar Cells*, vol. 73, no. 3, pp. 221–234, Jul. 2002, doi: 10.1016/S0927-0248(01)00127-1.

[34] R. A. Lowe, D. L. Chubb, S. C. Farmer, and B. S. Good, “Rare-earth garnet selective emitter,” *Appl Phys Lett*, vol. 64, no. 26, pp. 3551–3553, 1994, doi: 10.1063/1.111221.

[35] W. R. Chan *et al.*, “Toward high-energy-density, high-efficiency, and moderate-temperature chip-scale thermophotovoltaics,” *Proc Natl Acad Sci U S A*, vol. 110, no. 14, pp. 5309–5314, Apr. 2013, doi: 10.1073/PNAS.1301004110/ASSET/43323F29-7D87-478C-8CDD-C8AE65DE2E76/ASSETS/GRAPHIC/PNAS.1301004110FIG05.JPEG.

[36] A. Lenert *et al.*, “A nanophotonic solar thermophotovoltaic device,” *Nature Nanotechnology 2014 9:2*, vol. 9, no. 2, pp. 126–130, Jan. 2014, doi: 10.1038/nnano.2013.286.

[37] M. Chirumamilla *et al.*, “Metamaterial emitter for thermophotovoltaics stable up to 1400 °C,” *Sci Rep*, vol. 9, no. 1, pp. 1–11, Dec. 2019, doi: 10.1038/S41598-019-43640-6;TECHMETA=128,132,140;SUBJMETA=1015,301,357,399,624,639;KWRD=METAMATERIALS.

[38] M. Araghchini *et al.*, “Fabrication of two-dimensional tungsten photonic crystals for high-temperature applications,” *Journal of Vacuum Science & Technology B, Nanotechnology and Microelectronics: Materials, Processing, Measurement, and Phenomena*, vol. 29, no. 6, p. 61402, Nov. 2011, doi: 10.1116/1.3646475/104344.

[39] Y. X. Yeng *et al.*, “Enabling high-temperature nanophotonics for energy applications,” *Proc Natl Acad Sci U S A*, vol. 109, no. 7, pp. 2280–2285, Feb. 2012, doi:

10.1073/PNAS.1120149109/ASSET/A272A712-450D-426D-B7D4-3183CE65989D/ASSETS/GRAPHIC/PNAS.1120149109FIG5.JPEG.

[40] M. Soljačić *et al.*, "High-temperature stability and selective thermal emission of polycrystalline tantalum photonic crystals," *Optics Express, Vol. 21, Issue 9, pp. 11482-11491*, vol. 21, no. 9, pp. 11482–11491, May 2013, doi: 10.1364/OE.21.011482.

[41] K. A. Arpin *et al.*, "Three-dimensional self-assembled photonic crystals with high temperature stability for thermal emission modification," *Nat Commun*, vol. 4, no. 1, pp. 1–8, Oct. 2013, doi: 10.1038/NCOMMS3630;TECHMETA=121,128,135,140,145;SUBJMETA=1032,301,399,624,639,930;KWRD=DESIGN.

[42] M. Garín, D. Hernández, T. Trifonov, and R. Alcubilla, "Three-dimensional metallo-dielectric selective thermal emitters with high-temperature stability for thermophotovoltaic applications," *Solar Energy Materials and Solar Cells*, vol. 134, pp. 22–28, Mar. 2015, doi: 10.1016/J.SOLMAT.2014.11.017.

[43] A. S. Vlasov, V. P. Khvostikov, O. A. Khvostikova, P. Y. Gazaryan, S. V. Sorokina, and V. M. Andreev, "TPV Systems with Solar Powered Tungsten Emitters," *AIP Conf Proc*, vol. 890, no. 1, pp. 327–334, Feb. 2007, doi: 10.1063/1.2711750.

[44] A. Heinzel, V. Boerner, A. Gombert, B. Bläsi, V. Wittwer, and J. Luther, "Radiation filters and emitters for the NIR based on periodically structured metal surfaces," *J Mod Opt*, vol. 47, no. 13, pp. 2399–2419, 2000, doi: 10.1080/09500340008230522.

[45] S. Y. Lin, J. Moreno, and J. G. Fleming, "Three-dimensional photonic-crystal emitter for thermal photovoltaic power generation," *Appl Phys Lett*, vol. 83, no. 2, pp. 380–382, Jul. 2003, doi: 10.1063/1.1592614.

[46] H. Sai, Y. Kanamori, and H. Yugami, “Tuning of the thermal radiation spectrum in the near-infrared region by metallic surface microstructures,” *Journal of Micromechanics and Microengineering*, vol. 15, no. 9, p. S243, Aug. 2005, doi: 10.1088/0960-1317/15/9/S12.

[47] V. M. Andreev *et al.*, “Solar thermophotovoltaic system with high temperature tungsten emitter,” *Conference Record of the IEEE Photovoltaic Specialists Conference*, pp. 671–674, 2005, doi: 10.1109/PVSC.2005.1488220.

[48] Y. B. Chen and Z. M. Zhang, “Design of tungsten complex gratings for thermophotovoltaic radiators,” *Opt Commun*, vol. 269, no. 2, pp. 411–417, Jan. 2007, doi: 10.1016/J.OPTCOM.2006.08.040.

[49] C. Ungaro, S. K. Gray, and M. C. Gupta, “Solar thermophotovoltaic system using nanostructures,” *Optics Express, Vol. 23, Issue 19, pp. A1149-A1156*, vol. 23, no. 19, pp. A1149–A1156, Sep. 2015, doi: 10.1364/OE.23.0A1149.

[50] D. Kopper and M. S. Leite, “Material Screening for Thermophotovoltaic Optical Emitters,” *ACS Appl Energy Mater*, vol. 8, no. 7, pp. 4144–4151, Apr. 2025, doi: 10.1021/ACSAEM.4C02872/SUPPL_FILE/AE4C02872_SI_002.MP4.

[51] A. VanHorn and W. Zhou, “Design and optimization of a high temperature microheater for inkjet deposition,” *International Journal of Advanced Manufacturing Technology*, vol. 86, no. 9–12, pp. 3101–3111, Oct. 2016, doi: 10.1007/S00170-016-8440-8/METRICS.

[52] Z. E. Jeroish, K. S. Bhuvaneshwari, F. Samsuri, and V. Narayanamurthy, “Microheater: material, design, fabrication, temperature control, and applications—a role in COVID-19,” *Biomed Microdevices*, vol. 24, no. 1, pp. 1–49, Mar. 2022, doi: 10.1007/S10544-021-00595-8/FIGURES/14.

[53] J. Ramousse, O. Lottin, S. Didierjean, and D. Maillet, “Heat sources in proton exchange membrane (PEM) fuel cells,” *J Power Sources*, vol. 192, no. 2, pp. 435–441, Jul. 2009, doi: 10.1016/J.JPOWSOUR.2009.03.038.

[54] Y.-M. Juan *et al.*, “Local and CMOS-compatible synthesis of CuO nanowires on a suspended microheater on asilicon substrate,” *Nanotechnology*, vol. 21, no. 23, p. 235602, May 2010, doi: 10.1088/0957-4484/21/23/235602.

[55] R. M. Tiggelaar, “Silicon-technology based microreactors for high-temperature heterogeneous partial oxidation reactions,” Dec. 02, 2004. Accessed: Aug. 05, 2025. [Online]. Available: https://research.utwente.nl/en/publications/silicon-technology-based-microreactors-for-high-temperature-heter

[56] N. Verbrugghe, D. Fasquelle, B. Duponchel, and S. Députier, “Study of tungsten films deposited by DC sputtering dedicated to integrated heaters,” *Journal of Vacuum Science & Technology B, Nanotechnology and Microelectronics: Materials, Processing, Measurement, and Phenomena*, vol. 35, no. 3, p. 31204, May 2017, doi: 10.1116/1.4981786/593240.

[57] M. Xu, G. Slovin, J. Paramesh, T. E. Schlesinger, and J. A. Bain, “Thermometry of a high temperature high speed micro heater,” *Review of Scientific Instruments*, vol. 87, no. 2, p. 24904, Feb. 2016, doi: 10.1063/1.4942249/1021716.

[58] “Chapter 2 Surface Coating Methods,” *Tribology Series*, vol. 28, no. C, pp. 7–32, Jan. 1994, doi: 10.1016/S0167-8922(08)70752-1.

[59] F. J. G. Silva, “Nanoindentation on Tribological Coatings,” *Applied Nanoindentation in Advanced Materials*, pp. 111–133, Jan. 2017, doi: 10.1002/9781119084501.CH5.

[60] D. M. Mattox, “Handbook of Physical Vapor Deposition (PVD) Processing,” *Handbook of Physical Vapor Deposition (PVD) Processing*, Dec. 2007, doi: 10.1016/c2009-0-18800-1.

[61] H. Hoche, S. Groß, and M. Oechsner, “Development of new PVD coatings for magnesium alloys with improved corrosion properties,” *Surf Coat Technol*, vol. 259, no. PA, pp. 102–108, Nov. 2014, doi: 10.1016/J.SURFCOAT.2014.04.038.

[62] F. Silva, R. Martinho, M. Andrade, A. Baptista, and R. Alexandre, “Improving the Wear Resistance of Moulds for the Injection of Glass Fibre–Reinforced Plastics Using PVD Coatings: A Comparative Study,” *Coatings 2017, Vol. 7, Page 28*, vol. 7, no. 2, p. 28, Feb. 2017, doi: 10.3390/COATINGS7020028.

[63] A. M. A. Mubarak, E. H. E. Hamzah, and M. R. M. T. M. R. M. Tofr, “REVIEW OF PHYSICAL VAPOUR DEPOSITION (PVD) TECHNIQUES FOR HARD COATING,” *Jurnal Mekanikal*, pp. 42–51, 2005, Accessed: Aug. 05, 2025. [Online]. Available: https://jurnalmekanikal.utm.my/index.php/jurnalmekanikal/article/view/191

[64] A. Baptista, F. Silva, J. Porteiro, J. Míguez, and G. Pinto, “Sputtering Physical Vapour Deposition (PVD) Coatings: A Critical Review on Process Improvement and Market Trend Demands,” *Coatings 2018, Vol. 8, Page 402*, vol. 8, no. 11, p. 402, Nov. 2018, doi: 10.3390/COATINGS8110402.

[65] D. M. Mattox, “The Foundations of Vacuum Coating Technology,” *The Foundations of Vacuum Coating Technology*, pp. 1–150, Dec. 2003, doi: 10.1007/978-3-662-10329-6/COVER.

[66] T. Karabacak, J. J. Senkevich, G.-C. Wang, T.-M. Lu, and A. Phys Lett, “Stress reduction in sputter deposited films using nanostructured compliant layers by high working-gas pressures,” *Journal of Vacuum Science & Technology A*, vol. 23, no. 4, pp. 986–990, Jul. 2005, doi: 10.1116/1.1861940.

[67] D. M. Mattox, “Handbook of Physical Vapor Deposition (PVD) Processing,” *Handbook of Physical Vapor Deposition (PVD) Processing*, 2010.

[68] C. Mitterer, “PVD and CVD Hard Coatings,” *Comprehensive Hard Materials*, vol. 2, pp. 449–467, Jan. 2014, doi: 10.1016/B978-0-08-096527-7.00035-0.

[69] R. D. Arnell and P. J. Kelly, “Recent advances in magnetron sputtering,” *Surf Coat Technol*, vol. 112, no. 1–3, pp. 170–176, Feb. 1999, doi: 10.1016/S0257-8972(98)00749-X.

[70] K. Holmberg and A. Matthews, *Coatings Tribology: Properties techniques and applications in surface engineering*, vol. 28. Elsevier, 1994. Accessed: Aug. 06, 2025. [Online]. Available: https://cris.vtt.fi/en/publications/coatings-tribology-properties-techniques-and-applications-in-surf

[71] B. Rother, G. Ebersbach, and H. M. Gabriel, "Substrate-rotation systems and productivity of industrial PVD processes," *Surf Coat Technol*, vol. 116–119, pp. 694–698, Sep. 1999, doi: 10.1016/S0257-8972(99)00120-6.

[72] A. Datas and R. Vaillon, "Thermophotovoltaic energy conversion," *Ultra-High Temperature Thermal Energy Storage, Transfer and Conversion*, pp. 285–308, Jan. 2021, doi: 10.1016/B978-0-12-819955-8.00011-9.

[73] A. LaPotin *et al.*, "Thermophotovoltaic efficiency of 40%," *Nature 2022 604:7905*, vol. 604, no. 7905, pp. 287–291, Apr. 2022, doi: 10.1038/s41586-022-04473-y.

[74] T. J. Coutts, "A review of progress in thermophotovoltaic generation of electricity," *Renewable and Sustainable Energy Reviews*, vol. 3, no. 2–3, pp. 77–184, Jun. 1999, doi: 10.1016/S1364-0321(98)00021-5.

[75] B. Merabet, A. Maleque, and S. Belhachi, "A brief history of thermophotovoltaic development," *Semicond Sci Technol*, vol. 18, no. 5, p. S141, Apr. 2003, doi: 10.1088/0268-1242/18/5/301.

[76] L. Fraas, J. Avery, E. Malfa, J. G. Wuenning, G. Kovacik, and C. Astle, "Thermophotovoltaics for Combined Heat and Power Using Low NOx Gas Fired Radiant Tube Burners," *AIP Conf Proc*, vol. 653, no. 1, pp. 61–70, Jan. 2003, doi: 10.1063/1.1539364.

[77] R. S. Carlson and L. M. Fraas, "Adapting TPV for Use in a Standard Home Heating Furnace," *AIP Conf. Proc.*, vol. 890, pp. 273–279, 2007, Accessed: Aug. 09, 2025. [Online]. Available: https://cds.cern.ch/record/1035881

[78] E. M. West and W. R. Connelly, "Integrated development and testing of multi-kilowatt TPV generator systems," *AIP Conf Proc*, vol. 460, no. 1, pp. 446–456, Mar. 1999, doi: 10.1063/1.57826.

[79] A. Fiorino, L. Zhu, D. Thompson, R. Mittapally, P. Reddy, and E. Meyhofer, “Nanogap near-field thermophotovoltaics,” *Nat Nanotechnol*, vol. 13, no. 9, pp. 806–811, Sep. 2018, doi: 10.1038/S41565-018-0172-5;TECHMETA=119,120,123,128,144;SUBJMETA=166,639,925;KWRD=ENGINEERING,NANOSCIENCE+AND+TECHNOLOGY.

[80] J. Tatum, “Resistance and Temperature,” *LibreTexts*, Dec. 2016, Accessed: Aug. 09, 2025. [Online]. Available: https://phys.libretexts.org/Bookshelves/Electricity_and_Magnetism/Electricity_and_Magnetism_(Tatum)/04%3A_Batteries_Resistors_and_Ohm’s_Law/4.03%3A_Resistance_and_Temperature

[81] W. Shockley, *Electrons and holes in semiconductors*, vol. 84. van Nostrand New York, 1950.

[82] “Semiconductor Materials | PVEducation.” Accessed: Aug. 09, 2025. [Online]. Available: https://www.pveducation.org/pvcdrom/pn-junctions/semiconductor-materials

[83] S. Elbialy, B. Yousif, and A. Samra, “Modeling of active plasmonic coupler and filter based on metal-dielectric-metal waveguide,” *Opt Quantum Electron*, vol. 49, no. 4, pp. 1–19, Apr. 2017, doi: 10.1007/S11082-017-0961-3/FIGURES/24.

[84] D. A. Neamen *et al.*, “Semiconductor Physics and Devices McGraw-Hill Higher-Education Library of Congress Cataloging-in-Publication Data,” 2003.

[85] “N-Type vs P-Type Solar Cells: Understanding the Key Differences.” Accessed: Aug. 10, 2025. [Online]. Available: https://www.solarnplus.com/n-type-vs-p-type-solar-cells-differences/

[86] B. Zhou *et al.*, “Method to determine the single curve IV characteristic parameter of solar cell,” *J Phys Conf Ser*, vol. 1144, no. 1, p. 012012, Dec. 2018, doi: 10.1088/1742-6596/1144/1/012012.

[87] T. T. Hang and R. Chen, “Thermophotovoltaics (TPV) System to Accommodate High Efficiency Selective Emitter,” United States -- California, 2022. [Online]. Available: https://ezproxy.library.yorku.ca/login?url=https://www.proquest.com/dissertations-

theses/thermophotovoltaics-tpv-system-accommodate-high/docview/2832893518/se-2?accountid=15182

[88] E. Doyle, K. Shukla, and C. Metcalfe, “Development and Demonstration of a 25 Watt Thermophotovoltaic Power Source for a Hybrid Power System,” 2001. Accessed: Jul. 31, 2025. [Online]. Available: http://www.sti.nasa.gov

[89] Y. Liu *et al.*, “Experimental performance comparison of 0.72 eV-GaSb and 0.59 eV-InGaAs thermophotovoltaic cells under different radiation temperatures,” *Appl Energy*, vol. 361, p. 122959, May 2024, doi: 10.1016/J.APENERGY.2024.122959.

[90] N. Talebzadeh, S. Homaei, and P. G. O’Brien, “Optimizing thermophotovoltaic (TPV) systems through photon fate analysis: An experimental case study based on ellipsoidal optical cavities,” *Solar Energy Materials and Solar Cells*, vol. 288, p. 113634, Aug. 2025, doi: 10.1016/J.SOLMAT.2025.113634.

[91] A. Datas and C. Algora, “Development and experimental evaluation of a complete solar thermophotovoltaic system,” *Progress in Photovoltaics: Research and Applications*, vol. 21, no. 5, pp. 1025–1039, Aug. 2013, doi: 10.1002/PIP.2201;PAGEGROUP:STRING:PUBLICATION.

[92] D. Li and Y. Xuan, “Design and evaluation of a hybrid solar thermphotovoltaic-thermoelectric system,” *Solar Energy*, vol. 231, pp. 1025–1036, Jan. 2022, doi: 10.1016/J.SOLENER.2021.12.049.

[93] C. M. I. Hussain, A. Duffy, and B. Norton, “Thermophotovoltaic systems for achieving high-solar-fraction hybrid solar-biomass power generation,” *Appl Energy*, vol. 259, p. 114181, Feb. 2020, doi: 10.1016/J.APENERGY.2019.114181.

[94] G. Davis, “Hybrid thermophotovoltaic power systems,” Technical report P500-02-048F, California Energy Commission, 2002.

[95] C. M. I. H. cmih, B. Norton, A. Duffy, and M. Oubaha, “Hybrid Solar Thermophotovoltaic-Biomass/Gas Power Generation System with a Spectrally Matched Emitter for Lower Operating Temperatures,” 2017.

[96] C. M. I. Hussain, A. Duffy, and B. Norton, “Economic appraisal of hybrid solar–biomass thermophotovoltaic power generation,” *Proceedings of the Institution of Civil Engineers - Energy*, vol. 172, no. 4, pp. 162–168, Sep. 2019, doi: 10.1680/JENER.19.00023.

[97] G. Guazzoni and M. McAlonan, “Multifuel (liquid hydrocarbons) TPV generator,” *AIP Conf Proc*, vol. 401, no. 1, pp. 341–354, Mar. 1997, doi: 10.1063/1.53274.

[98] E. M. Watson and W. E. Forsythe, “Resistance and Radiation of Tungsten as a Function of Temperature,” *JOSA, Vol. 24, Issue 4, pp. 114-118*, vol. 24, no. 4, pp. 114–118, Apr. 1934, doi: 10.1364/JOSA.24.000114.

[99] D. De Faoite, D. J. Browne, F. R. Chang-Díaz, and K. T. Stanton, “A review of the processing, composition, and temperature-dependent mechanical and thermal properties of dielectric technical ceramics,” *Journal of Materials Science 2011 47:10*, vol. 47, no. 10, pp. 4211–4235, Dec. 2011, doi: 10.1007/S10853-011-6140-1.

[100] J. Hameury *et al.*, “Identification and Characterization of New Materials for Construction of Heating Plates for High-Temperature Guarded Hot Plates,” *Int J Thermophys*, vol. 39, no. 1, Jan. 2018, doi: 10.1007/S10765-017-2326-3.

[101] I. L. Shabalin, “Tungsten,” *Ultra-High Temperature Materials I*, pp. 237–315, 2014, doi: 10.1007/978-94-007-7587-9_3.

[102] S. M. Sze and K. K. Ng, “Physics of Semiconductor Devices, Third Edition,” *Physics of Semiconductor Devices, Third Edition*, pp. 12–16, Jan. 2006, doi: 10.1002/0470068329.

[103] Y. Liu *et al.*, "Experimental performance comparison of 0.72 eV-GaSb and 0.59 eV-InGaAs thermophotovoltaic cells under different radiation temperatures," *Appl Energy*, vol. 361, p. 122959, May 2024, doi: 10.1016/J.APENERGY.2024.122959.

[104] A. L. Stanford and J. M. Tanner, "Early Quantum Physics," *Physics for Students of Science and Engineering*, pp. 691–716, Jan. 1985, doi: 10.1016/B978-0-12-663380-1.50026-4.

[105] A. Schock, M. Mukunda, C. Or, V. Kumar, and G. Summers, "Design, analysis, and optimization of a radioisotope thermophotovoltaic (RTPV) generator, and its applicability to an illustrative space mission," *Acta Astronaut*, vol. 37, no. C, pp. 21–57, Oct. 1995, doi: 10.1016/0094-5765(95)00071-7.

[106] H. R. Devi, O. Y. Bisen, S. Nanda, R. Nandan, and K. K. Nanda, "Internal versus external quantum efficiency of luminescent materials, photovoltaic cells, photodetectors and photoelectrocatalysis," *Curr Sci*, vol. 121, no. 7, p. 894, Oct. 2021, doi: 10.18520/CS/V121/I7/894-898.

[107] *Instruction manual No. 699904400*, Revision 2. Varian vacuum products, 1997.

[108] "Kurt J. Lesker Company | KJLC® 375 Series Panel Mount / Benchtop Gauge Controller | Enabling Technology for a Better World." Accessed: Jul. 04, 2025. [Online]. Available: https://www.lesker.com/newweb/gauges/convection_kjlc_5.cfm

[109] "VEVOR Laboratory Chiller Circulator 6L Lab Recirculating Chiller 23°F-212°F | VEVOR CA." Accessed: Jul. 04, 2025. [Online]. Available: https://www.vevor.ca/laboratory-recirculating-chiller-c_11045/vevor-laboratory-chiller-circulator-6l-lab-recirculating-chiller-23-f-212-f-p_010515419251?srsltid=AfmBOoqbBQu4VSt58149_0aiEMGSlVKjmB5_cFZwS8i8UcFPeUvDzK6V

[110] "Ethanol Freeze Protected Water Solutions." Accessed: Jul. 04, 2025. [Online]. Available: https://www.engineeringtoolbox.com/ethanol-water-d_989.html

[111] “Fractal Paste - (8 Fluid Ounces).” Accessed: Jul. 05, 2025. [Online]. Available: https://mhi-inc.com/product/fractal-paste-8-fluid-ounces/

[112] “Kurt J. Lesker Company | Tungsten W Sputtering Targets | Enabling Technology for a Better World.” Accessed: Jul. 04, 2025. [Online]. Available: https://www.lesker.com/newweb/deposition_materials/depositionmaterials_sputtertargets_1.cfm?pgid=w1

[113] “AMOD Physical Vapour Deposition Platform » APP Systems Services.” Accessed: Jul. 30, 2025. [Online]. Available: https://appsystems.com.sg/product/amod-physical-vapour-deposition-platform/

[114] “304 Stainless Steel.” Accessed: Jul. 04, 2025. [Online]. Available: https://www.matweb.com/search/datasheet.aspx?MatGUID=abc4415b0f8b490387e3c922237098da&ckck=1

[115] “EXTREME ODYSSEY 120x20x0.5mm – Thermalright.” Accessed: Jul. 04, 2025. [Online]. Available: https://thermalright.com/product/odyssey-thermal-pad-120x20x0-5mm/

[116] “1600nm 25mm Diameter , OD 2.0 Shortpass Filter | Edmund Optics.” Accessed: Jul. 04, 2025. [Online]. Available: https://www.edmundoptics.ca/p/1600nm-25mm-diameterod-2-shortpass-filter/27725/

[117] “ATS-TCP-1001.” Accessed: Jul. 04, 2025. [Online]. Available: https://www.qats.com/Products/Liquid-Cooling/Tubed-Cold-Plates/ATS-TCP-1001